The Influence of Pressure Ratio on Film Cooling Performance of a Turbine Blade

By
James V. Bubb

Thesis Submitted to
Virginia Polytechnic Institute and State University
in partial fulfillment of the requirements for the degree of

Master of Science

in

Mechanical Engineering

Thomas E. Diller, Chairman
Wing Ng
Joseph A. Schetz

August, 1999
Blacksburg, Virginia

The Influence of Pressure Ratio on Film Cooling Performance of a Turbine Blade

James V. Bubb
Virginia Polytechnic Institute and State University, 1999
Advisor: Dr. Thomas E. Diller, Dr. Wing F. Ng

ABSTRACT

The relationship between the plenum to freestream total pressure ratio on film cooling performance is experimentally investigated. Measurements of both the heat transfer coefficient and the adiabatic effectiveness were made on the suction side of the center blade in a linear transonic cascade. Entrance and exit Mach numbers were 0.3 and 1.2 respectively. Reynolds number based on chord and exit conditions is 3×10^6. The blade contour is representative of a typical General Electric first stage, high turning, turbine blade. Tunnel freestream conditions were 10 psig total pressure and approximately 80 ° C. A chilled air coolant film was supplied to a generic General Electric leading edge showerhead coolant scheme. Pressure ratios were varied from run to run over the ranges of 1.02 to 1.20. The density ratio was near a value of 2. A method to determine both the heat transfer coefficient and film cooling effectiveness from experimental data is outlined.

Results show that the heat transfer coefficient is independent of the pressure ratio over these ranges of blowing parameters. Also, there is shown to be a weak reduction of film cooling effectiveness with higher pressure ratios. Results are shown for effectiveness and heat transfer coefficient profiles along the blade.

Contents

Nomenclature

Symbols

A	Orifice area
C_d	Discharge coefficient
C_p	Specific heat
DR	Density ratio
h	Heat transfer coefficient
I	Momentum ratio
k	Thermal conductivity
$\dot{m}$	Mass flow rate
M	Blowing ratio
Ma	Mach Number
PR	Pressure ratio
q''	Heat flux
r	Recovery factor
S	Coolant hole spacing

T	Temperature
U	Velocity
Tu	Turbulence
x	Downstream distance

Greek Symbols

δ	Uncertainty
γ	Specific heat ratio
η	Adiabatic film cooling effectiveness
ρ	Density
ε	Error value (from Sec. 2.3.2.3)

Subscripts

act	Actual
aw	Adiabatic wall
c	Coolant
d	Drop from freestream
e	Boundary layer edge
∞	Freestream
obj	Objective
r	Recovery
t	Total
w	Wall

Chapter 1

Introduction

1.1 Background

1.1.1 Turbine Blade Heat Transfer

The gas turbine industry continues to push aircraft engine performance to higher levels. New engine designs are yielding higher efficiencies and thrust-to-weight ratios for modern aircraft. Fig. 1.1 is an illustration of a typical aircraft gas turbine. Critical to the increased performance is the increase of turbine inlet temperatures. It is well known that higher turbine inlet temperatures yield higher thermodynamic efficiencies, and present engine designs utilize turbine inlet temperatures well in excess of the operating conditions temperatures of blade materials. A historical perspective of progress of turbine inlet temperature is given in Fig. 1.2. This figure shows the widening difference between the blade temperatures and the turbine inlet temperature. This difference between the turbine inlet temperature and the blade operating temperature is realized through the use of blade cooling. There are many different

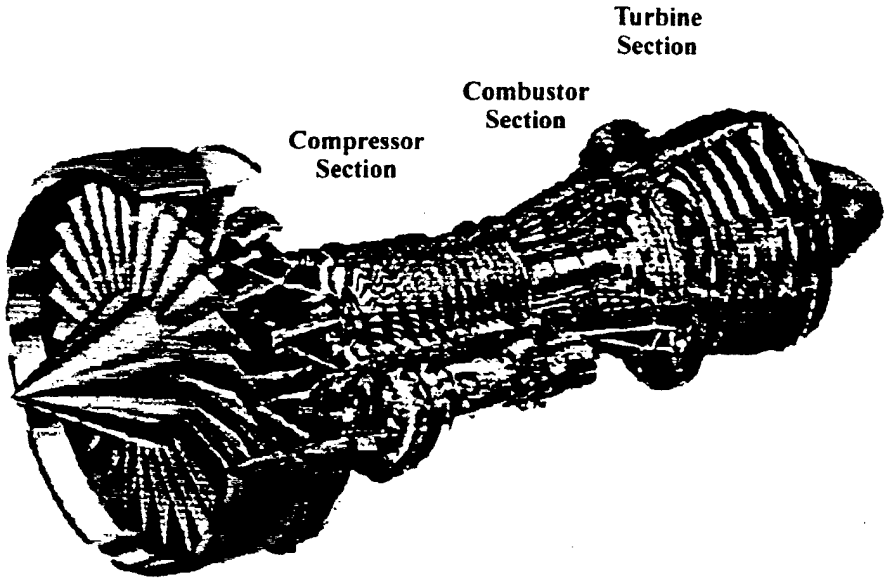

Figure 1.1: Modern Aircraft Engine (Courtesy *General Electric*)

cooling techniques that have been devised and implemented to keep the blade surfaces at lower temperatures. The future trend in engine design is to both increase turbine inlet temperatures further and to increase the temperature difference between the blade and the freestream flow. In order to push the envelope of engine performance further, a better understanding of coolant schemes is essential.

1.1.2 Film Cooling

One widely used blade cooling technique is film cooling. Film cooling is accomplished by injecting, from within the blade, a thin film of cold air along the blade surface separating the blade from the hot freestream gases. This film provides an insulating layer and has the effect of protecting the blade from high temperatures of the hot freestream flow. Fig. 1.3 illustrates three different film cooling schemes.

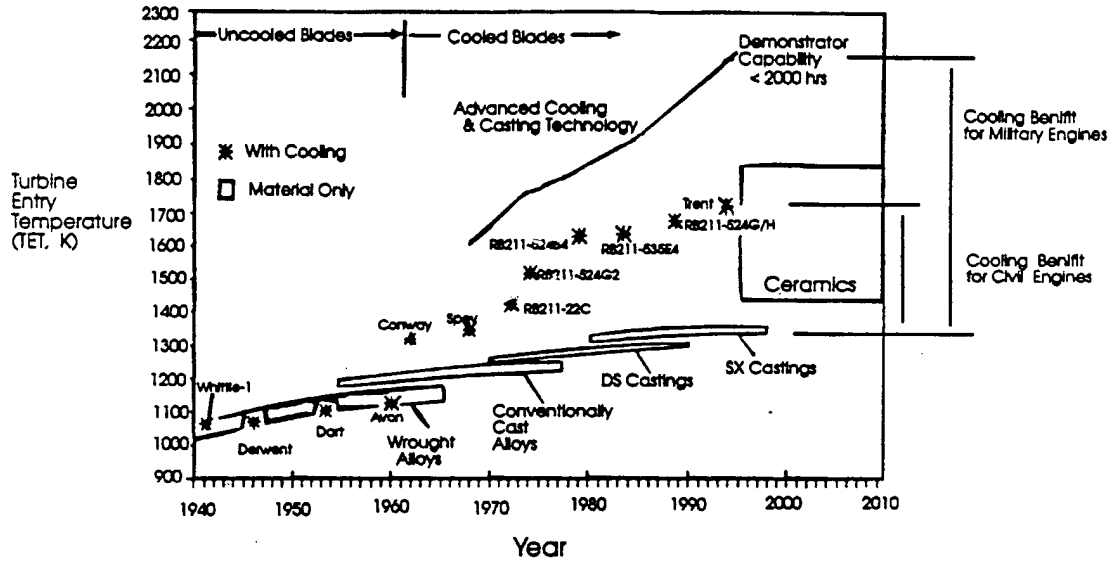

Figure 1.2: Advance of Materails and Cooling Technology, (Courtesy Royal Aeronautical Society/ Aerospace - 1994)

Unfortunately, this cold film protection from heat flux comes at a price. The source of the cold coolant air is bleed-off air from the last stage of the compressor section. This high pressure air bypasses the combustor section of the engine, and in so doing, is maintained at much lower temperatures than the core turbine flow. This bleed-off air, however, is removed from the core mass flow and subtracts from the overall thrust of the engine. Obviously, the engine designer wants to minimize the amount of bleed-off air required to cool the blade. From this, it is apparent that a good understanding of not only how film cooling schemes affect heat transfer is needed, but also an understanding of what parameters control the level of effectiveness provided is needed.

In the past, a great deal of research has been devoted to turbine heat transfer phenomenon, and specifically, film cooling schemes. A good summary of different film cooling research is given by Goldstein [7]. This study continues the understanding of film cooling heat transfer.

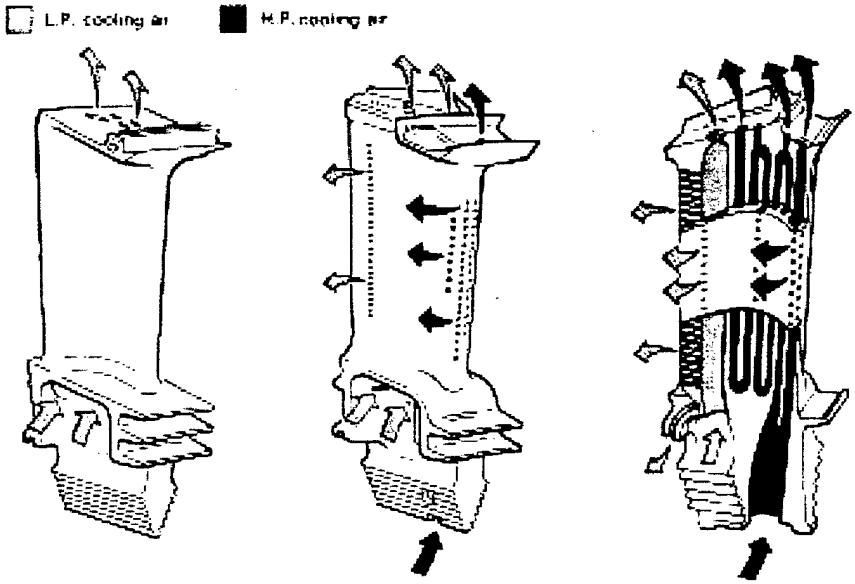

Figure 1.3: Film Cooling Schemes (Courtesy *Rolls-Royce*)

1.2 Motivation

1.2.1 Heat Transfer Coefficient

Turbine heat transfer and film cooling can be described using some important variables. In general, convective heat transfer is described by,

$$q'' = h \cdot (T_{aw} - T_w) \tag{1.1}$$

The first of the important variables in this equation is the heat transfer coefficient, h. The heat transfer coefficient is for the most part dictated by the external flow field. h is a factor that relates a driving temperature difference, $T_{aw} - T_w$, to absorbed heat flux energy, q''. In order to keep blade temperatures low, it is in the best interest of the turbine designer to attempt to minimize heat transfer and consequently, h. In general, the injection of film cooling changes the fluid flow profile around the blade and usually increases the heat transfer coefficient. This increase in h is undesirable as it promotes heat transfer from the hot freestream flow, and good designs of film cooling should attempt to minimize this increase. Obviously, an understanding of exactly how film coolant schemes affect the heat transfer coefficient is important. While the introduction of film cooling has the effect of increasing h slightly, the technique's advantage is realized by a large decrease of the adiabatic wall temperature, T_{aw}.

1.2.2 Film Cooling Effectiveness

Eqn. 1.1 also shows that a second variable of importance that describes heat transfer in engines is the driving temperature difference, $T_{aw} - T_w$. In film cooling schemes, however, it is more convenient to examine a dimensionless form of this driving temperature difference. This dimensionless parameter is defined as the adiabatic

film cooling effectiveness, η.

$$\eta \equiv \frac{T_r - T_{aw}}{T_r - T_c} \tag{1.2}$$

The details of this expression will be discussed at length later in the thesis, but a basic understanding of this variable implies that a higher effectiveness results in the blade surface being protected from the high temperatures of the core flow.

1.2.3 Film Cooling Parameters

This research is an experimental investigation of parameters effecting both the film cooling effectiveness and heat transfer coefficient. In general, η and h are functions of many parameters in an engine environment. The most influential parameters can be grouped into two categories, Aerodynamics and Geometry. Specifically η and h are functions of,

Cooling Geometry...

- Downstream location, $\frac{x}{D}$
- Coolant scheme geometry (hole length, hole spacing, blowing angle, etc.)

Aerodynamics...

- Local Freestream Mach Number, Ma
- Freestream Turbulence, Tu
- Film Cooling Momentum Ratio, I,

$$I \equiv \frac{\rho_c U_c^2}{\rho_\infty U_\infty^2} \tag{1.3}$$

- Film Cooling Blowing Ratio, M,

$$M \equiv \frac{\rho_c U_c}{\rho_\infty U_\infty} \tag{1.4}$$

- Film Cooling Density Ratio, DR,

$$DR \equiv \frac{\rho_c}{\rho_\infty} \tag{1.5}$$

In these experiments the only geometric parameter studied is the downstream distance. This will be investigated by the use of several heat flux gauges staggered along the blade profile. The rest of the coolant geometry is all specified and will remain constant. The blade shape and coolant hole geometries are all fixed to one design.

Furthermore in these experiments, the local Mach number is fixed by the blade design (see Fig 2.8 and Fig. 2.6 for Mach number distributions) and the tunnel operating conditions. For this reason, it will not be varied and studied systematically. Freestream turbulence has been shown to have an influence on heat transfer and film-cooling effectiveness but was not studied in this thesis due to time constraints.

There are several experimental ratios that dictate the manner in which the coolant air leaves the coolant holes. These ratios have been given significant discussion in previous research. One of these, the density ratio, has been shown by Foster et al. [6] and Goldstein et al. [8] to be of secondary importance in determining film cooling effectiveness, at least in the ranges where the current experiments are performed. Furthermore, Goldstein [7] suggests that the parameter of importance in determining whether the coolant film layer lifts off the surface is the momentum ratio.

Since the density ratio has been assumed to be of secondary importance, and only two of the parameters defined in Eqn. 1.3 through Eqn. 1.5 can be varied independently, it was decided to investigate and discuss the results in terms of the

momentum ratio, and the blowing ratio can be backed out from the other two ratios. This decision to control the momentum ratio is also convenient, because the only ratio that can be controlled consistently in the experimental apparatus is the pressure ratio. Because of hardware constraints, the pressure ratio is held to a constant in the course of an experiment, but the temperature ratio varies transiently. From the isentropic flow relations, it can be shown that the temperature dependence cancels out of the formulation of the momentum ratio (See Section 3.3) such that the momentum ratio is purely a function of pressure ratio.

Implied in the outset of this research is Foster's and Goldstein's suggestion that effectiveness is independent of the density ratio (and consequently the temperature ratio). This hypothesis is to be tested with the experiments to see if the effectiveness is truly independent of the density ratio.

This research is an extension to past work done at Virginia Tech on heat transfer measurements. Earlier experiments performed by Smith [22] have developed the technique for measuring heat transfer coefficient and effectiveness in the cascade facility. The extension of the research here involves using this technique to study the influence of pressure ratio (and consequently momentum ratio) on film cooling performance.

1.3 Literature Review

The approaches that have been taken to investigate film cooling phenomenon can be separated into general two areas: experimental and computational. This literature review will concentrate on the experimental side as this is the area where the current research program focuses.

The database of literature on film cooling experiments is very extensive. This short literature review does not profess to be an exhaustive list and discussion of all that has been published in the research area. For the different kinds of research, representative facilities have been selected and discussed where invariably there are multiple researchers performing similar types of experiments with similar conclusions. A reference that provides a nice overview of fundamental film cooling analysis and experiments and the conclusions reached by researchers is given by Goldstein [7].

The most basic of film cooling experiments starts with the flat plate experiment. These types of tests are the simplest to set-up, and detailed measurements of film cooling parameters can be made easily. Experiments done at the University of Minnesota by Goldstein et al. [8] are some of the most basic flat plate discrete hole film cooling experiments. These experiments were performed on both a single coolant hole and one row of coolant holes with a flat plate geometry. Also, these experiments were performed at low speeds rather than at high speeds which are more representative of an engine environment. The thrust of their research was to vary the injection angles and blowing ratios to investigate film cooling effectiveness. These experiments generally showed that the cooling effectiveness was optimized for the hole inclined at 35° to the streamwise direction and that the centerline effectiveness decayed monotonically with distance from the coolant hole. Also, this study showed that at a blowing ratio of approximately 0.5 the centerline cooling effectiveness reached a maximum value. The researchers suggested the decline of effectiveness at higher blowing ratios

was due to the coolant film lifting off the surface and allowing the freestream air to penetrate to the surface.

Compound injection angle schemes (holes angled both in the streamwise and spanwise directions) have been studied at great length and in general have been shown to increase overall cooling effectiveness by better distributing the coolant layer of the surface. Recent studies by Ligrani et al. [16] investigate the possibilities and results of angled injection schemes.

The effect of surface curvature was investigated by Schwartz et al. [21]. Film cooling effectiveness was measured in this research by a mass transfer technique. This research showed that convex surfaces (similar to the suction side of turbine blades) had higher effectiveness values at higher momentum ratios than those of the flat plate experiments. The reason for this is that the pressure gradient held the jet to the surface longer and allowed for better coverage at higher blowing ratios.

Experiments performed by Ekkad et al. [5] investigated the effect of freestream turbulence on heat transfer and film effectivness on a cylindrical model. These experiments used a transient liquid crystal technique which gave high resolution measurements of local heat transfer and film cooling effectiveness. The results from this research showed a maximum effectiveness at a blowing ratio of about 0.4. One important conclusion from this work was that higher values of freestream turbulence reduced film effectiveness at lower blowing ratios, but this effect was diminished at the higher blowing ratios. Also, with the use of the liquid crystal, they were able to show that the location of the highest film effectiveness changes with the increase of blowing ratio. This geometry begins to exhibit the two dimensional and three dimensional nature of film cooling.

From these idealized fundamental geometries, the experiments on realistic blade geometries is developed. Some of the earliest research on realistic geometries

was performed by Ito et al. [13]. These experiments used turbine blades in a low speed ($Ma = 0.065$), cascade wind tunnel with a single row of coolant holes and made measurements using the mass transfer technique. One of the conclusions of this research was that the convex suction side surface provides a pressure gradient that helps to keep the coolant film attached to the blade surface at higher momentum ratios. At the highest of momentum ratios (M >1.5), the film would eventually lift off the surface and the effectiveness would decrease. This work also showed the three dimensional nature of the problem as it illustrated that the blowing ratio where the maximum effectiveness occurred depended on the downstream and spanwise distance from the coolant holes.

Recent research conducted by Bunker et al. [2] from General Electric Aircraft Engines studied a turbine blade and showerhead film cooling geometry representative of actual engine hardware and similar to the geometry used in this research. The experiments were run in a transonic linear cascade wind tunnel. These tests showed a well-behaved, well-mixed film at blowing ratios of 1.2 to 1.4 and density ratios of 1.8 to 2.0. The results showed a general monotonic decrease of both heat transfer coefficient and film cooling effectiveness along the suction side surface. Furthermore, it was seen that the heat transfer coefficient increased significantly with the introduction of film cooling. This research performed measurements only at one design condition of blowing and density ratios.

A closer approximation of engine geometries was accomplished by research at the University of Oxford by Guo et al. [10]. Experiments were performed on heavily film-cooled nozzle guide vanes in a transonic annular cascade facility. These experiments used thin-film gauges to measure a transient surface temperature history and back out the heat transfer coefficient and film cooling effectiveness. The results indicated a scatter of data for both the film cooling effectiveness and heat transfer coefficient profiles. The explanation for the strange profile was that the coolant film lifted off the blade surface. A closer distribution of gauges was needed to understand

the details of the coolant phenomenon.

Another step in experimental approximations to engine environments is a rotating facility. Research was performed by Epstein et al. [1] at Massachusetts Institute of Technology using a fully cooled transonic turbine blade in a short duration rotating facility. Measurements were made with thin film heat flux gauges distributed about the surface of the blade. This showed a notable increase in the heat transfer coefficient between the cooled and uncooled geometries. A comparison was also made between higher blowing ratios (1.24 for the first row of holes) and low blowing ratios (0.96 for the first row of holes). For comparison, our ranges of blowing ratios are from 1.5 to 2.5. The results from this comparison tended to suggest that film liftoff was occurring on the pressure side at the higher blowing ratio but not along the suction side.

Some general conclusions can be drawn from the published literature about both heat transfer coefficient and film cooling effectiveness. The first of these generalizations is that the heat transfer coefficient increases significantly with the introduction of film cooling. Second, film cooling effectiveness generally is reduced with downstream distance from the coolant exits, but in environments that approximate a real engine, effectiveness is inherently a three dimensional phenomenon.

In general, it was difficult to find researchers who were investigating the effect of pressure ratio in a high speed regime with realistic geometries. Epstein et al. [1] did investigate two separate blowing ratios at these realistic conditions.

This literature review attempts to place the Virginia Tech Transonic Wind Tunnel in context with the other experiments that have been performed by the scientific community. The Virginia Tech facility is somewhere in between the most realistic engine approximations (rotating rigs, full coolant scheme) and the more fundamental approximations (flat plate studies, single coolant row).

Chapter 2

Experimental Setup

2.1 Test Conditions

These heat transfer experiments were performed in the Vigrinia Tech Transonic Cascade Wind Tunnel. The test conditions were designed such that they attempted to match relevant engine conditions. A comparison of engine and experimental conditions is summarized in Table 2.1.

Table 2.1: Comparison of Experimental and Engine Conditions

Parameter	Engine	Experiment
Exit Mach Number	Transonic	1.2
Temperature Ratio	2	1.6 ... 2.4
Reynolds Number (based on exit and chord)	5×10^5	3×10^6
Pressure Ratio	1.04	1.02 ... 1.20
Turbulence Level	10% +	1%

The experiments are reasonably close to matching several of the nondimensional parameters of importance. The exit Mach number is transonic as one would expect to see in modern engine designs. The temperature ratio matched for at least

some portion of the tunnel run, and the pressure ratio can be set to reasonable values suggested by General Electric.

It can be seen that the Reynolds numbers are not exactly matched but are close. Perhaps more importantly, the turbulence levels are much lower than one would expect to see in an engine environment. This is a point of note and will be discussed in Chapter 5 as a suggested area of future work.

2.2 Wind Tunnel Facility

All experiments were performed in the Virginia Tech Transonic Cascade Wind Tunnel Facility. This tunnel is a blowdown facility capable of providing run times of approximately 60 sec at the desired test conditions. The wind tunnel provides a freestream flow at 10 psig. Fig. 2.1 is an illustration of the facility.

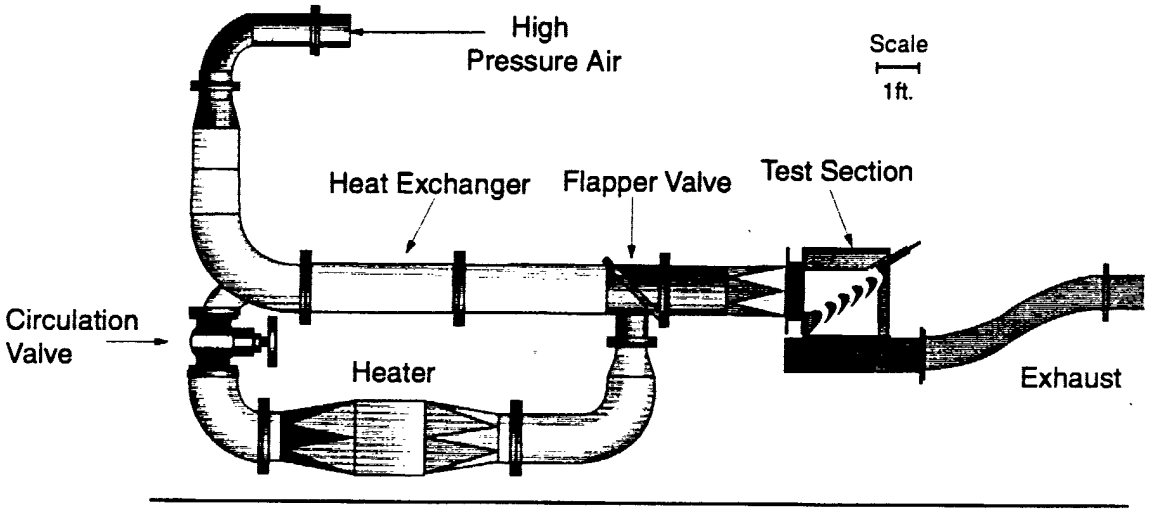

Figure 2.1: Windtunnel Facility

The freestream air for the experiment is provided by two large storage air tanks. The storage tanks are charged to 170 psi by a four-stage Ingersoll-Rand compressor. Before being stored in the tanks, the air is first passed through a dryer to remove water vapor to approximately three percent relative humidity. During a run, the tunnel control value regulates the tank pressure via a tunnel control algorithm to achieve a constant freestream pressure of 10 psig. Before entering the test section, the air is heated as it crosses over a bank of hot copper tubes. After the heated air crosses over the blade cascade it exits to atmosphere.

2.2.1 Heated Flow

The tunnel air is heated by the use of a passive heat exchanger comprised of a bank of copper tubes. This bank of copper tubes is heated before a test run by closing the flapper valve and opening the circulation valve which creates the circulation loop shown in Fig. 2.2. A 36 kW heater and fan then circulates air through this loop. This heats a bank of copper tubes in the upper portion of the loop to a temperature of approximately 130°C. After the tubes have reached this temperature, the heater and fan are turned off and the valves are reopened so the wind tunnel freestream flow can pass through the tubes. During a run, the thermal energy in the tubes is transferred

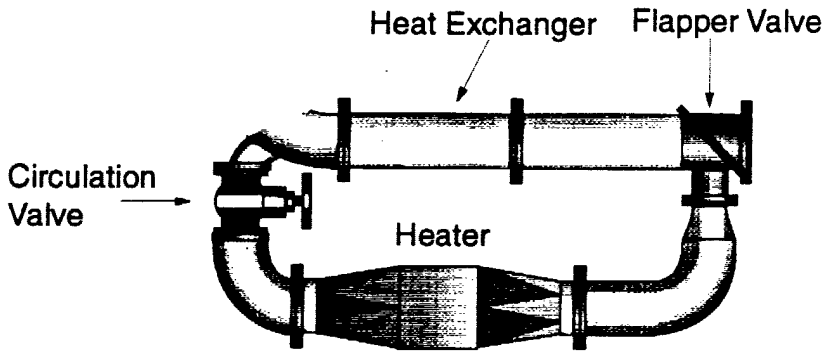

Figure 2.2: Circulation Loop

to the freestream flow. Because the copper tubes cool down during the run, the freestream air also cools. This causes the freestream temperature to vary during a run from about 100°C to 30°C. This changing freestream temperatures provides a range of $\frac{T_\infty}{T_c}$ ratio from about 1.4 to 2.6 during the course of a run.

2.2.2 Tunnel Control

Tunnel control is realized through a control algorithm written in C code. This program utilizes both a feed-back and feed-forward approach. The goal of this algorithm is to maintain the freestream pressure at a desired objective pressure. The objective pressure for all tests was 10 psig. The feed-forward portion of the code determines an initial opening position for the valve and a general profile for value position as a function of time. This general assumed position profile is then corrected via a pressure feedback from a Pitot probe located just before the test section and the objective pressure. This algorithm was able to keep $\frac{P_{obj}}{P_\infty}$ between 0.90 and 1.10 over a duration of approximately 20 seconds. Fig 2.3 is a graph of a pressure control for a typical run.

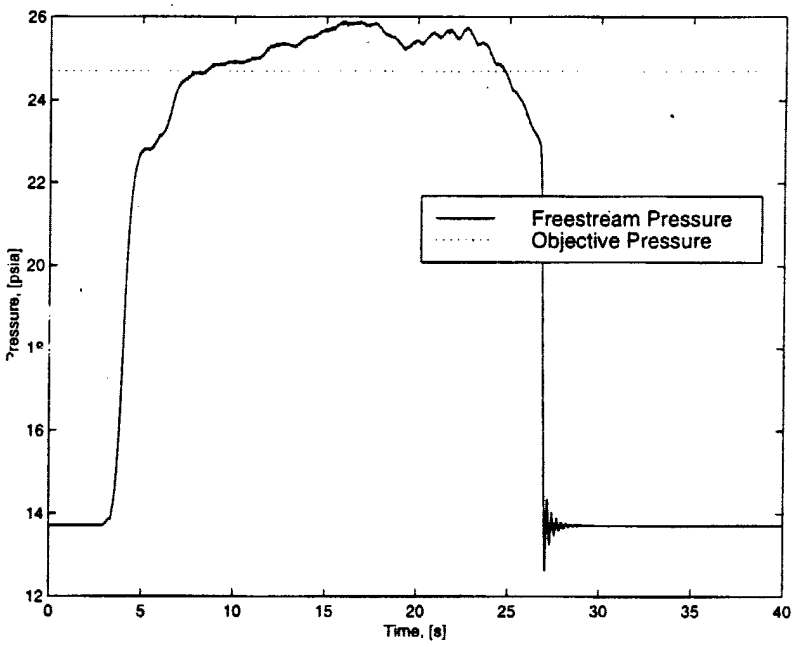

Figure 2.3: Typical Pressure Control During a Run

2.2.3 Test Section

The test section holds four full blades and two half blades for a total of five flow passages. Fig. 2.4 illustrates the blades in place. Only the center blade of the cascade is equipped with instrumentation. The blades have a 13.72 cm (5.4 inch) chord length and a 15.24 cm (6 inch) span. Flow enters the test section at Ma=0.3. goes though a high turning angle of 128°, and exits at Ma=1.3.

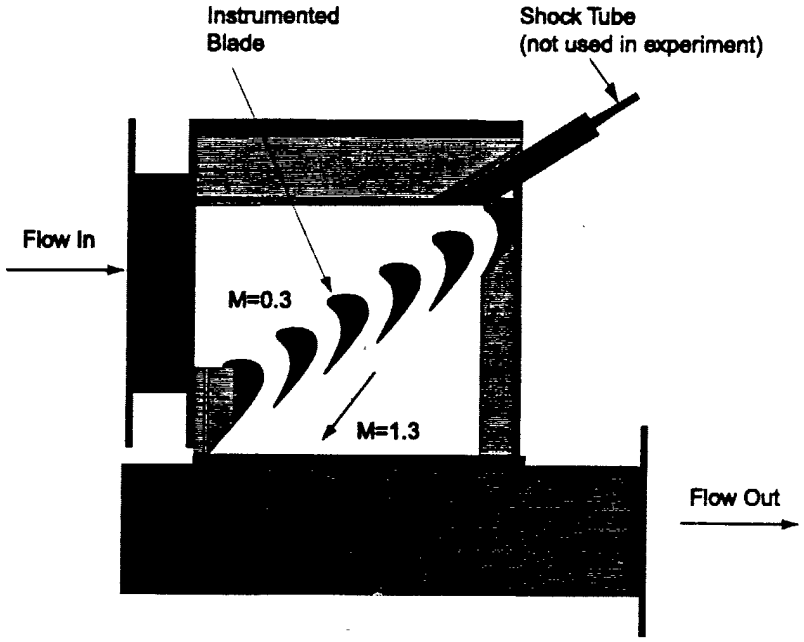

Figure 2.4: Test Section Schematic

The endwalls of the test section are made of one inch thick plexiglas to allow for flow visualization experiments to be performed. These plexiglas endwalls are then reinforced by one inch thich aluminum sidewalls. Fig. 2.5 shows the assembled casacade test section hardware.

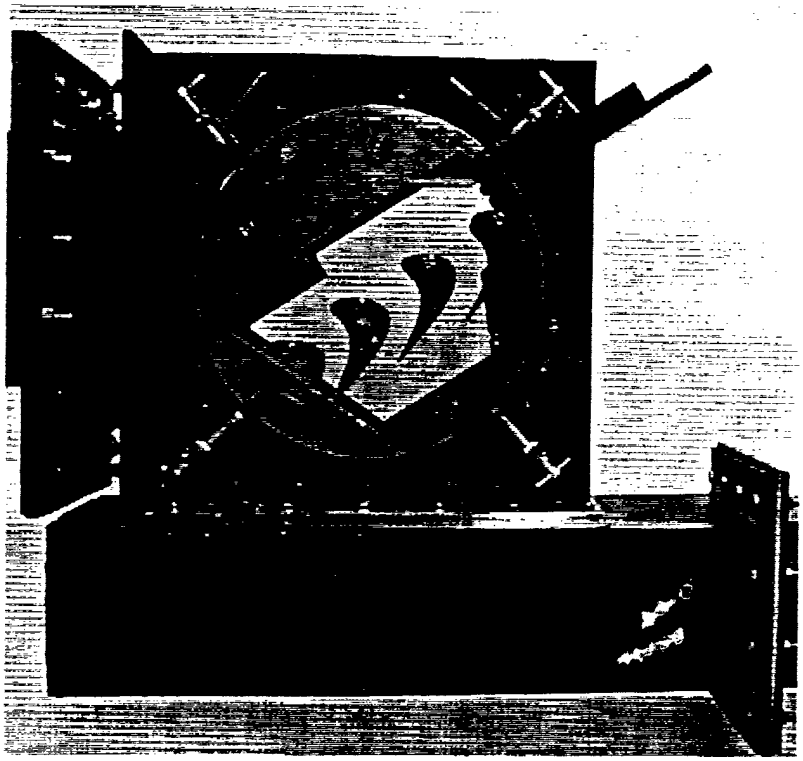

Figure 2.5: Turbine Cascade and Test Section

2.3 Cooling and Blade Design

2.3.1 Blade Design

The blade profile is inspired by a generic General Electric Aircraft Engines first stage turbine blade. Design and measured Mach number profiles are shown in Fig. 2.6.

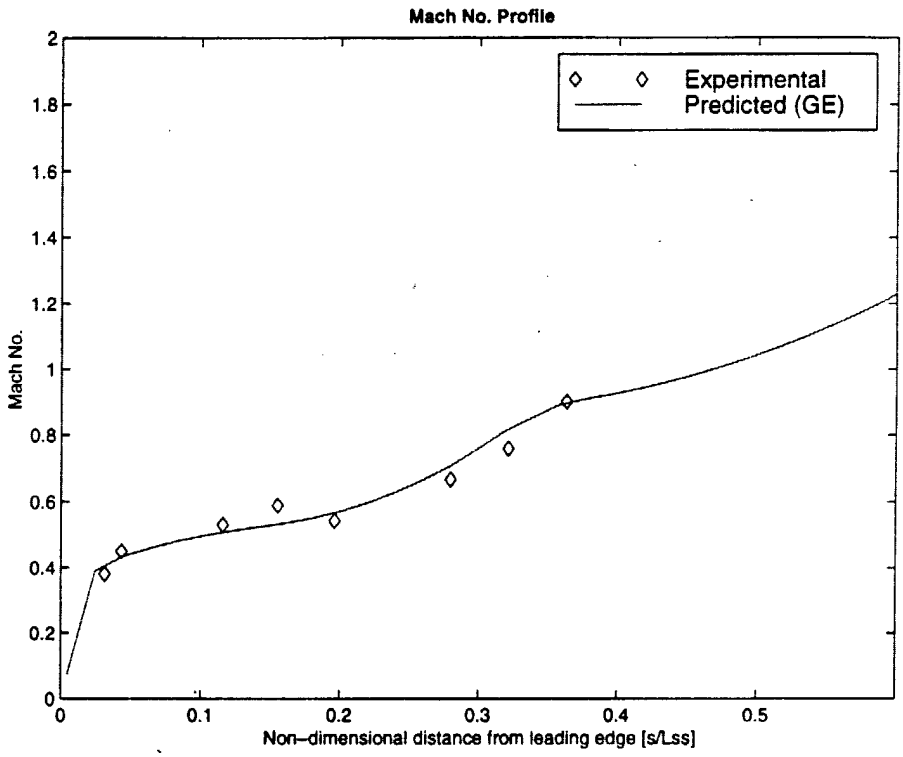

Figure 2.6: Mach Number Profile

The measured Mach numbers are from three pressure taps at the suction side coolant exits and five of the six (transducer 3 was broken) tranducers at the gauge locations. See Sec. 2.4.5 for descriptions of these transducers. The predicted Mach number profile was provided by General Electric for this blade.

Another check that the blade design was operating as expected was performed with shadowgraph visualization. The techniques for the shadowgraph photography are detailed in Sec. 2.4.1. Fig. 2.7 shows the blades without the film coolant running. From this figure it can be seen that the flow is rather periodic in the three full passages.

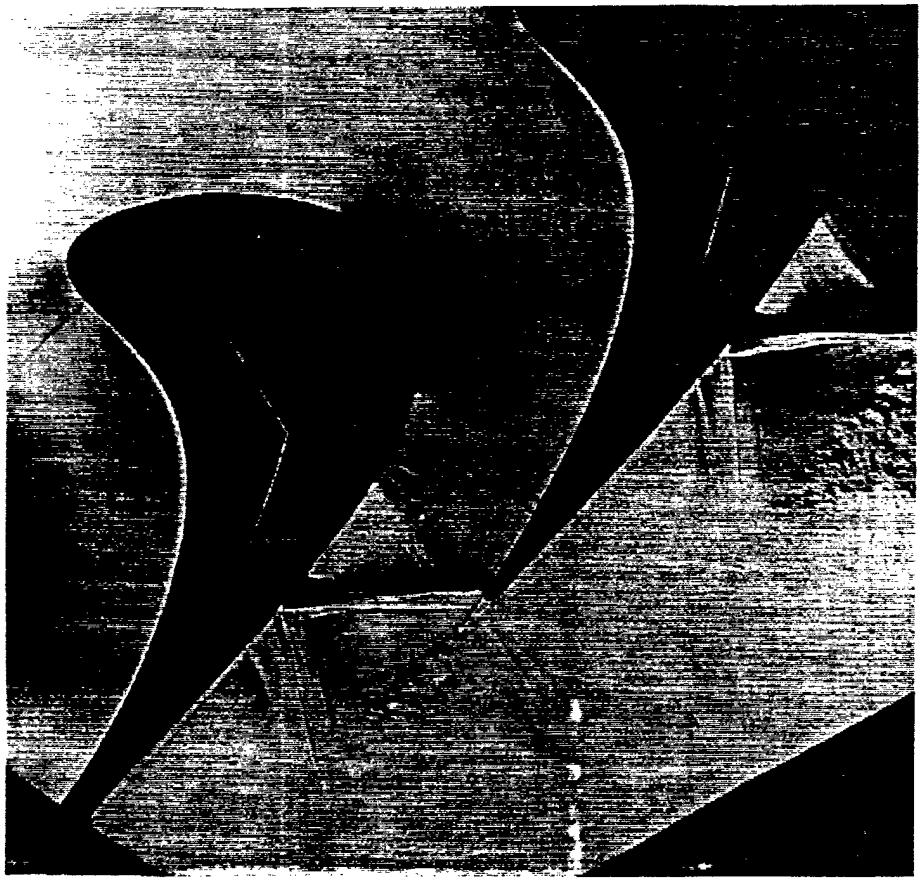

Figure 2.7: Shadowgraph of Blade Passages

Furthermore, the angles of the trailing edge shocks are equal, implying equal exit velocities. The last passage can be seen to have very non-uniform flow, but this is to be expected as it is not a full passage.

2.3.2 Coolant Design

2.3.2.1 Coolant Geometry

The coolant scheme was also inspired by a generic General Electric design. This film cooling scheme consists of six rows of coolant holes. The holes are 10.4 mm (0.041 inches) in diameter with a 91.4 mm (0.360 inches) spacing (a 8.78 $\frac{s}{D}$ ratio). The coolant locations from suction side to pressure side are referred to as Suction Gill (SG), Suction Nose 2 (SN2), Suction Nose 1 (SN1), Nose (N), Pressure Nose (PN), and Pressure Gill (PG) and will be referred to as such from this point. The locations and descriptions are shown in Fig. 2.8. In order to keep the coolant film layer from lifting off the surface of the blade, the coolant holes at locations SN1, SN2, N, and PN are all angled in the spanwise direction by 30°. The coolant holes at locations SG and SN are not angled in the spanwise direction but angled in the streamwise direction by 45° to the surface. Figure 2.9 illustrates the coolant angles.

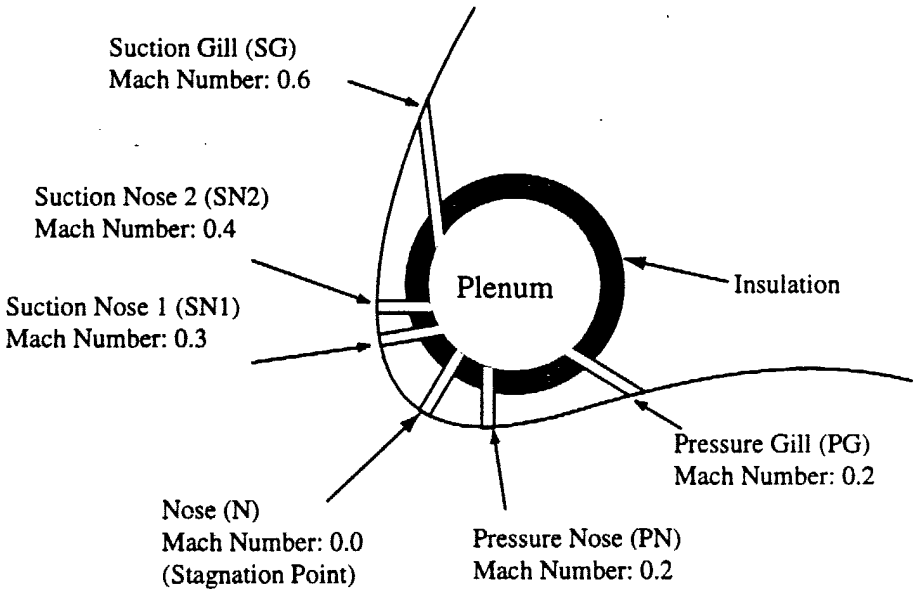

Figure 2.8: Coolant Design

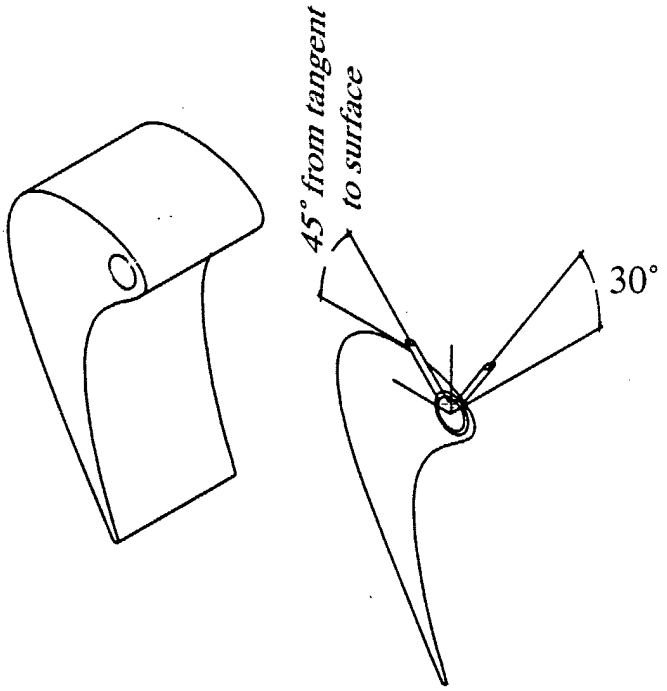

Figure 2.9: Cooling Angles

2.3.2.2 Coolant Air Supply

Coolant air is supplied to the blade by the system of hardware that is illustrated in Fig. 2.10.

The air is supplied to the large storage tank by an Ingersoll Rand compressor, dryer, and filter combination. These three components are pictured in Fig. 2.11. The compressor is an Ingersoll Rand 2475N5 5HP, two stage, reciprocating compressor and provides pressurized air at 175 psi at a rate of 16.8 ambient cubic feet per minute. The dryer is an Ingersoll-Rand HRM regenerative dryer that dries the air to below four percent relative humidity. Finally the air passes through an Ingersoll-Rand filter that removes any dirt particles before being stored in a large storage tank. The exit

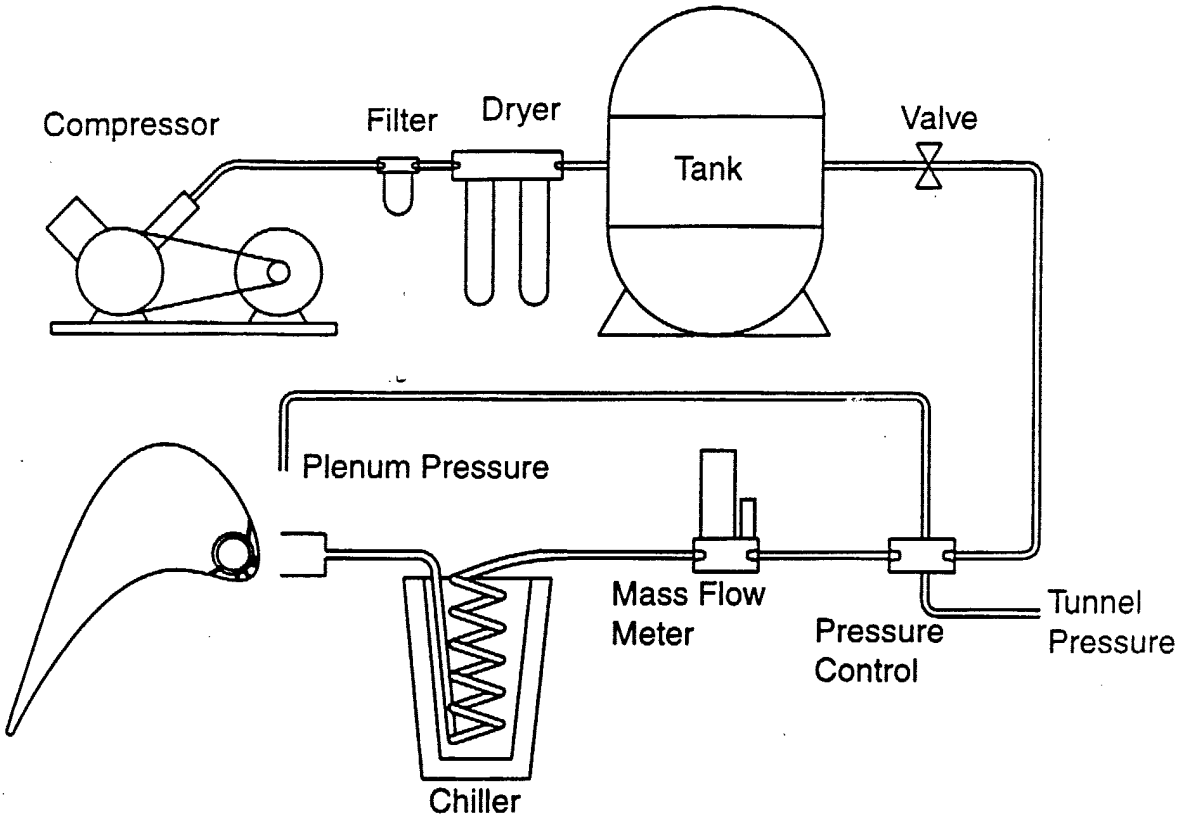

Figure 2.10: Coolant Supply Schematic

flow from the storage tank is regulated by an on/off ball valve.

From the ball valve, the air passes through the coolant pressure control system. The coolant control system was an added improvement from previous research at the same facility. This addition was necessary to be able to control the pressure ratio of the coolant reliably, accurately, and over a wide range of values. A description of this control system is given in Sec. 2.3.2.3.

After the control system, the air passes through an orifice plate to measure the mass flow of coolant. A description of this measurement device is given in Sec. 2.4.6. Next, the air passes through a chiller to cool the air to get the appropriate temperature ratio. The chiller is pictured in Fig. 2.12. It is simply a copper coil emersed in a styrofoam container filled with liquid nitrogen. The level of the nitrogen is regulated manually by a hand valve from the nitrogen supply tank.

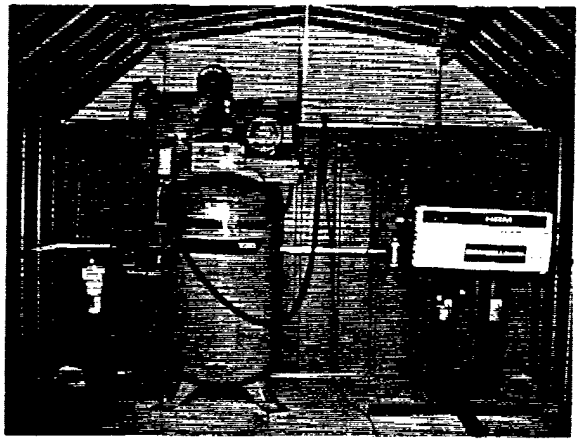

Figure 2.11: Compressor, Dryer, Filter combination

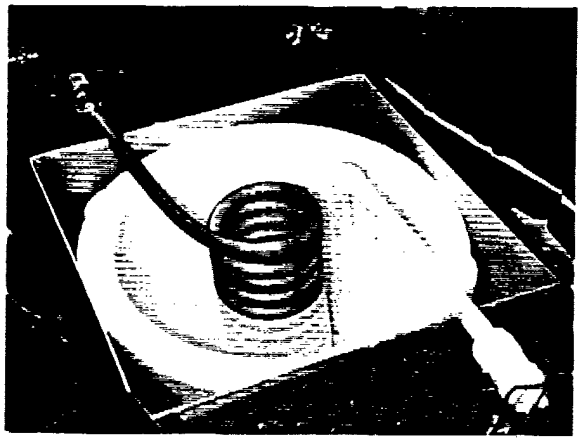

Figure 2.12: Liquid Nitrogen Chiller

Lastly, the chilled air enters the plenum and exits the coolant holes on the blade.

2.3.2.3 Coolant Control

The coolant control schematic is shown in Fig. 2.13. This system is what maintains a constant pressure difference between the plenum and freestream total pressures throughout the tunnel run. The heart of this control system is a simple integrating circuit, which was able to maintain the pressure ratio at the values needed.

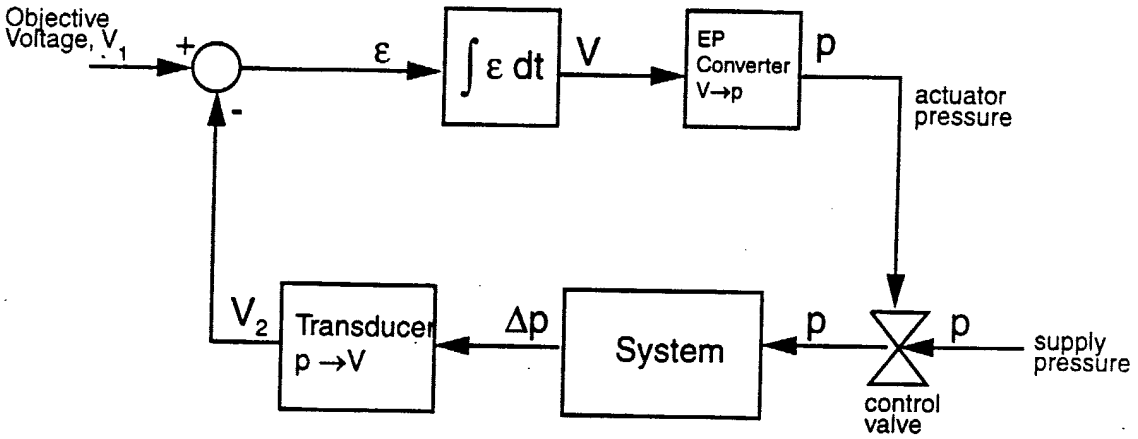

Figure 2.13: Coolant Control System Schematic

The first step in this control schematic is to set the objective delta pressure using the objective voltage, V_1. This voltage is created simply by a battery and a voltage divider circuit with a potentiometer. The signal from the feedback delta pressure, V_2, is given by a transducer which has a linear output where pressure in psi outputs directly as volts. In other words, if the desired delta pressure is 2 psi, the objective voltage is set to 2 V.

This objective voltage is then subtracted from the actual feedback voltage by the use of an op-amp difference amplifier. This difference amplifier is detailed in Fig. 2.14. The first two op-amps in this schematic constitute the difference amplifier portion of the control circuit. This circuit yields the inverted difference between the

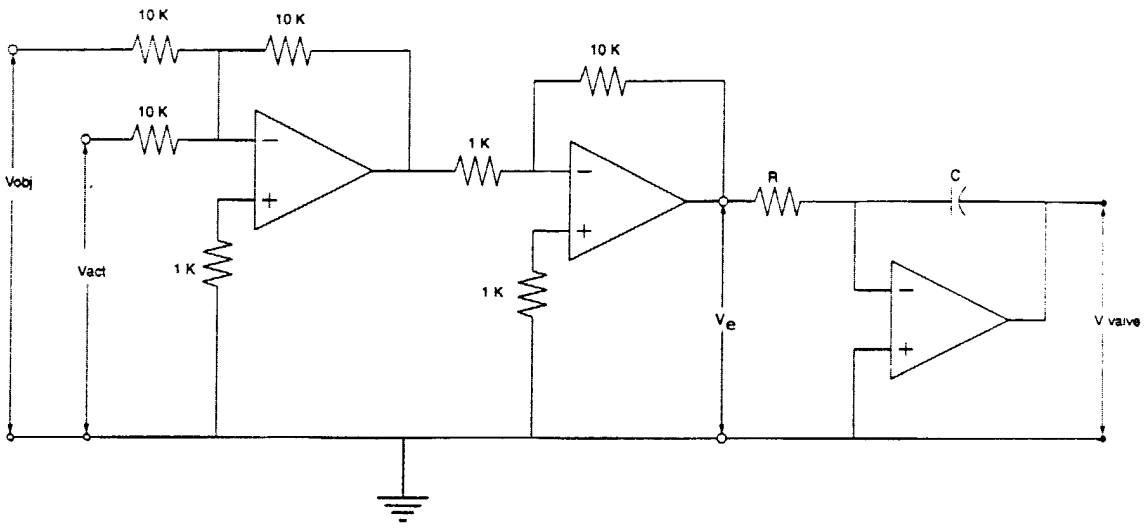

Figure 2.14: Coolant Control Circuit

actual and objective voltages by the simple relationship,

$$V_\varepsilon = -(V_{act} - V_{obj})$$

The second portion of this control circuit is the integrating op-amp circuit. It provides a control voltage for the control valve, V_{valve}. The intergator circuit integrates the error signal by the equation,

$$V_{valve} = \frac{-1}{RC} \int_0^t V_\varepsilon \, dt$$

In this equation, the $\frac{1}{RC}$ term is often referred to as the integrator "gain". This term controls the slope of the control output. In the control apparatus, the value of the integrator gain was adjusted by using a set capacitance and a potentiometer. An appropriate tuning of the control system provided a quick rise time with little overshoot. Both the difference amplifier portion and the integrating portion of this circuit are inverting amplifiers, so the end result is a non-inverted output. Two good references for op-amp designs are Jung [15] and Mims [12]. An example of the control that was achieved is shown in Fig. 2.15. It is important to comment here that this system controls the coolant to freestream pressure difference rather than the pressure ratio. Over the ranges of the tunnel runs, however, this type of control yielded a very constant pressure ratio as well as pressure difference.

Following Fig. 2.13, the integrated error signal is then routed into an electro-pneumatic converter, and the voltage is converted into an actuating pressure for a proportional valve. The proportional valve is a Research Control Valve Model 4 Type B1RA valve from Badger Meter, Inc. This actuator valve is a proportional pneumatically driven valve that regulates the air flow from the large coolant storage tank to the rest of the coolant system. This actuator valve opens or closes in proportion to the pressure supplied to it from the electro-pneumatic converter. After the air leaves the control valve, it enters the rest of the cooling system, namely the chiller and the plenum, which in turns creates a real pressure difference that is measured and used as feedback to close the control loop.

If the feedback pressure is higher than the objective pressure, the error signal is negative, the integrated signal starts to decrease and the actuator valve starts to close. The opposite occurs if the feedback is lower than the objective. An illustration of typical coolant pressure control is shown in Fig. 2.15.

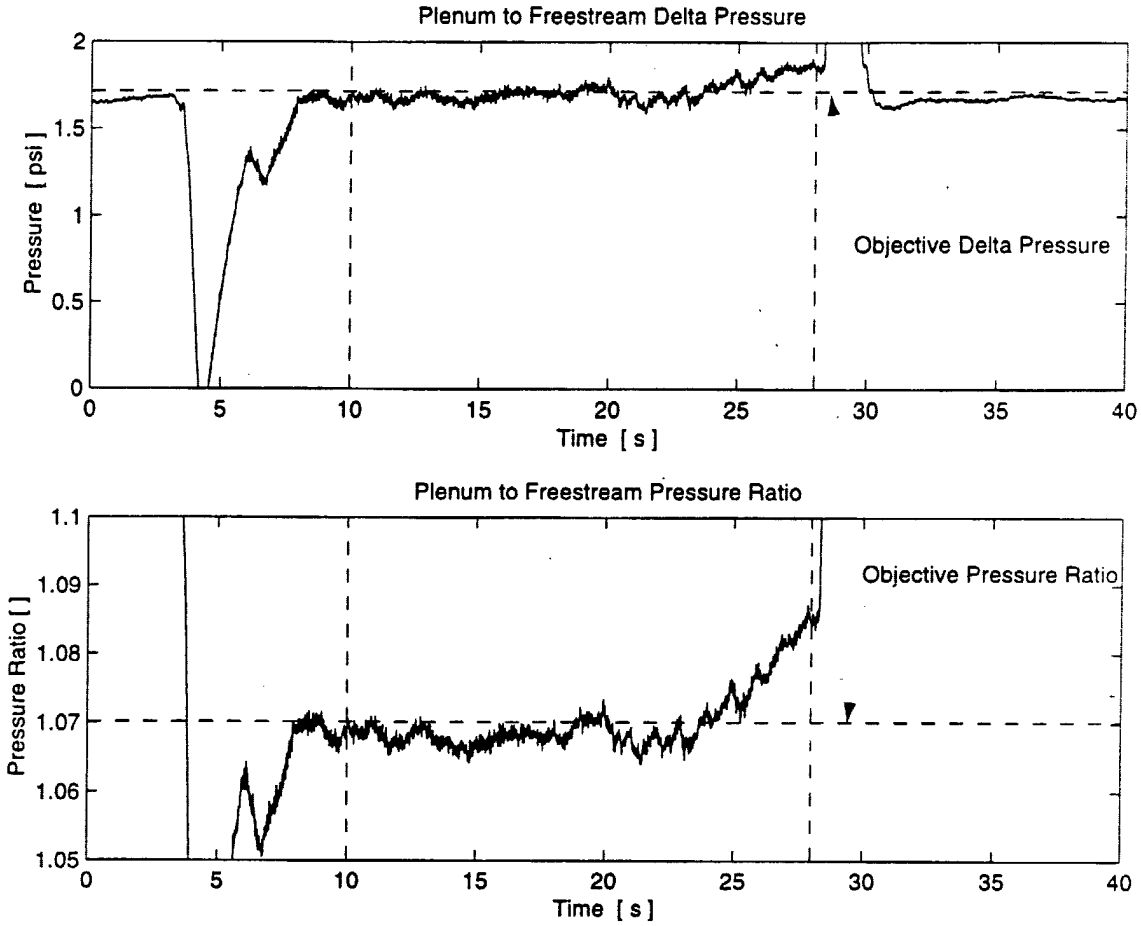

Figure 2.15: Typical Coolant Control

2.4 Instrumentation

2.4.1 Optical Techniques

Two types of optical visualizations were performed; Schlieren and shadowgraphs. A brief overview of the two techniques is given in this section but for a detailed discussion of these and more detailed descriptions of our apparatus see Grabowski [9]. Both techniques use a similar set-up depicted in Fig. 2.16. For the Schlieren pho-

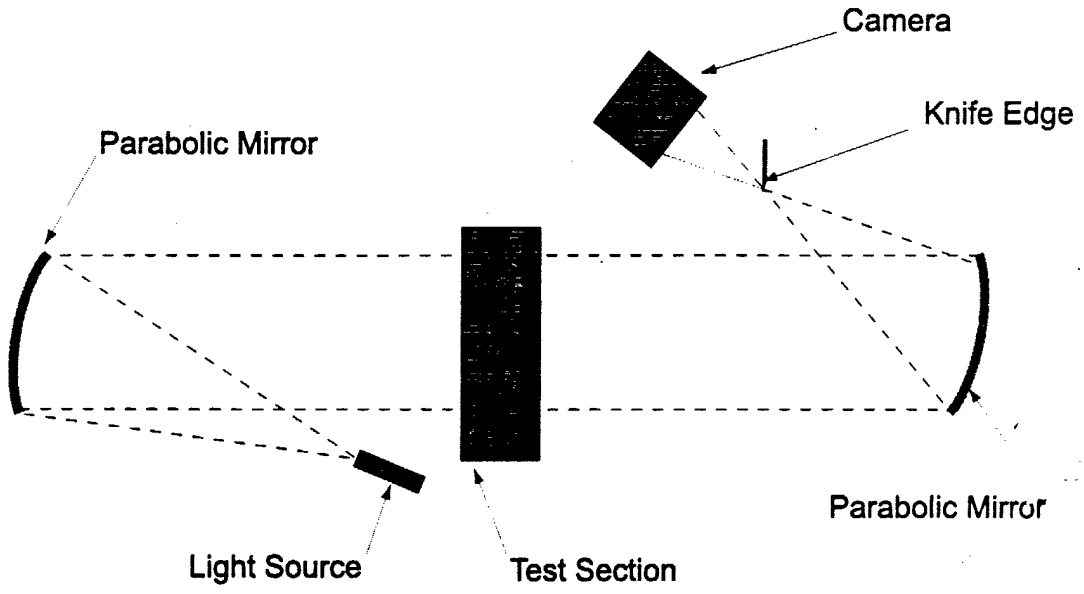

Figure 2.16: Optical Set-up

tographs, the light source is a slot, and a knife edge is placed at the second focal point as shown in this figure. This visualization yields the gradient of density normal to the knife edge direction. The shadowgraph visuaization, on the other hand, uses a point light source and no knife edge. This type of photograph shows the second derivative of density.

2.4.2 On-Blade measurements

The instrumented blade is equipped with numerous transducers. In order to facilitate the installation of all the sensors, the blade was manufactured in two halves. These two halves are pictured in Fig. 2.17. The first half is the pressure side which contains the plenum and cooling passages and instrumentation coolant transducers. The second half is the suction side and it contains six sets of triplet (pressure, heat flux, and temperature) gauges. These triplet gauges are staggered down the chordwise

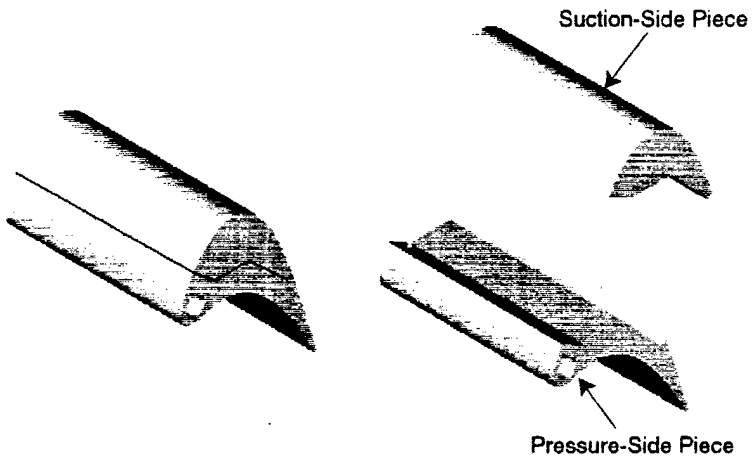

Figure 2.17: Blades Halves

direction at a spacing of 0.41 inches and across the spanwise direction at a spacing of 0.50 inches. The locations of these triplet gauges with respect to the coolant exits and to each other is depicted in Fig. 2.18. A picture of the actual hardware is shown in Fig. 2.19.

A diagram of all of the on-blade measurements is shown in Fig. 2.20. Table 2.2 complements this figure by summarizing the on-blade measurements.

At six separate locations along the chord of the blade (locations 1 through 6) there are triplet gauge groups. The temperature is measured with a K-type surface

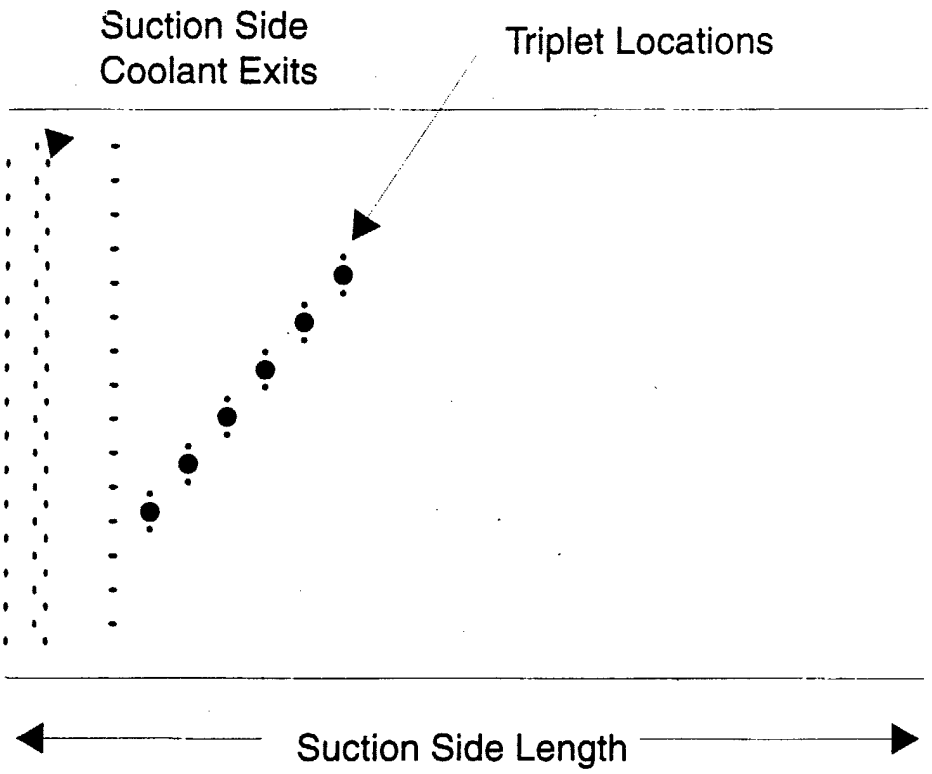

Figure 2.18: Suction Side Plan View

thermocouple mounted flush to the blade surface. The pressure measurement is made with a *Kulite* XCQ-062-50 pressure transducer. Finally, the heat flux measurement is made with a *Vatell* HFM-7 heat flux microsensor.

In addition to these triplet gauges along the blade surface, a number of measurements were made at the coolant exits. At each of the six coolant exit rows, static pressure and coolant exit temperature are measured using *Lucas* NPC-410 pressure sensors. These pressure taps are metal tubes inserted so that they are flush to the blade surface. The tap location is 1 cm (0.39 inches) from the sidewalls. Flow vi-

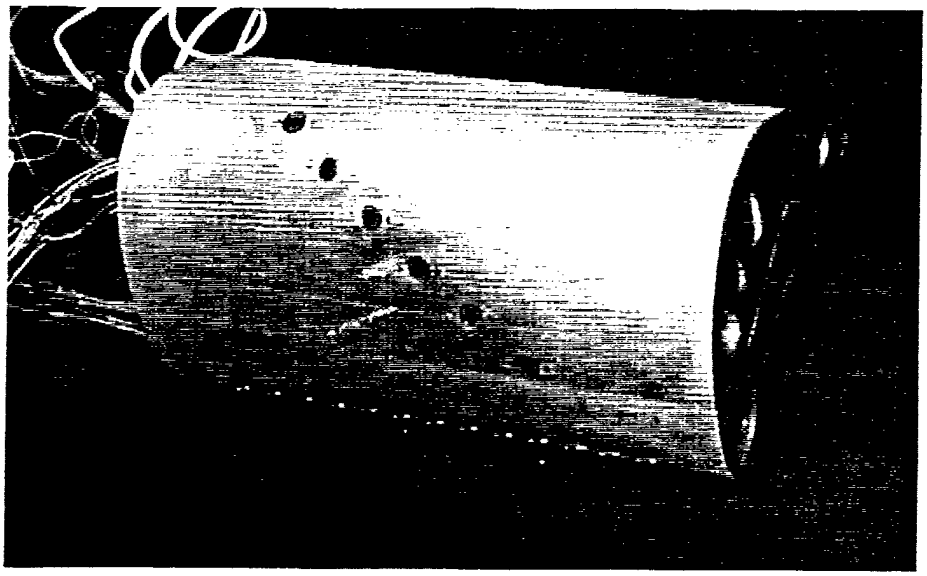

Figure 2.19: Instrumented Blade

sualization experiments showed that this distance is sufficiently outside the endwall secondary flows. The thermocouple measurements are made with a small (36 gauge) K-type thermocouple bead just protruding into the coolant flow passage of the coolant hole closest to the endwall. Fig. 2.21 illustrates this configuration.

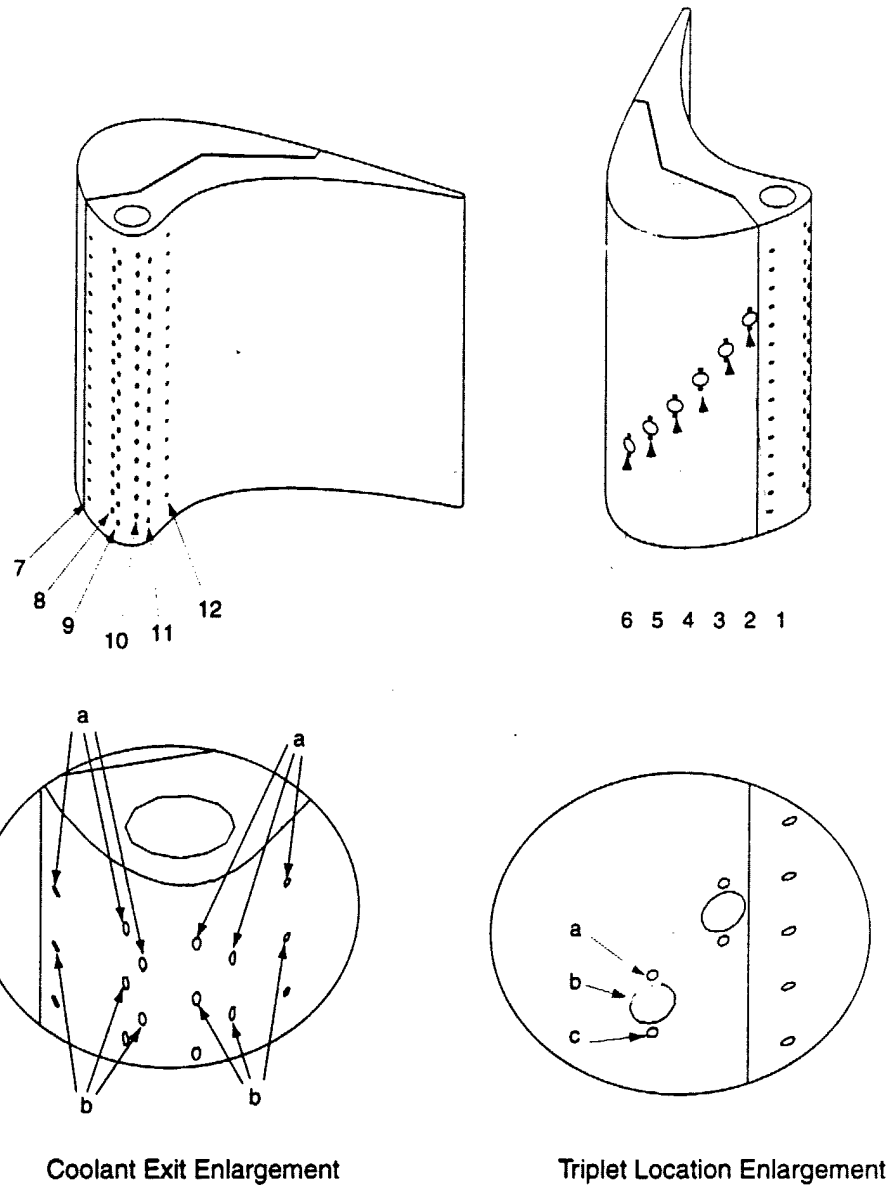

Figure 2.20: Blade Instrumentation Scheme. See Table 2.2 for Location Descriptions

Table 2.2: On-Blade Measurements

Location	Measurement	Device
1a	Heat Flux and Temperature	*Vatell* HFM
1b	Static Pressure	*Kulite* Transducer
1c	Temperature	Thermocouple
2a	Heat Flux and Temperature	*Vatell* HFM
2b	Static Pressure	*Kulite* Transducer
2c	Temperature	Thermocouple
3a	Heat Flux and Temperature	*Vatell* HFM
3b	Static Pressure	*Kulite* Transducer
3c	Temperature	Thermocouple
4a	Heat Flux and Temperature	*Vatell* HFM
4b	Static Pressure	*Kulite* Transducer
4c	Temperature	Thermocouple
5a	Heat Flux and Temperature	*Vatell* HFM
5b	Static Pressure	*Kulite* Transducer
5c	Temperature	Thermocouple
6a	Heat Flux and Temperature	*Vatell* HFM
6b	Static Pressure	*Kulite* Transducer
6c	Temperature	Thermocouple
7a	Static Pressure	Lucas Sensor
7b	Temperature	Thermocouple, AMUX-64T
8a	Static Pressure	Lucas Sensor
8b	Temperature	Thermocouple, AMUX-64T
9a	Static Pressure	Lucas Sensor
9b	Temperature	Thermocouple, AMUX-64T
10a	Static Pressure	Lucas Sensor
10b	Temperature	Thermocouple, AMUX-64T
11a	Static Pressure	Lucas Sensor
11b	Temperature	Thermocouple, AMUX-64T
12a	Static Pressure	Lucas Sensor
12b	Temperature	Thermocouple, AMUX-64T
Plenum	Temperature	Thermocouple, AMUX-64T
Plenum	Total Pressure	Lucas Sensor

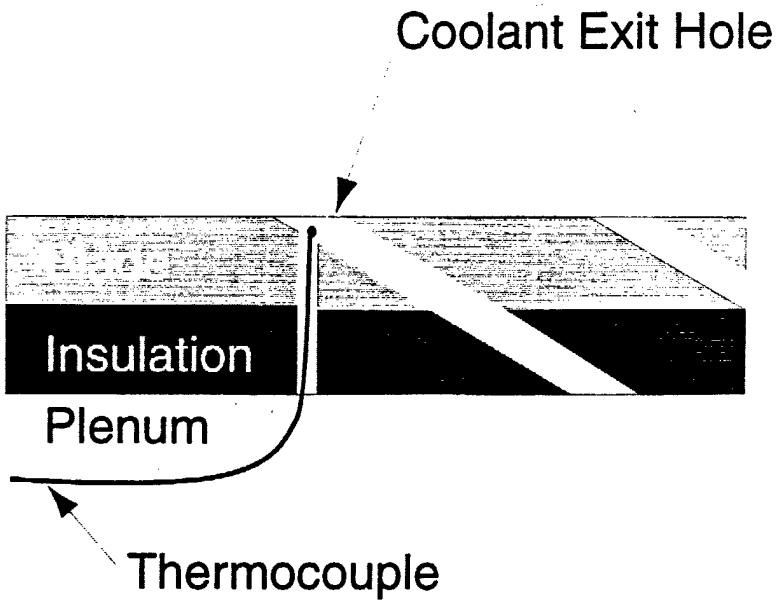

Figure 2.21: Coolant Temperature Thermocouple

2.4.3 Off-Blade Measurements

The off-blade measurements made are summarized in Table 2.3.

Table 2.3: Off-Blade Measurements

Location	Measurement Device
Orifice Total Pressure	Lucas Sensor
Orifice Delta Pressure	Lucas Sensor
Orifice Line Temperature	Thermocouple, AMUX-64T
FreeStream Total Pressure	Lucas Sensor
FreeStream Temperature	Thermocouple, AMUX-64T

2.4.4 Heat Flux Measurements

Heat flux measurements were taken by *Vatell* Heat Flux Microsensors (HFM). The active sensor area is 4 mm in diameter. This sensor is actually comprised of two separate devices, a Heat Flux Sensor (HFS) and a Resistance Temperature Sensor (RTS). Figure 2.22 is a picture of the HFM.

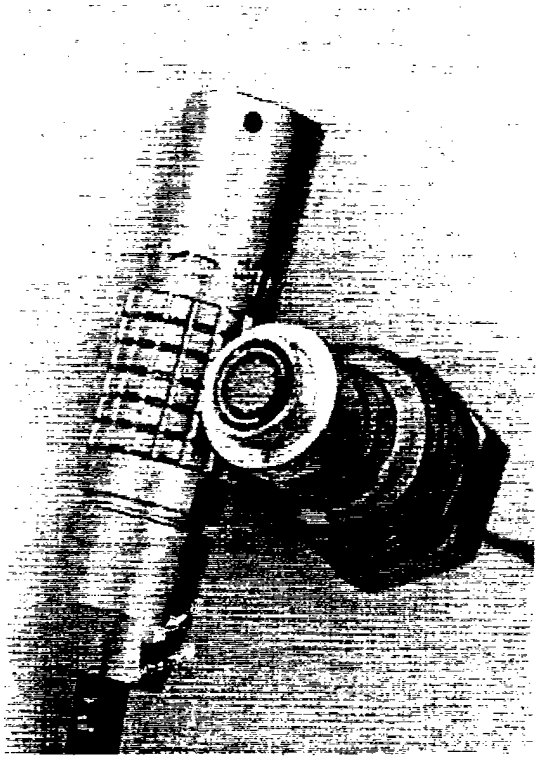

Figure 2.22: Heat Flux Microsensor (Courtesy *Vatell*)

A thorough discussion of the phenomenon that comprise this type of heat flux gauge is giver by Diller [4]. A basic understanding of the gauge physics follows. The HFS works by measuring a temperature difference over a thin resistance layer. The differential temperature across the substrate is measured by a thermopile of thermocouples. The thermopile has 280 Nichrome/Constantan thermocouple pairs deposited in a serpentine pattern along the gauge face. Conduction through this

thin-film sensing layer is described by Fourier's Law,

$$q'' = k\frac{\Delta T}{t}$$

where q'' is heat flux, k is the thermal conductivity, t is the thickness, and ΔT is the temperature difference across the sensing layer. A calibration procedure yields a value of $\frac{k}{t}$ so that the measured thermalcouple voltage of ΔT is converted into a heat flux value by using a gauge sensitivity. Over the temperature ranges that our experiments are being performed, it is assumed that the heat flux sensitivity is constant, so that actual heat flux can be calculated using,

$$q'' = \frac{VG}{S}$$

where V is HFS voltage, G is amplifier gain, and S is gauge sensitivity. Over higher temperature ranges the gauges have a sensitivity to temperature. This temperature dependence is typically corrected for with the RTS portion of the HFM, but for our application this effect is ignored. The calibrated coefficients that corrected for the temperature dependence were extremely small and over the ranges of temperature of our experiments were insignificant.

The sensitivities of each gauge are determined by a number of calibration tests. An extensive study of different calibration schemes is given by Smith et al. [23]. The HFS can be essentially modeled as a first-order system having a time constant of 17 μ s. Experiments have been performed to verify this by Popp [20] and Peabody [19].

The second portion of the HFM is the resistance temperature sensor (RTS). The RTS is a thin-film element deposited surrounding the gauge. It works on the principle that its resistance changes repeatably as a function of temperature. This temperature dependence is generally described by a polynomial fit of the form,

$$T = a \cdot R^3 + b \cdot R^2 + c \cdot R + d$$

where T is temperature, R is RTS resistance, and a,b,c, and d are the coefficients of the polynomial. The coefficients for each gauge are determined through calibration.

The gauge is supplied with a 0.1 mA constant current supply and the voltage is measured which yields resistance from Ohm's Law.

The HFM gauges have a thin (2 microns) thick sensing layer and the substrate of the rest of the gauge is made of aluminum nitride. This material was picked so it would have nearly the same thermal properties as that of the aluminum blade to minimize its disturbance of the thermal phenomenon. The installment of the HFM gauges was done by press fitting the sensor into the blade. This was done in the so that the tight fit would provide good thermal contact with the blade, minimizing the contact resistance that might occur.

2.4.5 Pressure Measurements

2.4.5.1 Kulite Transducers

Static pressure measurements at the six gauge triplet locations were made using *Kultite* XCQ-062-50 high frequency pressure transducers. The transducer is pictured in Fig. 2.23. These transducers are 1.7 mm in diameter. The frequency response of the transducers is 25 kHz. The transducer is based on pizeoelectric materials and gives a voltage linearly proportional to its face pressure. The linear output of the gauge is typically near 2 mV/psi. These transducers were then amplified using *Measurements Group* 2310 amplifiers at a gain of 100. These pressure transducers were selected for their high frequency response for some other experiments that were performed by Popp [20] in the same facility. For the experiments presented in this thesis the transducers were used for low speed measurements only.

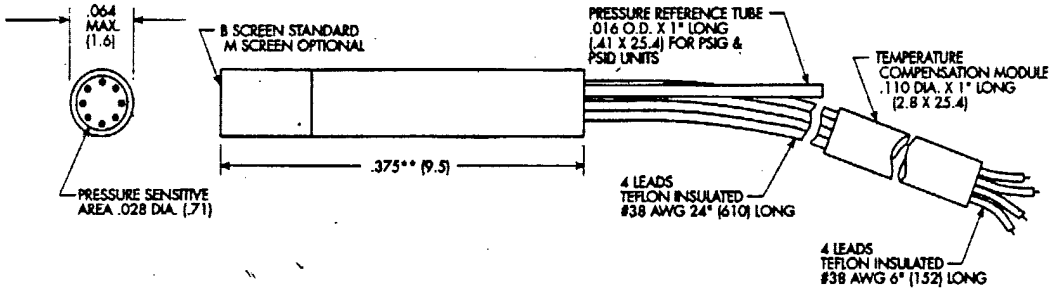

Figure 2.23: *Kulite* Pressure Transducer (Courtesy *Kulite* Inc.)

2.4.5.2 Lucas Transducers

Other low speed pressure measurements of plenum total pressure, freestream total pressure, orifice total pressure, orifice differential pressure, and static pressure were made using a *Lucas* NPC-410 solid state pressure transducer. The transducer

works by the use of a piezoresistive strain gauge integrally formed on a mechanical diaphragm. This resistance is then used as a leg of a wheatstone bridge. Several different transducers with different pressure ranges are used in the experiments.

2.4.6 Coolant Mass Flow

Coolant air mass flow was recorded using an orifice plate pictured in Fig. 2.24. This orifice plate was a Lambda Square orifice plate. In order to use the orifice plate.

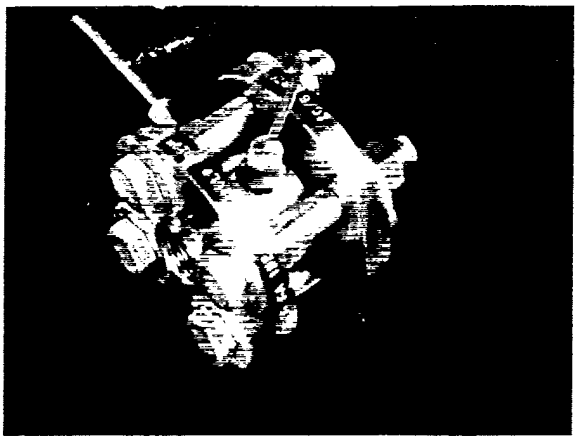

Figure 2.24: Orifice Plate

it is necessary to record line temperature, upstream total pressure, and differential plate pressure. These measurements can then be used with the correlation,

$$\dot{m} = C_d A \sqrt{2\rho\Delta p} \tag{2.1}$$

where, C_d is the discharge coefficient, A is the bore area, ρ is the air density (calculated from line temperature and line pressure), and Δp is the differential plate pressure. A value of 0.62 for C_d was used for this model of orifice plate.

2.4.7 Amplifiers

2.4.7.1 AMP-6

The volatge output from the HFM is amplified using *Vatell* AMP-6 amplifiers. The amplifier provides a 0.1 mA signal to the RTS. The amplifier has two separate gains for both the heat flux signal and the temperature signal. Both must be zeroed by the use of a potentiometer. The AMP-6 has RTS gain settings of 1, 100, 200, and 500. For all experiments the RTS gain setting of 100. The AMP-6 has HFS gain settings of 1, 200, 500, 1000, and 5000. All experiments used an HFS gain setting of 100.

2.4.7.2 Measurements Groups 2310

The *Kulite* signals were amplified with a *Measurements Group* 2310 amplifier. These amplifiers provide both an excitation voltage and measurement of gauges in a wheatstone configuration. The 2310's can provide gains from 1 to 11,000. All experiments used a *Kultie* gain setting of 100.

2.4.8 Data Acquisition

All data acquisition was done using a *National Intruments* AT-MIO-16XE-50 digital data acquisition board and a PC. This board provides eight differential channels of input. In order to increase the number of channels acquired. two *National Instruments* AMUX-64T multiplexer boards were used. These boards both mutiplex four channels apiece which expands the channel count to 64 differential channels. Also the AMUX-64T has a built-in ability to acquire thermocouple signals directly with a temperature compensated electronic ice point. This is the device that was used for all thermocouple measurements.

A *Labview* program was written to acquire all channels. The details of this *Labview* program are given by Smith [22].

Chapter 3

Analysis

3.1 Convective Heat Transfer

Convective heat transfer as described by Eqn. 1.1 is repeated here for clarity.

$$q'' = h \cdot (T_{aw} - T_w) \tag{3.1}$$

where q'' is heat flux, h is the convective heat transfer coefficient, T_{aw} is the adiabatic wall temperature, and T_w is the blade wall temperature. This equation illustrates that heat transfer is directly proportional to a heat transfer coefficient and a driving temperature difference. In this analysis, it is assumed, and has been confirmed by experiment [22], that the heat transfer coefficient is a function of the fluid flow field and independent of the temperatures of the blade and fluid.

The second factor in Eqn. 3.1 is the difference between the blade wall temperature, T_w, and the adiabatic wall temperature, T_{aw}. When this temperature difference is zero, there is no heat transfer to the blade, hence the term "adiabatic" wall temperature.

Eqn. 3.1 is a general expression that can be applied to different flow regimes.

3.1.1 Low Speed Convection

In low speed flows, T_{aw} in Eqn. 3.1 is simply replaced by boundary layer edge temperature, T_e.

$$q'' = h \cdot (T_e - T_w) \tag{3.2}$$

In such a flow regime, the heat transfer coefficient can be determined by measuring q'', T_w, and T_e.

3.1.2 High Speed Convection

In high speed flows, however, the true driving temperature difference must be represented using a recovery temperature, T_r for the adiabatic wall temperature. This recovery temperature takes into account the total enthalpy and the viscous dissipation effects which are neglected in low speed flows. Substituting recovery temperature into Eqn. 3.1 results in,

$$q'' = h \cdot (T_r - T_w) \tag{3.3}$$

The recovery temperature is often found by assuming a recovery factor, r, as defined by,

$$r \equiv \frac{T_r - T_e}{\frac{U_e^2}{2C_p}} \tag{3.4}$$

where U_e is the boundary layer edge velocity, and C_p is the specific heat of air. A further simplification commonly used is to estimate the recovery factor as the cube root of the Prandtl Number for turbulent flow. In the following analysis however,

instead of making this approximation, the recovery temperature has been determined for this test section experimentally. Earlier experiments performed by Smith et al. [22] have shown the recovery temperature to be a simple drop from the boundary layer edge temperature denoted by T_d.

$$T_d = T_{t,e} - T_r \tag{3.5}$$

At each location T_d was measured and the results for this are summarized in Sec. B.1. Knowing the recovery temperature is important in order to extend our analysis to film-cooled heat transfer.

3.1.3 Film-Cooled Heat Transfer

In film-cooling heat transfer, it is convenient to use a nondimensionalized temperature difference rather than the adiabatic wall temperature. This nondimensionalized temperature, η, (repeated from Eqn. 1.2) is defined as,

$$\eta \equiv \frac{T_r - T_{aw}}{T_r - T_c} \tag{3.6}$$

The three temperatures in this expression are: recovery temperature, T_r, adiabatic wall temperature, T_{aw}, and the coolant temperature, T_c. Solving this expression for for T_{aw} yields,

$$T_{aw} = T_r - \eta \cdot (T_r - T_c) \tag{3.7}$$

Substituting this expression into Eqn. 3.1 yields,

$$q'' = h \cdot (T_r - T_w - \eta \cdot (T_r - T_c)) \tag{3.8}$$

3.2 Data Reduction

All of the terms in Eqn. 3.8 are measurable quantities except two important parameters: the heat transfer coefficient, h, and film cooling effectiveness, η. The analysis outlined below is a description of how the raw data is reduced to yield these two parameters.

Fig. 3.1 is a sample test run showing the relevant measurements used in the data reduction. The blade wall temperature is simply measured using the blade

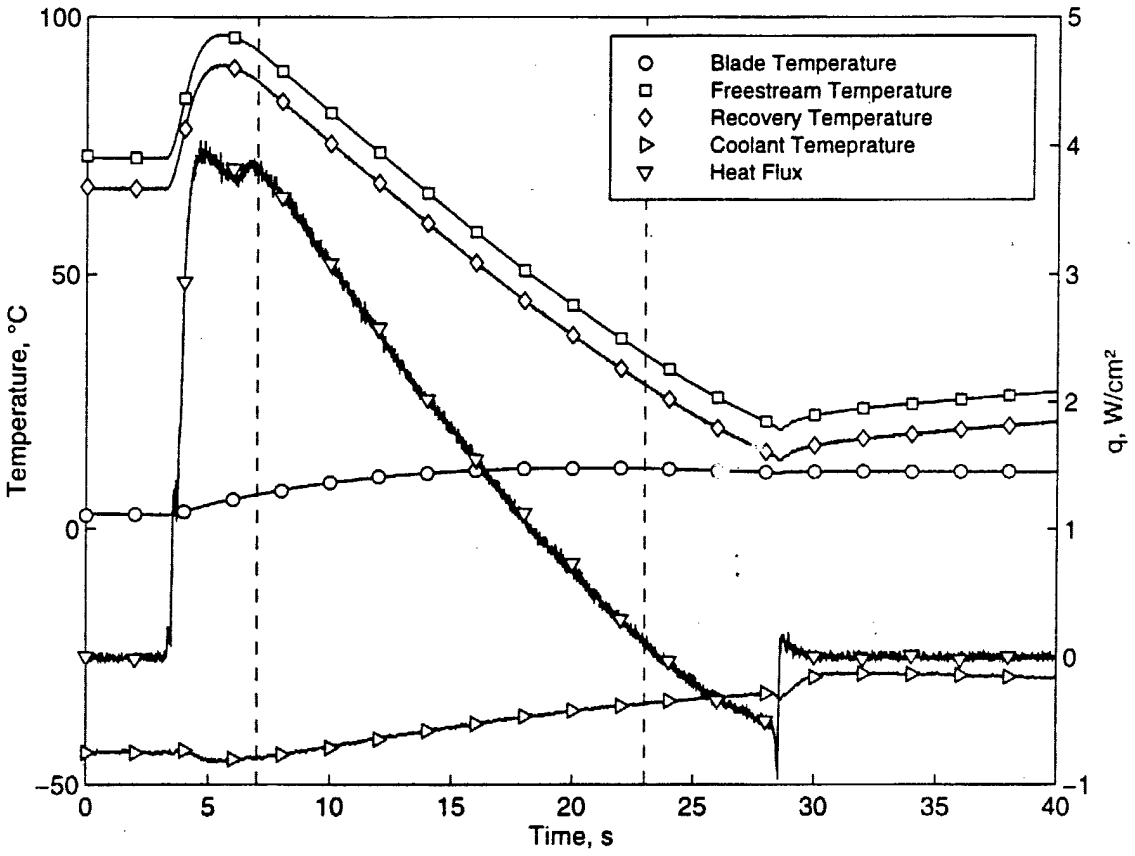

Figure 3.1: Sample Test Run at Gauge 1

thermocouples at each triplet location. The coolant temperature is derived from the coolant exit thermocouples (See Sec. 2.4.2). Since there is a coolant exit thermocouple

for each row of coolant holes, a representative coolant temperature must be found. This was found by using a mass averaged coolant temperature from the exits locations SN1, SN2, and SG. The recovery temperature is found by utilizing Eqn. 3.5 and the data in Appendix B.1. For this representative location on the blade (Gauge 1), the recovery temperature is a drop from the freestream temperature of 6 °C.

It is important to notice that the temperature history is transient. At the beginning of the run the total freestream temperature starts at about 100°C and drops to a final value of about 30°C. The blade temperature stays fairly constant of the course of the run at about 10°C. The coolant temperature also varies somewhat at values near −40°C. This gives a wide range of driving temperature difference to use to evaluate the effectiveness and heat transfer coefficient. In Fig. 3.1 the vertical dashed lines indicate the area over which the analysis is applied. All measured values shown in Fig. 3.1 are from Gauge 1.

The blade wall temperature is simply measured using the blade thermocouples at each triplet location. The coolant temperature is derived from the coolant exit thermocouples (See Sec. 2.4.2). Since there is a coolant exit thermocouple for each row of coolant holes, a representative coolant temperature must be found. This was found by using a mass averaged coolant temperature from the exits locations SN1, SN2, and SG. The recovery temperature is found by utilizing Eqn. 3.5 and the data in Appendix B.1. For this representative location on the blade (Gauge 1), the recovery temperature is a drop from the freestream temperature of 6 °C.

These measured values can now be used to yield the heat transfer coefficient and film cooling effectiveness. In order to do this, it is convenient to rearrange the terms of Eqn. 3.8 by dividing both sides of the equation by $(T_r - T_c)$ to yield,

$$\frac{q''}{T_r - T_c} = h \cdot \left(\frac{T_r - T_w}{T_r - T_c} \right) - h \cdot \eta \tag{3.9}$$

Inspection of this equation shows that it is a linear equation for $\frac{q''}{T_r - T_c}$ and $\frac{T_r - T_w}{T_r - T_c}$ with

a slope of h and y-axis intercept of $h \cdot \eta$. Plotting the data from Fig. 3.1 as in Fig. 3.2 shows the linearity of this relationship. Upon realizing that the experimental data is

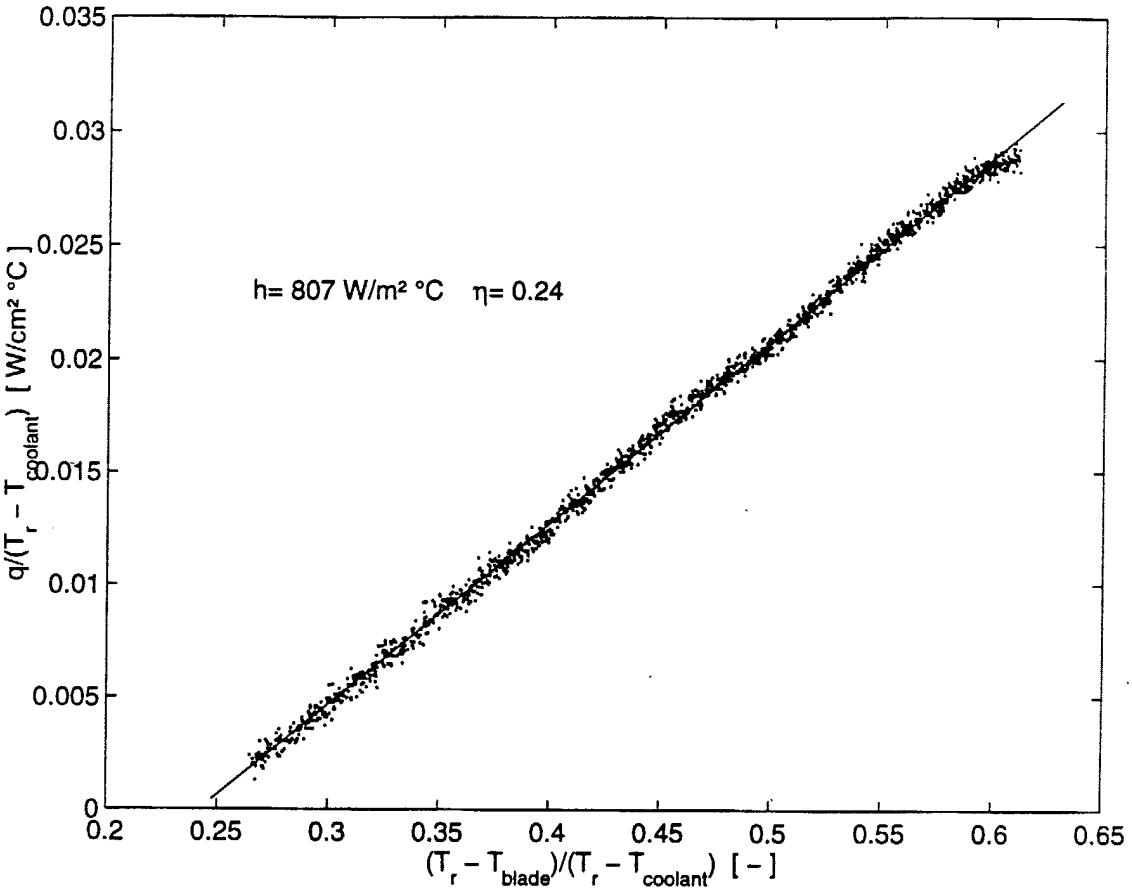

Figure 3.2: Linearized Data at Gauge 1

fairly linear over the range of temperatures, a least-squares regression analysis was applied. The slope of the least-squares fit of the data yields a heat transfer coefficient (807 W / m^2 °C for the example case shown in Fig 3.2) and the x-intercept yields the film cooling effectiveness (0.24 for this example case).

The above outlined method was used to reduce the data from numerous runs at all locations to get both a heat transfer coefficient and a film cooling effectiveness.

After having performed the analysis illustrated in Fig. 3.2, the adiabatic wall

temperature can be determined from Eqn. 3.7. In order to visualize the adiabatic wall temperature over the course of the run it is necessary to assume the film cooling effectiveness is constant. Using this assumption along with Eqn. 3.7 gives rise to the plot of adiabatic wall temperature as shown in Fig. 3.3.

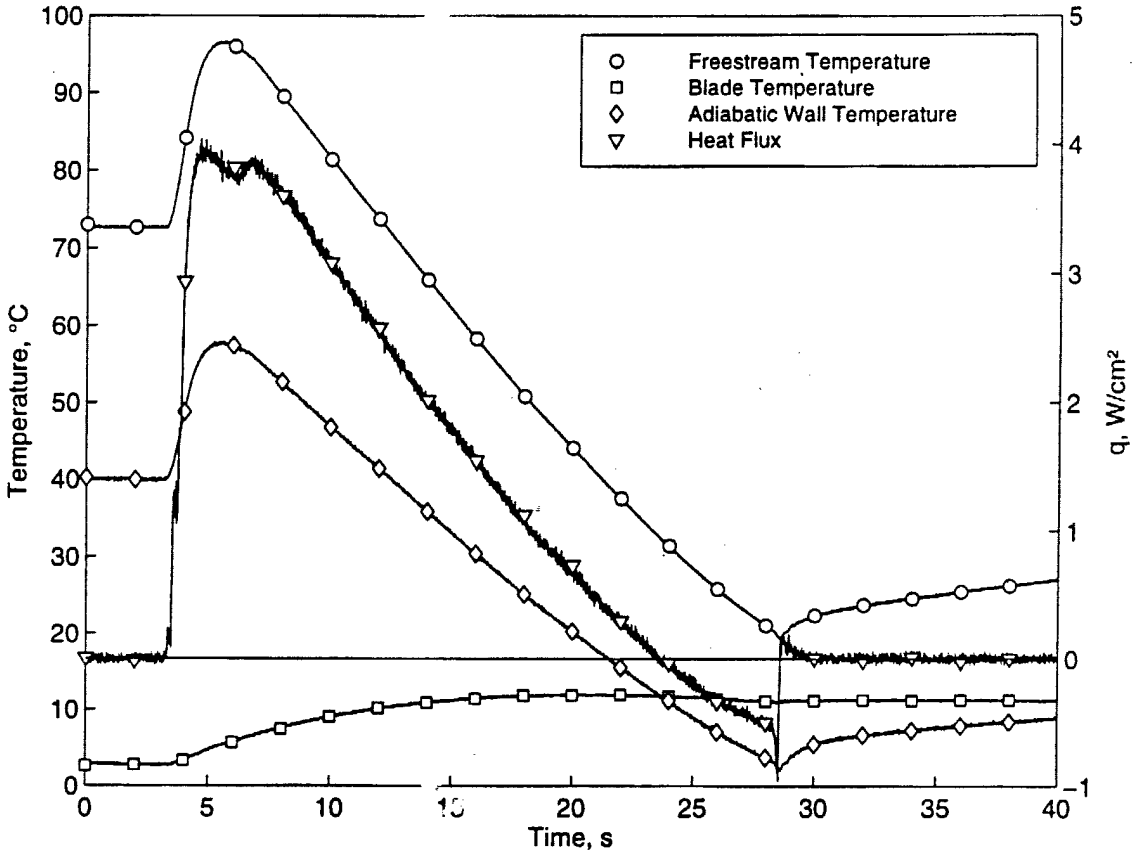

Figure 3.3: Adiabatic Wall Temperature at Gauge 1

This analysis illustrates a few important ideas. The first is that the effect of film cooling is to lower the adiabatic wall temperature significantly. In this sample run, the adiabatic wall temperature is approximately 40°C below the freestream temperature. A second idea illustrated in Fig. 3.3 is that the measured heat flux goes to zero when the adiabatic wall and blade wall temperatures cross. This fact is not surprising but serves as a nice "sanity" check for the data reduction scheme presented.

The analysis illustrated in Fig. 3.2 yields an average heat transfer coefficient over the analysis time. If one still makes the assumption that the film cooling effectiveness is constant, the time varying heat transfer coefficient can backed out from Eqn. 3.8. This yields Fig. 3.4. This figure shows that the heat transfer coefficient is

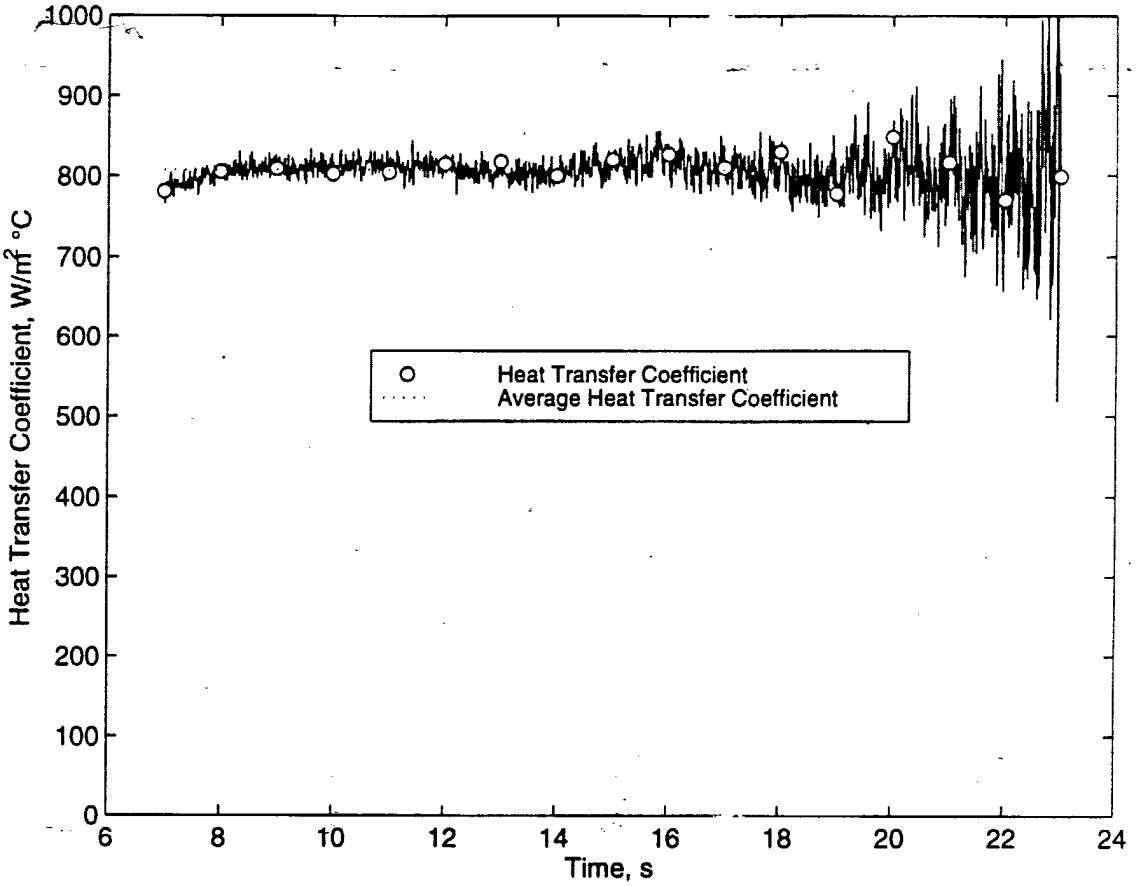

Figure 3.4: Time Varying Heat Transfer Coefficient at Gauge 1

fairly constant over the course of the run. The large amount of noise near 22 seconds is due to the way the heat transfer coefficient is calculated. Eqn. 3.8 shows that h can be calculated by dividing by q'', and as q'' approaches zero, the analysis breaks down. The least squares analysis has the advantage of not being affected by this "division by zero" phenomenon.

The time history of the film-cooling effectiveness can be found in a similar

manner. Assuming a constant h and using Eqn. 3.8 yields Fig. 3.5. This figure shows that the film-cooling effectiveness is constant over the course of a run.

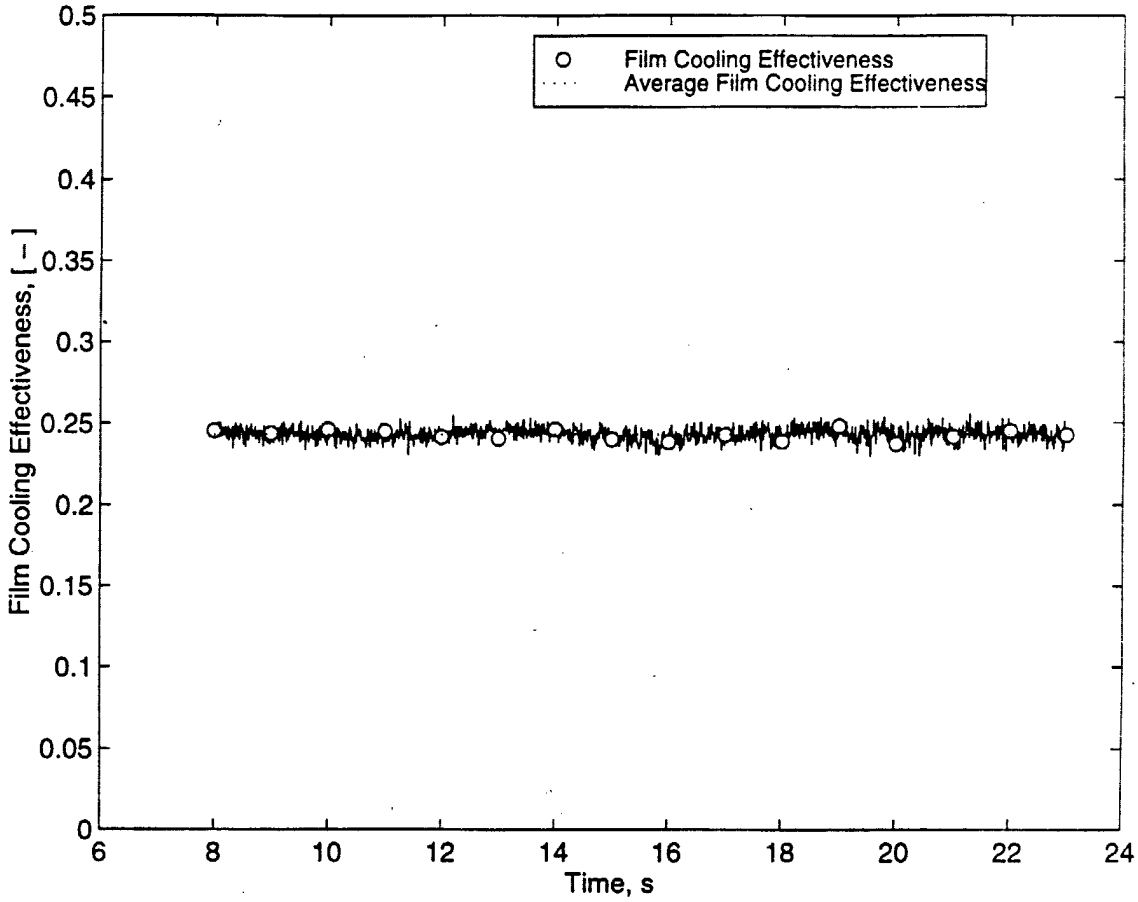

Figure 3.5: Time Varying Effectiveness at Gauge 1

3.3 Calculation of Coolant Ratios

A number of aerodynamic calculations have been made using isentropic relations. The first of these is the Mach number profile. The Mach number, Ma, at location x is calculated from,

$$Ma_x = \sqrt{\frac{2}{\gamma - 1} \cdot \left(\left(\frac{p_{t\infty}}{p_\infty} \right)^{\frac{\gamma-1}{\gamma}} - 1 \right)} \tag{3.10}$$

The coolant ratios defined in Eqn. 1.3 through Eqn. 1.5 are calculated using isentropic relations in the following manner.

$$DR \equiv \frac{\rho_c}{\rho_\infty}$$

$$DR = \frac{T_\infty}{T_c} \cdot \left(\frac{p_{tc}}{p_{t\infty}} \right)^{\frac{\gamma-1}{\gamma}} \tag{3.11}$$

$$I \equiv \frac{\rho_c U_c^2}{\rho_\infty U_\infty^2}$$

$$I = \frac{2}{\gamma - 1} \cdot \frac{1}{Ma^2} \cdot \left(\left(\frac{p_{tc}}{p_{t\infty}} \right)^{\frac{\gamma-1}{\gamma}} \cdot \left(1 + \frac{\gamma - 1}{2} \cdot Ma^2 \right) - 1 \right) \tag{3.12}$$

$$M \equiv \frac{\rho_c U_c}{\rho_\infty U_\infty}$$

$$M = \sqrt{DR \cdot I} \tag{3.13}$$

It can be seen from Eqn. 3.12 that I is a function of only the local freestream Mach number and the pressure ratio. Since the pressure ratio is controlled carefully with this experimental setup, the momentum ratio is consequently controlled. Since the pressure ratio is constant for all coolant exits and the momentum ratio is different for each coolant exit (as a consequence of the Mach number profile), the results of this

study show the film cooling effectiveness and heat transfer coefficient as affected by the pressure ratio. Fig. 3.6 illustrates Eqn. 3.12 over the ranges where this research is concerned.

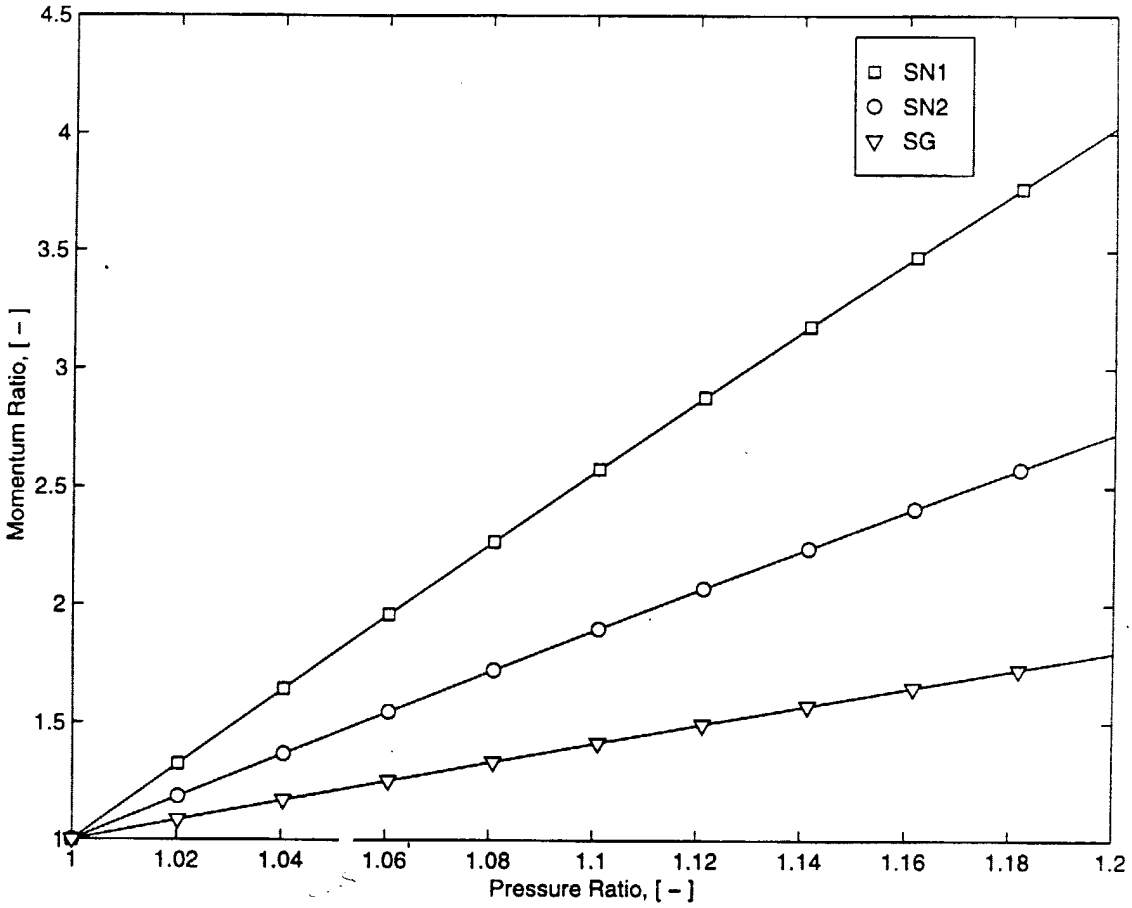

Figure 3.6: The Isentropic Relationship Between Pressure Ratio and Momentum Ratio

It is useful to look at the ratio histories over the duration of one representative run. The data shown in Fig. 3.7 through Fig. 3.9 are from the same sample run as shown in Fig. 3.1. These figures illustrate that the momentum ratio is held fairly constant over the course of the run. The density ratio, however, is shown to vary significantly due to the changing freestream and coolant temperatures and the fact that the density ratio changes with the temperature ratio as shown in Eqn. 3.11.

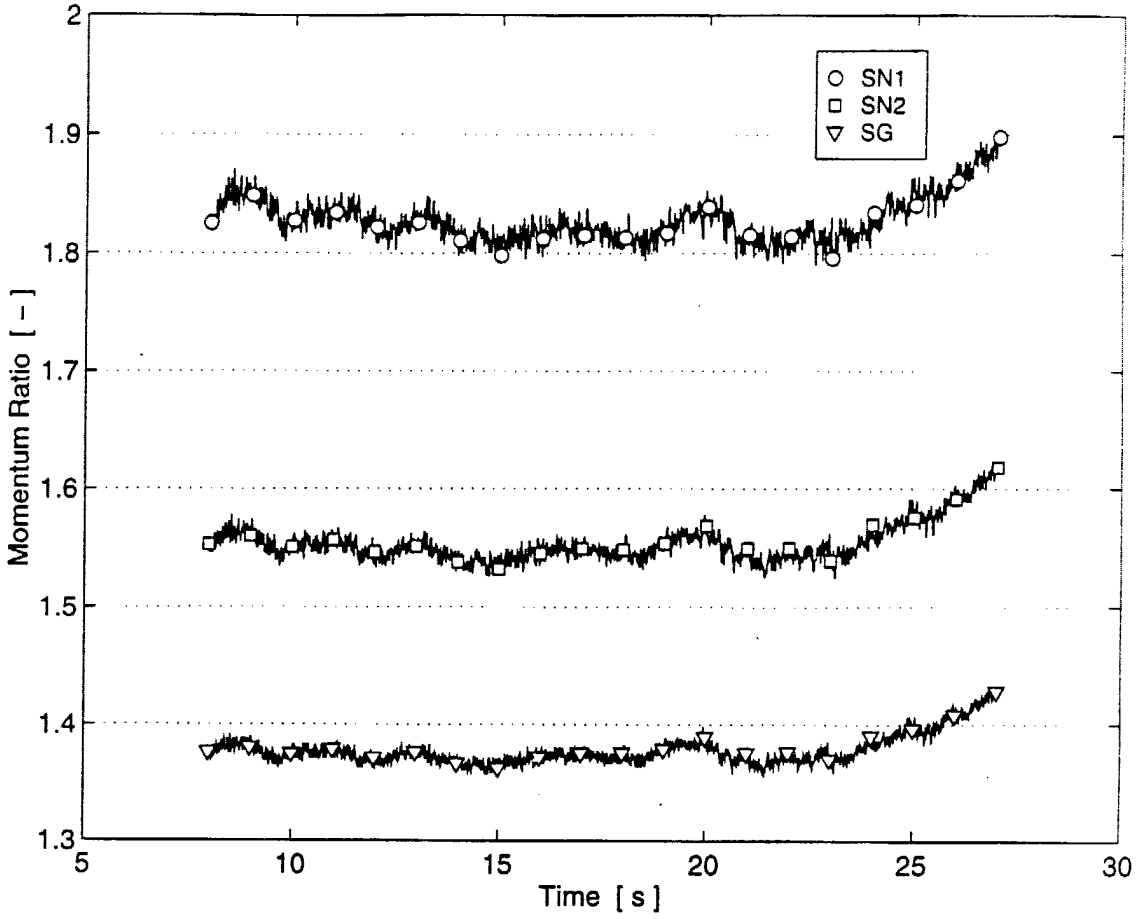

Figure 3.7: Time History of Momentum Ratio During Run

Also, the blowing ratio varies during the run due to the changing temperatures but only as the square root of the temperature ratio as illustrated by Eqn. 3.13.

The assumption that the density ratio has little effect on film cooling effectiveness over our range of interest is somewhat confirmed by these figures. Even though the density ratio is varying significantly, the data shown in Fig. 3.2 shows a very linear trend. This was an important verification of a needed assumption in the analysis.

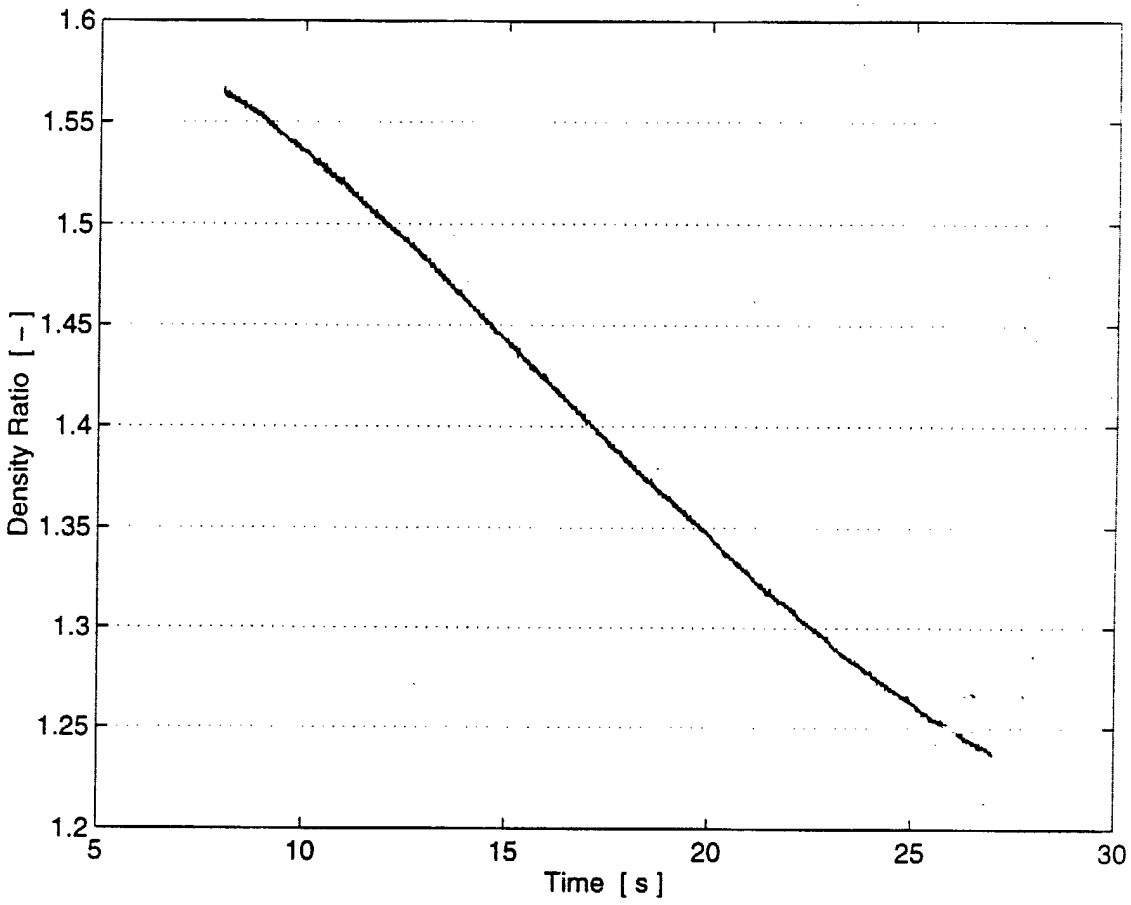

Figure 3.8: Time History of Density Ratio During Run

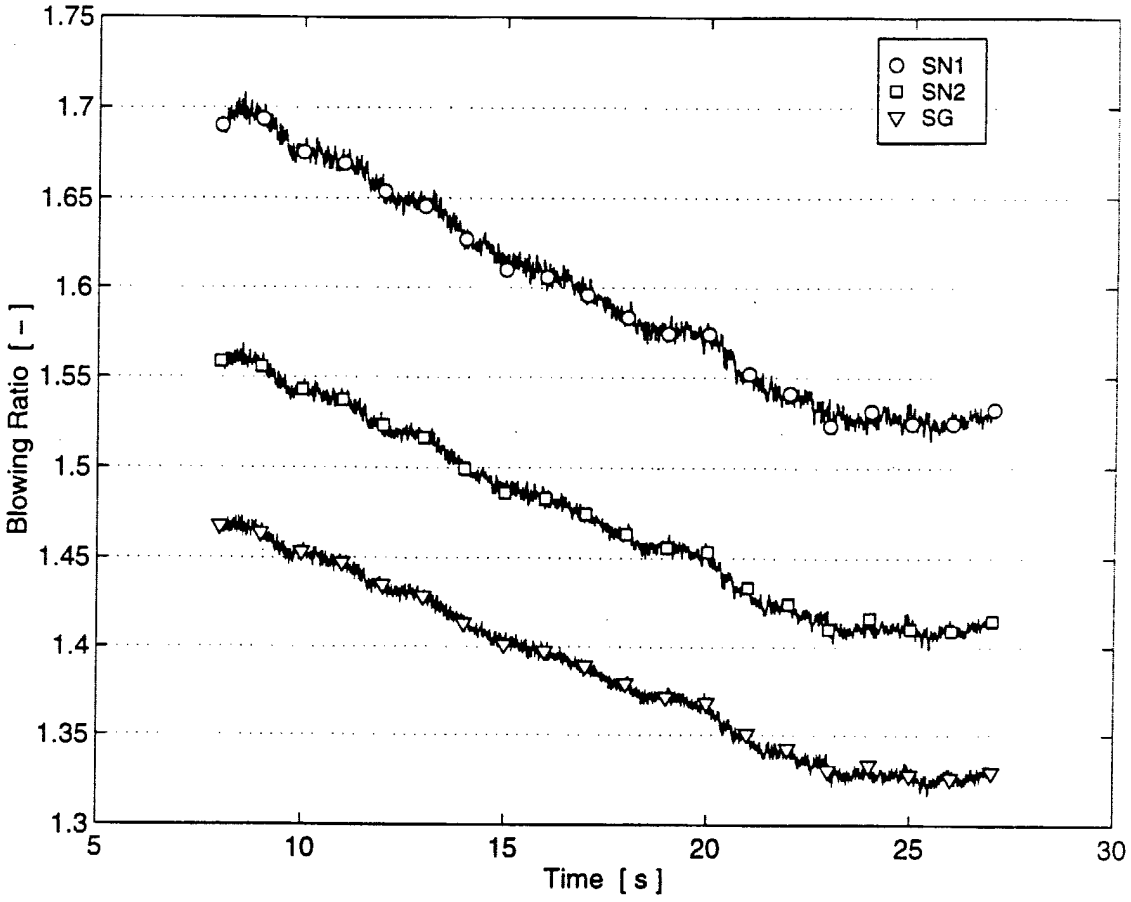

Figure 3.9: Time History of Blowing Ratio During Run

3.4 Measurement Error

There are two issues in measurement error that are important to consider: measurement uncertainty and measurement repeatability. Measurement uncertainty refers to how close the measurements are to the true physical properties. Measurement repeatability, on the other hand, is a measure of how repeatable the tests can be reproduced from run to run and day to day. The first of these matters to address is measurement uncertainty.

3.4.1 Measurement Uncertainty

Within measurement uncertainty there are two categories, bias uncertainty and precision. Bias uncertainty refers to an error that is made consistently from measurement to measurement. These types of errors are typically associated with calibration of the transducers or consistent errors in an acquisition scheme. The precision uncertainty is associated with random errors that vary from measurement to measurement. The first area of uncertainty to address is the bias uncertainty.

For these experiments, The HFM sensors are the main component of bias uncertainty. Reliable measurements of heat flux are directly dependent on the calibrated sensitivity of each sensor. The sensors went through an extensive calibration procedure summarized by Smith et al. [23]. In this study, the gauges were calibrated with both convective and radiative heat flux. At the conclusion of the study, values for the uncertainty for each of the gauge sensitivites are calculated. These uncertainties are specific for each of the gauges installed in the blade, and they are based on several of the convective tests and a 90% confidence interval assuming a student-T distribution. These uncertainties are listed in Table 3.1. The next question to answer is how do these bias errors in heat flux measurements affect the h and η biases. Since the

Table 3.1: HFM Gauge Uncertainties

Gauge	Uncertainty
1	17.0%
2	3.7%
3	5.2%
4	15.2%
5	8.8%
6	10.7%

value of h is the slope of the linearized data and q'' is plotted on the y-axis. these q'' uncertainties go directly into the h values, so that the values in Table 3.1 can be understood directly as bias uncertainties in h. Also, the uncertainty of η is unaffected by uncertainties in the scale of q'' since η is derived from the x-axis intercept of the linearized data. The value of η is solely dependent upon temperature measurements and is unbiased using this data reduction method.

The next area of uncertainty is precision. The thermocouple measurements constitute this type of uncertainty. The kinds of errors that go into precision uncertainty are thermocouple wire difference from junction to junction, acquisition inconsistencies from channel to channel, or a wandering electronic ice point. The three thermocouple measurements that go into the h and η calculations are T_w, T_c, and T_r. Temperature measurements are made with K-Type thermocouples and the AMUX-64T multiplexer board. From the *National Instruments* literature the uncertainty of any individual temperature measurement is estimated to be $\pm$ 1.1°C. The value used for T_r is 1.56°C since it is a derived value from two thermocouple measurements (square root of the sum of the squares).

In order to translate the individual thermocouple precision uncertainties to h and η precision uncertainties, a method was used similar to that suggested by Moffat [18]. The first step of this approach is re-apply the h and η analysis using the nominal values of two of the temperature measurements and an "errored" third temperature measurement consisting of the measurement added to its uncertainty.

The addition or subtraction of this individual uncertainty is done such that it has the greatest influence on the h and η values. Next, this procedure is repeated for each of the other two measurements individually, and the influence of each measurement is computed. Knowing each individual contribution, the total uncertainty, δ, can be calculated as the sum of the squares of all three uncertainties,

$$\delta = \sqrt{\delta_{T_r}^2 + \delta_{\dot{m}_w}^2 + \delta_{T_c}^2} \tag{3.14}$$

The results vary slightly from gauge to gauge and from run to run. A number of runs over different operating ranges were subjected to this uncertainty analysis and the maximum uncertainty for each gauge is listed in Table 3.2. The raw data for the runs is listed in Appendix C in the MATLAB file "summary.m".

Table 3.2: Precision Uncertainties

Gauge	h Precision	η Precision
	[W / m^2 °C], [%]	[-], [%]
1	43.5, 5.9%	0.040, 18.5%
2	49.2, 6.1%	0.041, 21.0%
3	35.0, 5.6%	0.036, 13.9%
4	42.5, 5.9%	0.040, 21.3%
5	48.3, 6.0%	0.040, 17.0%
6	49.4, 5.7%	0.034, 11.5%

3.4.2 Measurement Repeatability

Another indication of measurement error is measurement repeatability. This refers to the repeatability of conditions from run to run. Measurement repeatability is an experimental number that reflects the same ideas contained in the more theoretical value of precision (from Sec. 3.4). Measurement repeatability, however, also takes into account the real variations from run to run (e.g. variation of aerodynamic conditions, variations of humidity levels, coolant supply leakage, etc.). These kinds of errors have not been accounted for in the data reduction scheme, and perhaps some of the sources of variation probably have not been even conceived. Because of this, it is important to get this experimental value of measurement repeatability.

In order to quantify the measurement repeatability, a number of runs at approximately the same conditions were compared. The greatest number of runs were performed near the cooling design point of a pressure ratio of 1.04. All of the runs for this pressure ratio are compared in Fig. 3.10 and 3.11.

These measurements were taken from eight different runs on two different days. There was considerable variation noticed from day to day. The different day's runs are shown with different symbols. With these runs, a Student-T distribution with a 90% confidence interval is used. These confidence intervals are shown in Table 3.3.

Table 3.3: Measurement Repeatability

Gauge	h 90% Confidence Interval	η 90% Confidence Interval
	[W / m^2 °C], [%]	[-], [%]
1	± 90, ± 11.1%	± 0.049, ± 16.4%
2	± 32, ± 4.0%	± 0.015 ± 8.2%
3	± 34, ± 5.5%	± 0.024, ± 7.1%
4	± 38, ± 5.1%	± 0.034, ± 15.8%
5	± 51, ± 6.7%	± 0.023, ± 12.1%
6	± 63, ± 7.3%	± 0.034, ± 11.4%

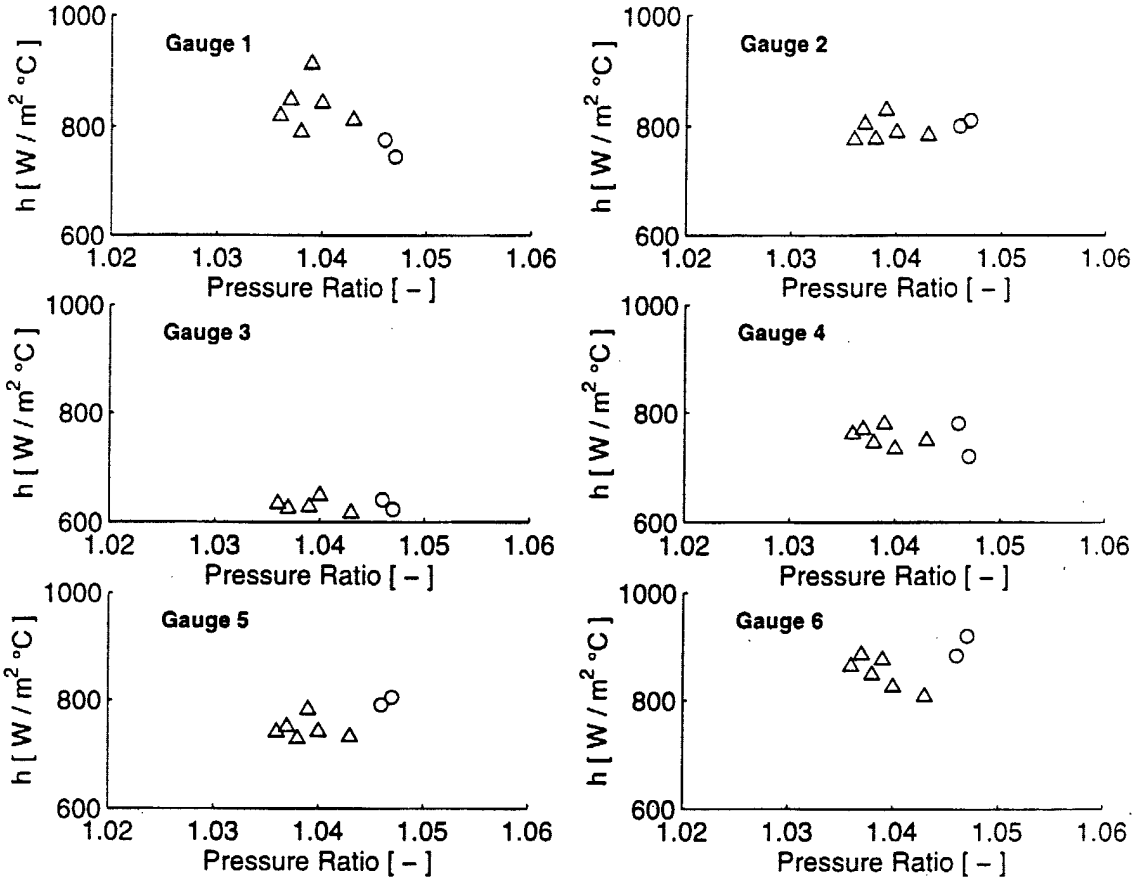

Figure 3.10: Measurement Repeatability of Heat Transfer Coefficient at PR=1.04

The observed measurement repeatability is of approximately the same size as the theoretical precision uncertainty. Gauge 1 is an exception to this generalization as its observed repeatability is higher than its predicted precision. Most likely this is due to the fact that the flow physics around gauge one is extremely unstable because it is so close to the last coolant exit.

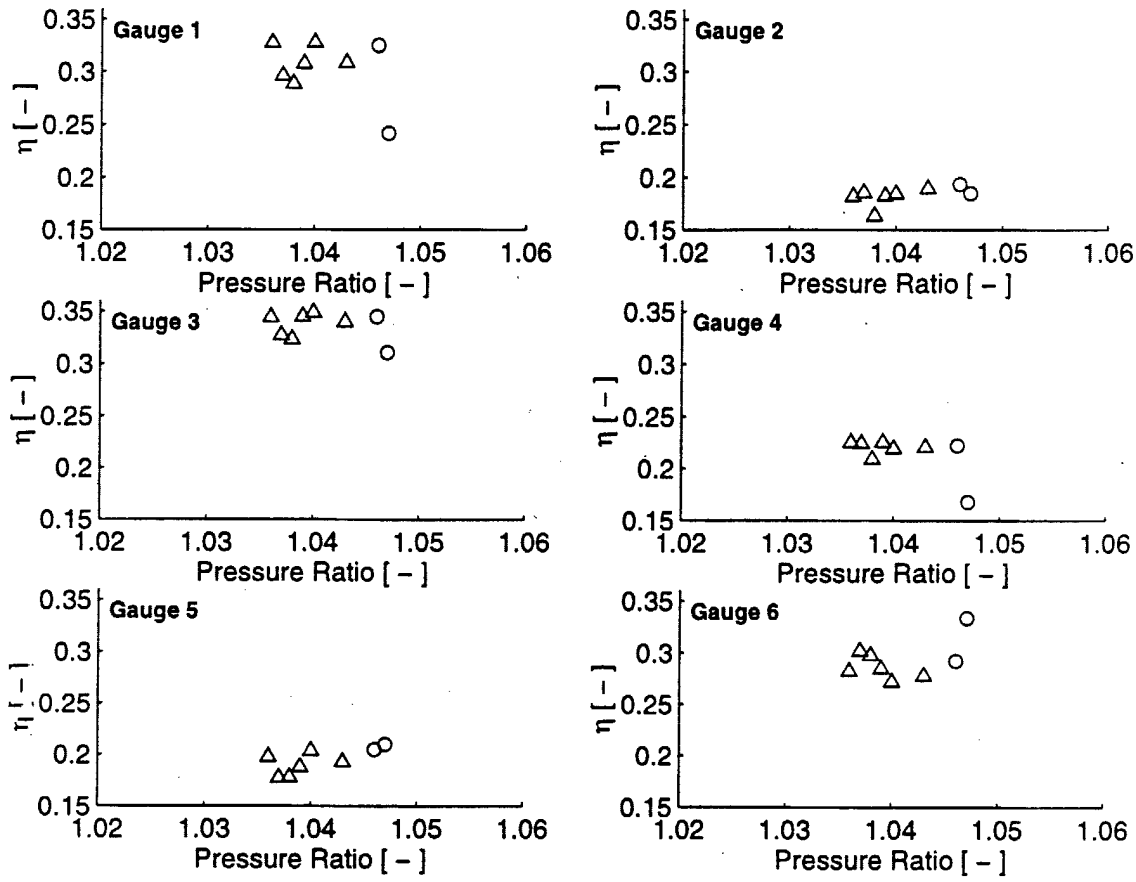

Figure 3.11: Measurement Repeatability of Effectiveness at PR=1.04

3.5 Coolant Mass Flow

The coolant mass flow rates measured using the orifice plate are documented in Fig. 3.12. On the left axis of this figure is the mass flow (g/s) and on the right axis is the fraction of coolant mass flow to the approximate freestream mass flow per passage (2 kg/s). Also shown on this curve is the predicted mass flow from an isentropic calculation and a discharge coefficient of 0.655. As can been seen, the mass flow of coolant is increased at higher pressure ratios. The scatter of this data is

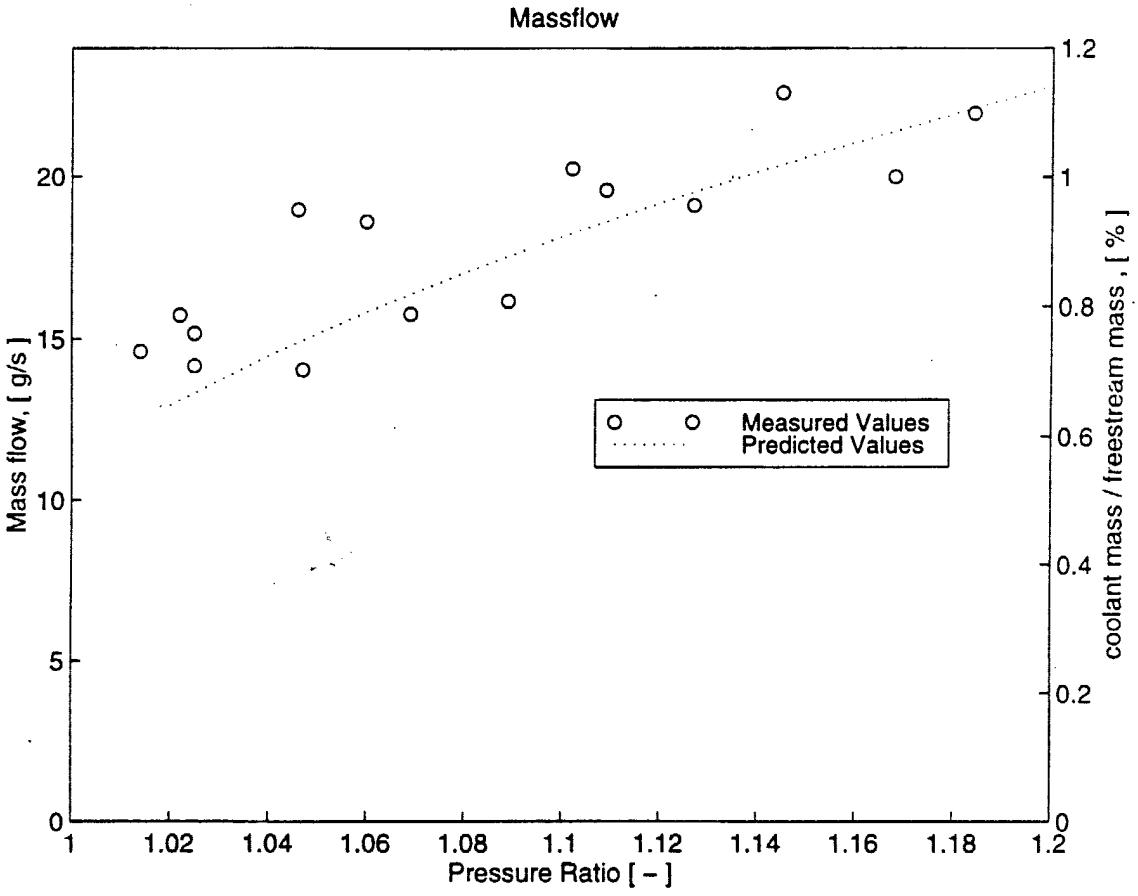

Figure 3.12: Coolant Mass Flow as a Function of Pressure Ratio

most likely due to the lack of control of coolant temperature (and therefore density ratio). In order to evaluate this possibility, it is useful to examine an expression for

the coolant mass flow,

$$\dot{m} = \rho_c \cdot U_c \cdot A$$
$$\dot{m} = M \cdot \rho_\infty \cdot U_\infty \cdot A$$
$$\dot{m} = \sqrt{I \cdot DR} \cdot \rho_\infty \cdot U_\infty \cdot A \tag{3.15}$$

Eqn. 3.15 shows that the mass flow is proportional to the square root of the product of the momentum ratio and density ratio, $\sqrt{I \cdot DR}$. Arbitrarily choosing the Suction Gill exit momentum ratio and plotting $\sqrt{I \cdot DR}$ on top of the measured mass flow is done in Fig. 3.13. This figure suggests a nice correlation between the scatter in the mass flow and the scatter in the density ratio.

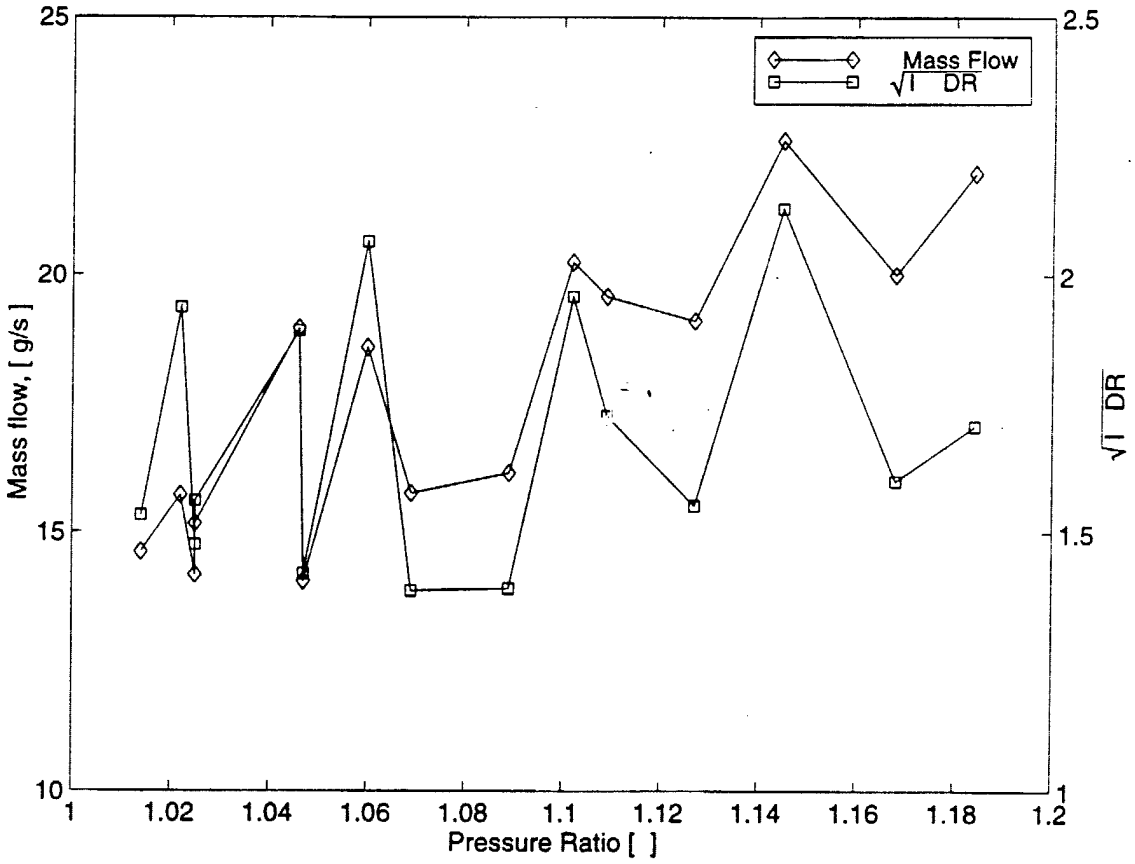

Figure 3.13: Coolant Mass Flow compared to $\sqrt{I \cdot DR}$ for SG

Again, it should be pointed out that the changes in density ratio have been shown earlier to not affect the heat transfer coefficient and film cooling effectiveness significantly (See Section 3.3).

Chapter 4

Results and Discussion

4.1 Shadowgraph Visualization

Shadowgraph photographs of tests with different pressure ratios are shown in Fig. 4.1 through Fig. 4.7. Unfortunately, the quality of these photographs is limited due to the following reasons:

- The abrasive environment of the tunnel gave poor endwall surface quality and lead to Moire patterns.
- Frost was formed near the leading edge on the outside of the endwalls due to the cold coolant.
- The optical set-up distorted the blade shape so the locations of the gauges and coolant geometry shown in Fig 4.1 are all approximate.
- The camera has a reduced resolution compared to that of Polaroid film.

Fig. 4.1 shows a drawing of the blade overlaid on the shadowgraph. This figure orients the photograph with respect to the coolant geometry. Fig. 4.2 shows the blade with no freestream flow and no coolant flow running. This figure can be used as a reference to compare the features of the coolant pictures. Another no-freesream flow picture is shown in Fig. 4.3. In this picture the coolant flow is running at a pressure ratio of 1.04. It can be seen in this picture that, without the presence of a freestream flow, the coolant film shoots directly off the blade surface. This is no surprise but the picture serves as a check that the coolant film can be visualized.

The next figures (4.4 - 4.7) show cases with the main flow and a progression of coolant pressure ratio. The film layer can be seen on these pictures attached to the blade surface. The most striking observance between these photos is that there is no noticeable difference between the appearance of the coolant layers. Never does the coolant seem to lift off the surface, as we had previously anticipated happening. Furthermore, while there appears to be a slight thickening of the film layer from the 1.02 to the 1.04 tests, there is no significant changes from the 1.04 to either of the higher pressure ratios photographs. This observation was surprising.

It is important to realize that these photographs only give a spanwise averaged picture across the flow field as is an inherent feature of al . There might perhaps be some spanwise shifting of the coolant flow or other coolant physics that is not being shown using this visualization method.

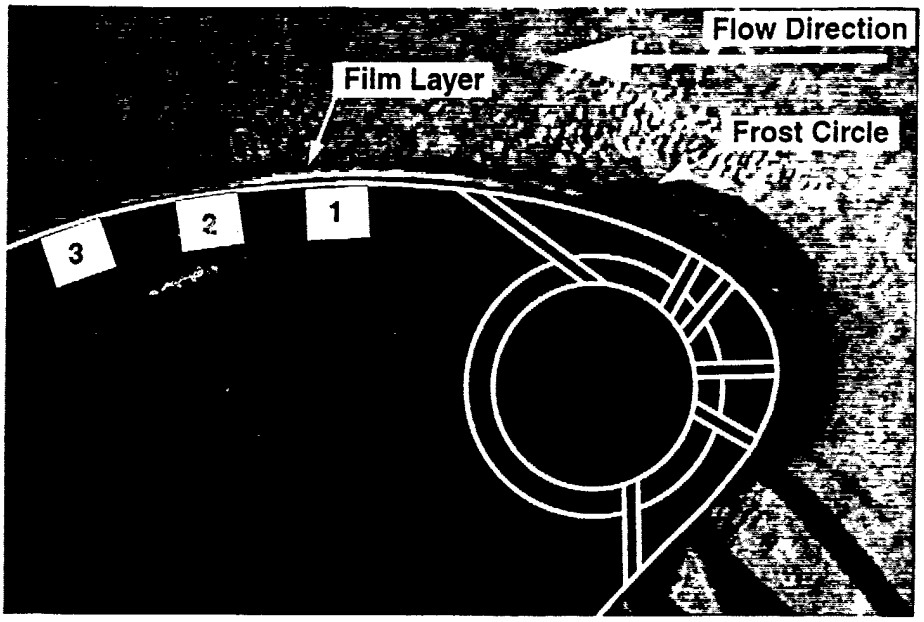

Figure 4.1: Typical Shadowgraph

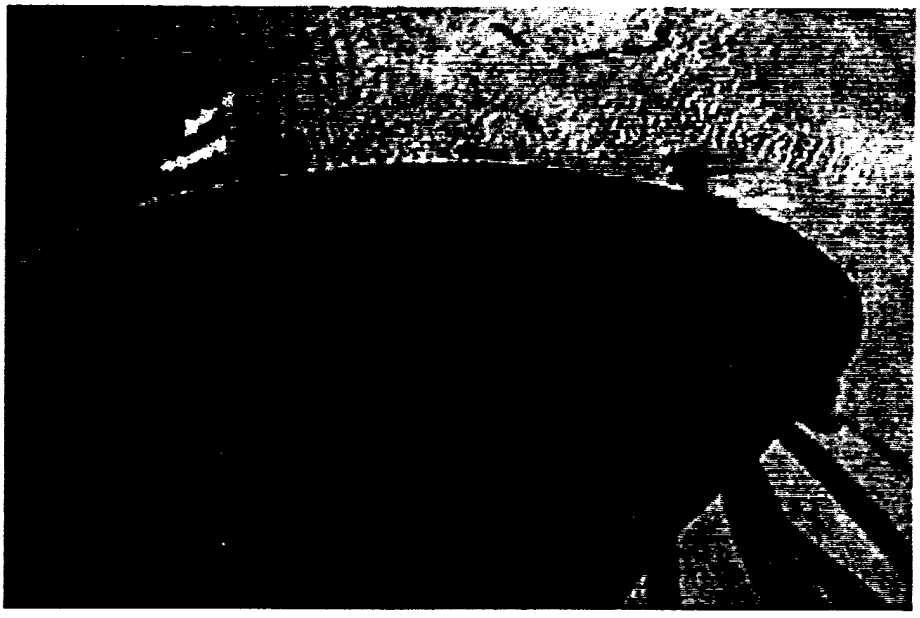

Figure 4.2: Shadowgraph, No Flow, No Coolant

Figure 4.3: Shadowgraph, No Flow, Coolant Running

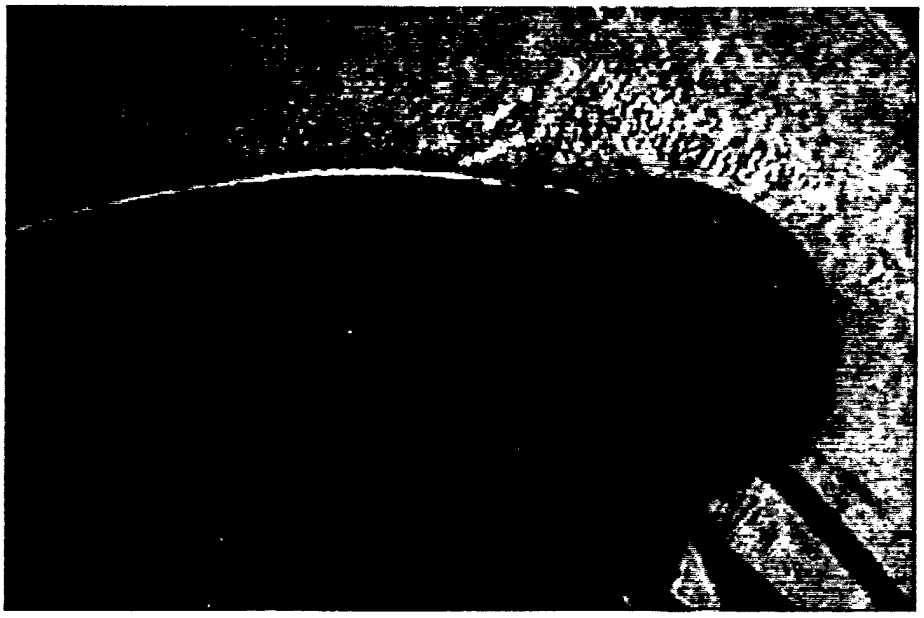

Figure 4.4: Shadowgraph, Pressure Ratio: 1.02

Figure 4.5: Shadowgraph, Pressure Ratio: 1.04

Figure 4.6: Shadowgraph, Pressure Ratio: 1.18

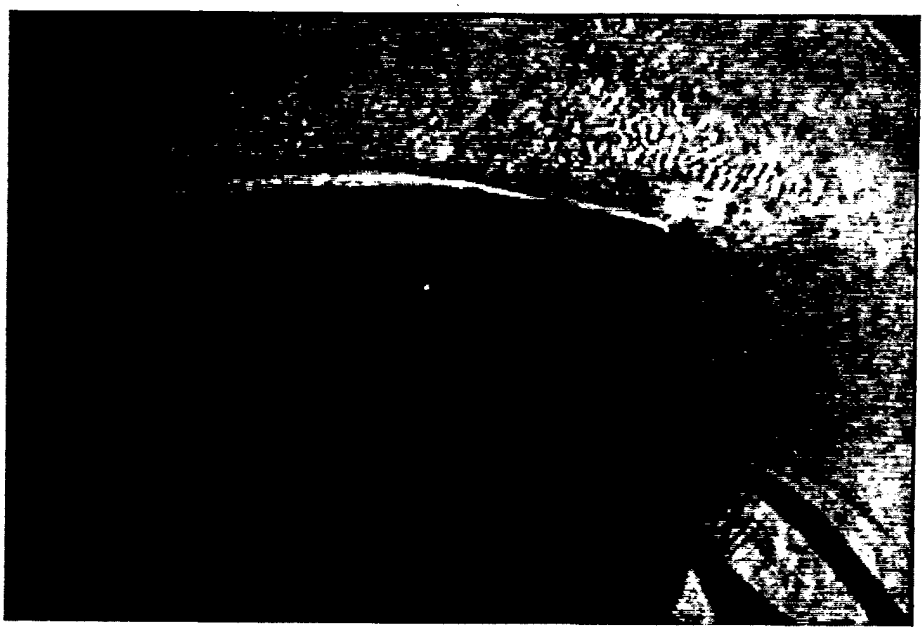

Figure 4.7: Shadowgraph, Pressure Ratio: 1.21

4.2 Effect of Pressure Ratio on Heat Transfer Coefficient

The observed effect of the pressure ratio on the surface heat transfer coefficient is illustrated in Fig. 4.8 through Fig. 4.13. These graphs show the results from a number of runs performed on two different days. The range of pressure ratios covers from about 1.02 to about 1.19. The GE design point for this coolant design is a pressure ratio of 1.04. The error bars shown on these plots are for the 90% confidence bounds on measurement repeatability (these uncertainties are summarized in Table 3.1). It is important to realize that the error bars are representative of measurement repeatability and not measurement accuracy as discussed in Sec. 3.4. Each of the gauges is shown on a different graph to better illustrate the trends of pressure ratio at each different location.

A few observations can be made from looking at these graphs. One noticeable feature is that the data at Gauge 1 has very low repeatability as evidenced by the scatter of the data points and the large error bars. It is suspected that this scatter is due to the fact that Gauge 1 is so close to the last coolant exit. At this close location, the film is most probably very un-mixed and small tunnel variations can create significant changes in the local flow field appearance. This type of situation would result in a very unstable flow physics at this location. The second more general observation, is that the heat transfer coefficient appears to be fairly independent of the pressure ratio.

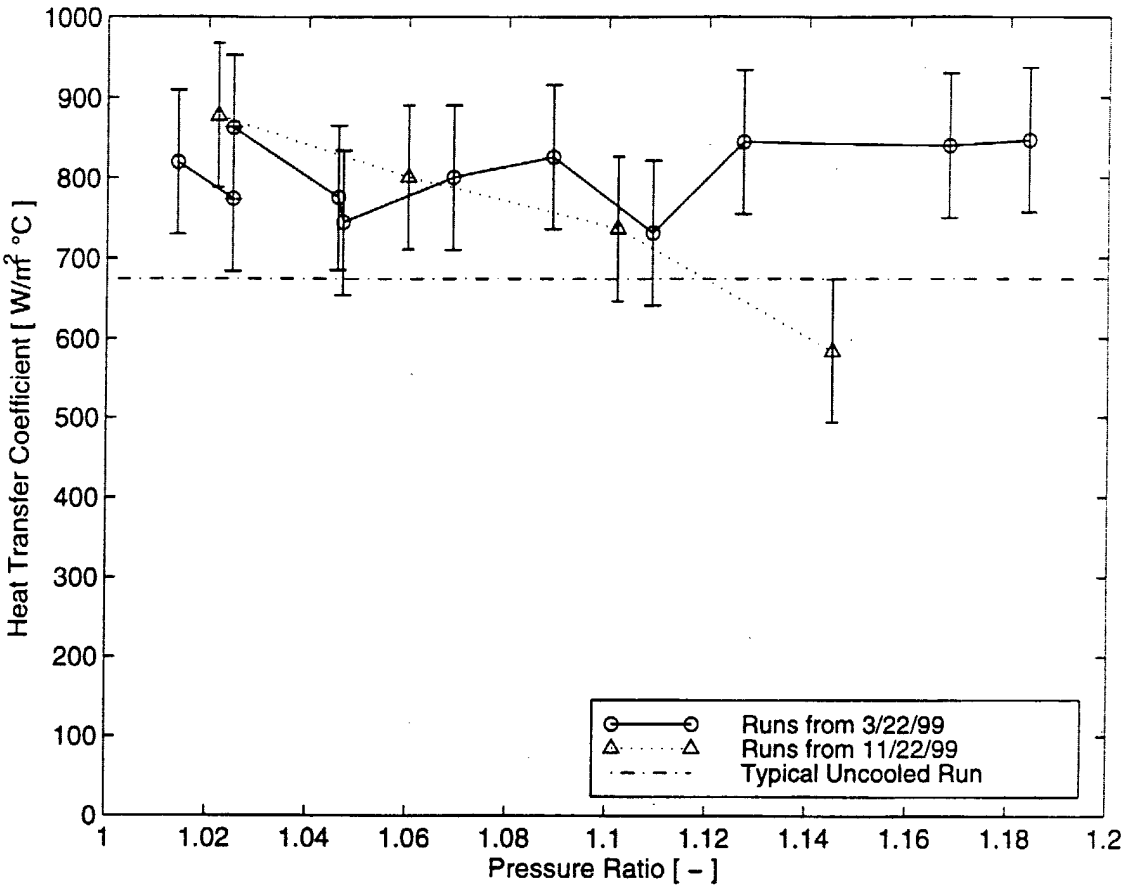

Figure 4.8: Variation of Heat Transfer Coefficient with Pressure Ratio for Gauge 1

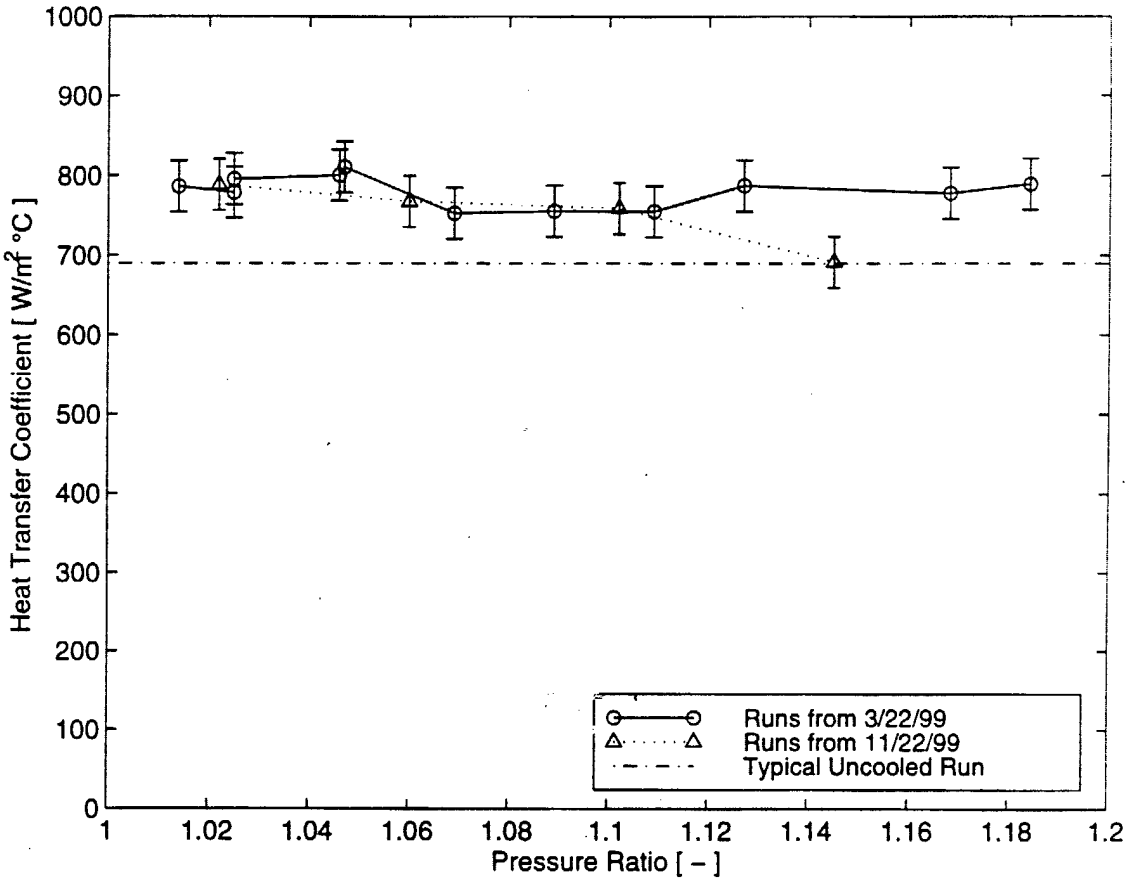

Figure 4.9: Variation of Heat Transfer Coefficient with Pressure Ratio for Gauge 2

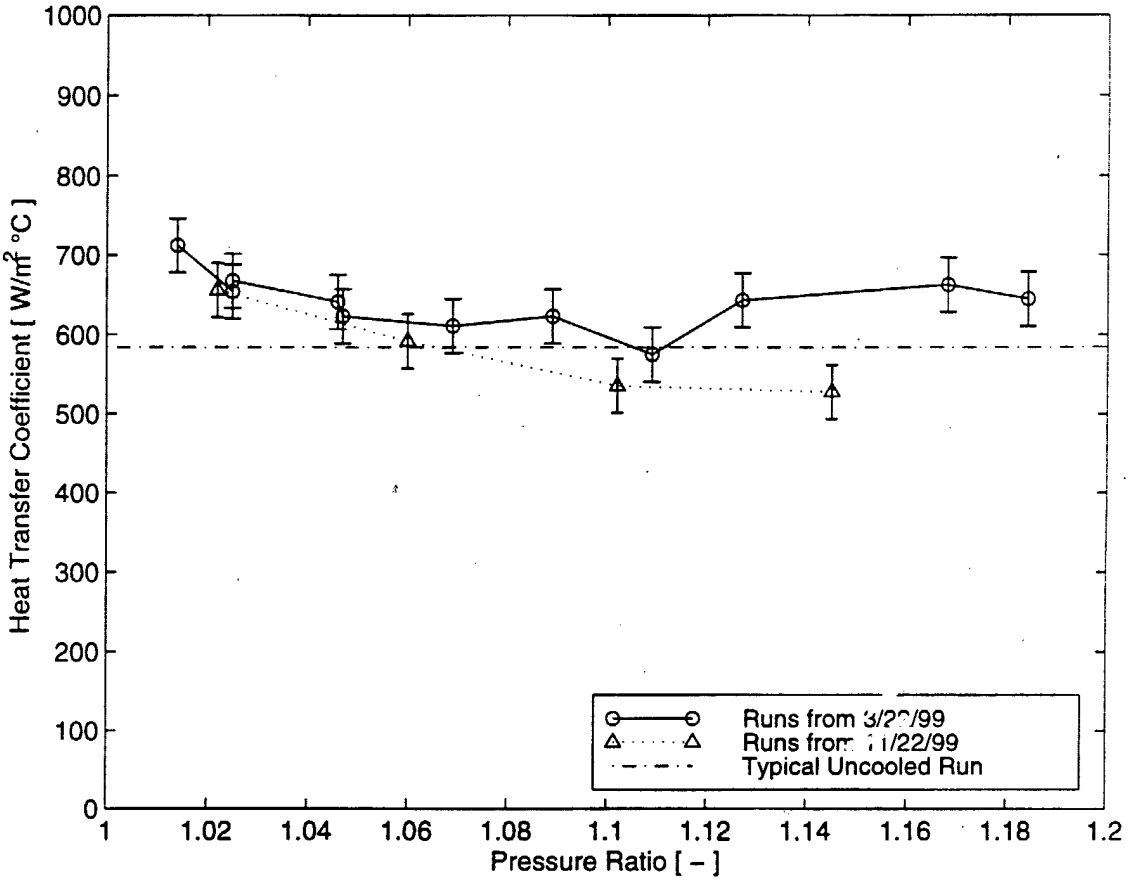

Figure 4.10: Variation of Heat Transfer Coefficient with Pressure Ratio for Gauge 3

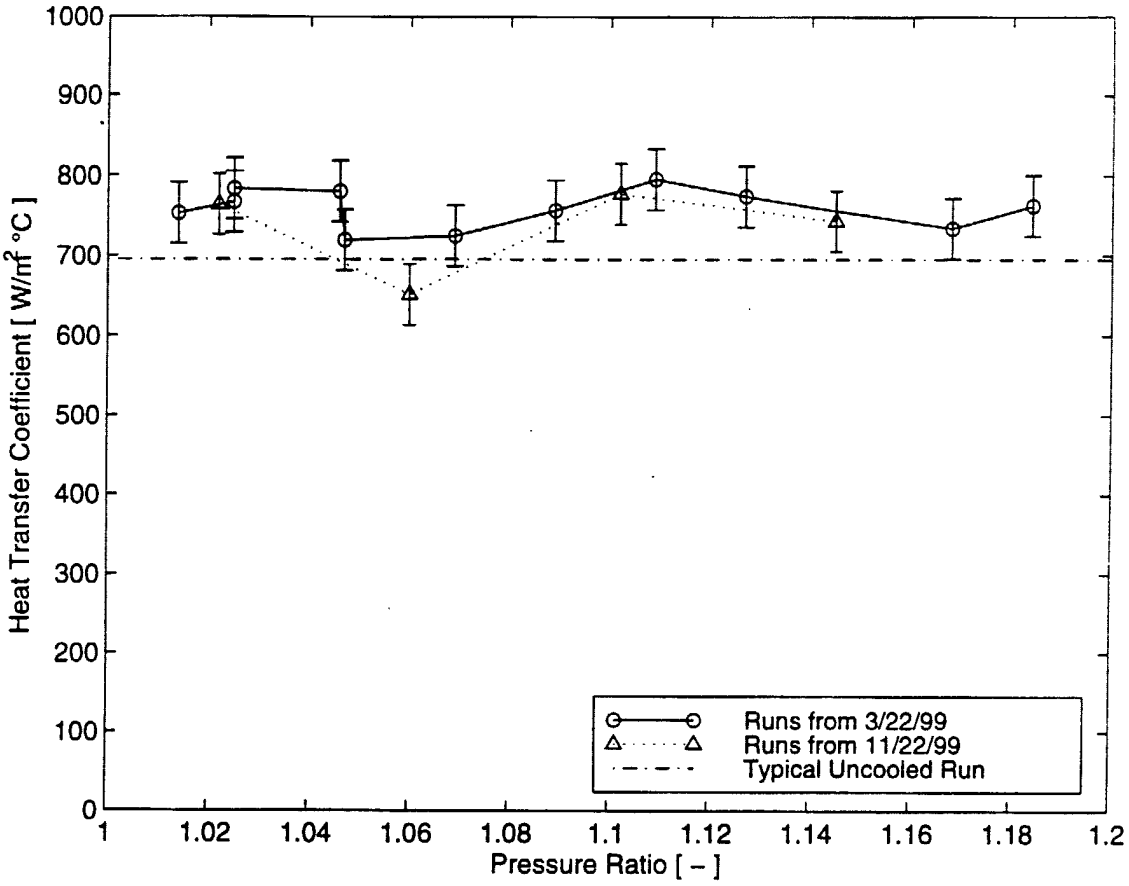

Figure 4.11: Variation of Heat Transfer Coefficient with Pressure Ratio for Gauge 4

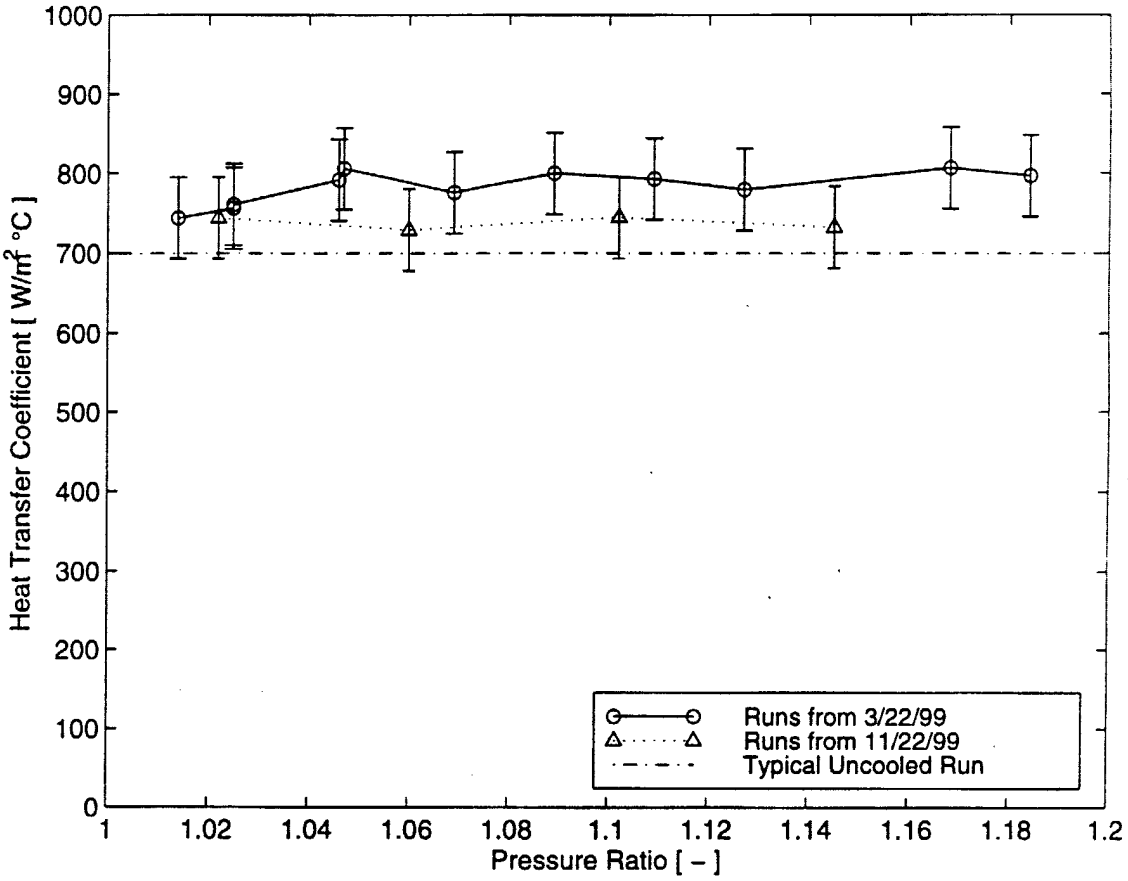

Figure 4.12: Variation of Heat Transfer Coefficient with Pressure Ratio for Gauge 5

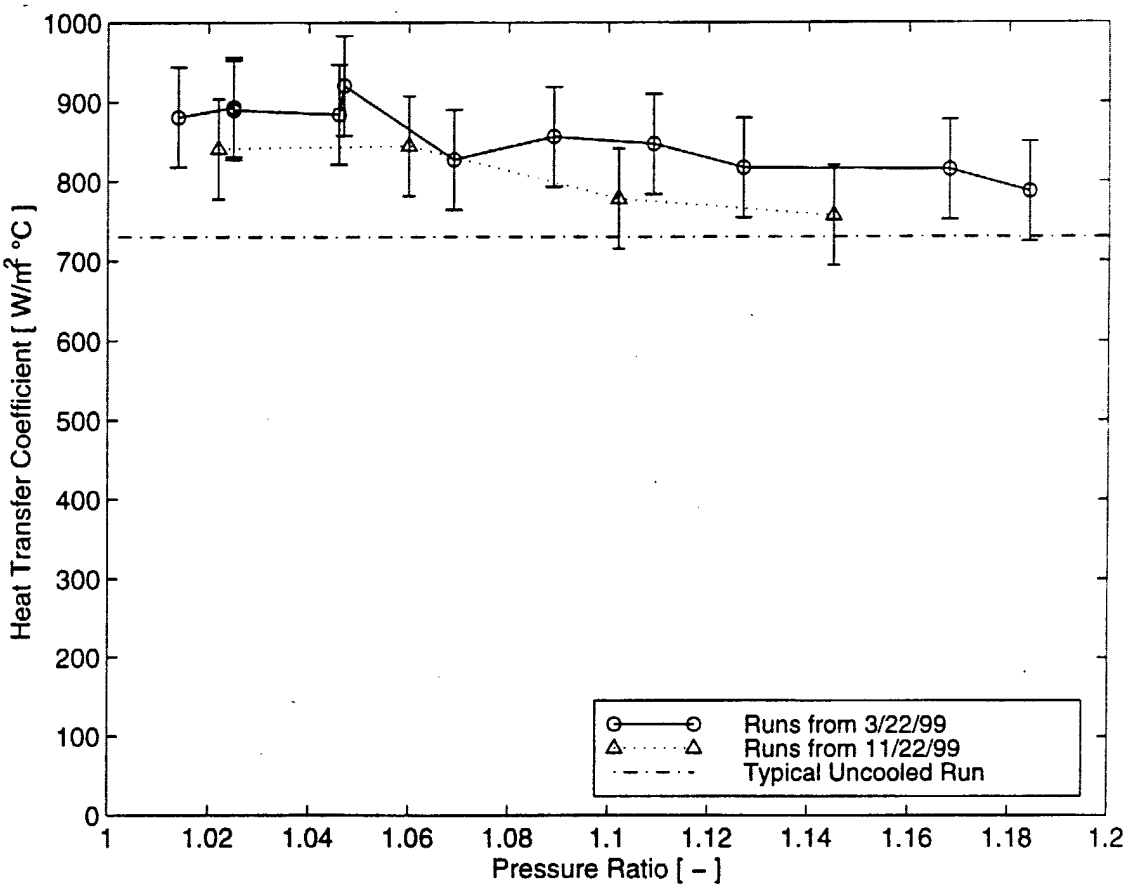

Figure 4.13: Variation of Heat Transfer Coefficient with Pressure Ratio for Gauge 6

4.3 Effect of Pressure Ratio on Effectiveness

The observed effect of the pressure ratio on film cooling effectiveness is illustrated in Fig. 4.14 through Fig. 4.19. These graphs show the results from a number of runs performed on two different days. The range of pressure ratios covers from about 1.02 to about 1.19. The GE design point for this coolant design is a pressure ratio of 1.04. The error bars shown on these plots are for the 90% confidence bounds on measurement repeatability (these uncertainties are summarized in Table 3.1). It is important to realize that the error bars are representative of measurement repeatability and not measurement accuracy as discussed in Sec. 3.4. Each of the gauges is shown on a different graph to better illustrate the trends of pressure ratio at each different location.

At Gauge 1, a high scatter of the data points is observed. It is suspected that this scatter is due to the same reason there is high scatter in the heat transfer coefficient. This reason is that the flow physics in the region so close to the coolant exits is unsteady. The film is not mixed very well and from one run to the next different amounts of film coverage are present resulting in different cooling effectiveness. The uncertainties and overall scatter of the data points outweigh any trends that might be interpreted.

Gauge 2 has much lower scatter and a fairly flat trend of film cooling effectiveness. Gauge 3 has moderate uncertainty and a trend that suggests the film cooling effectiveness is reduced at the higher pressure ratios. Gauge 4 shows little dependence of effectiveness on pressure ratio.

Gauges 5 and 6 show a trend that indicates film cooling effectiveness reduces slightly with higher pressure ratios.

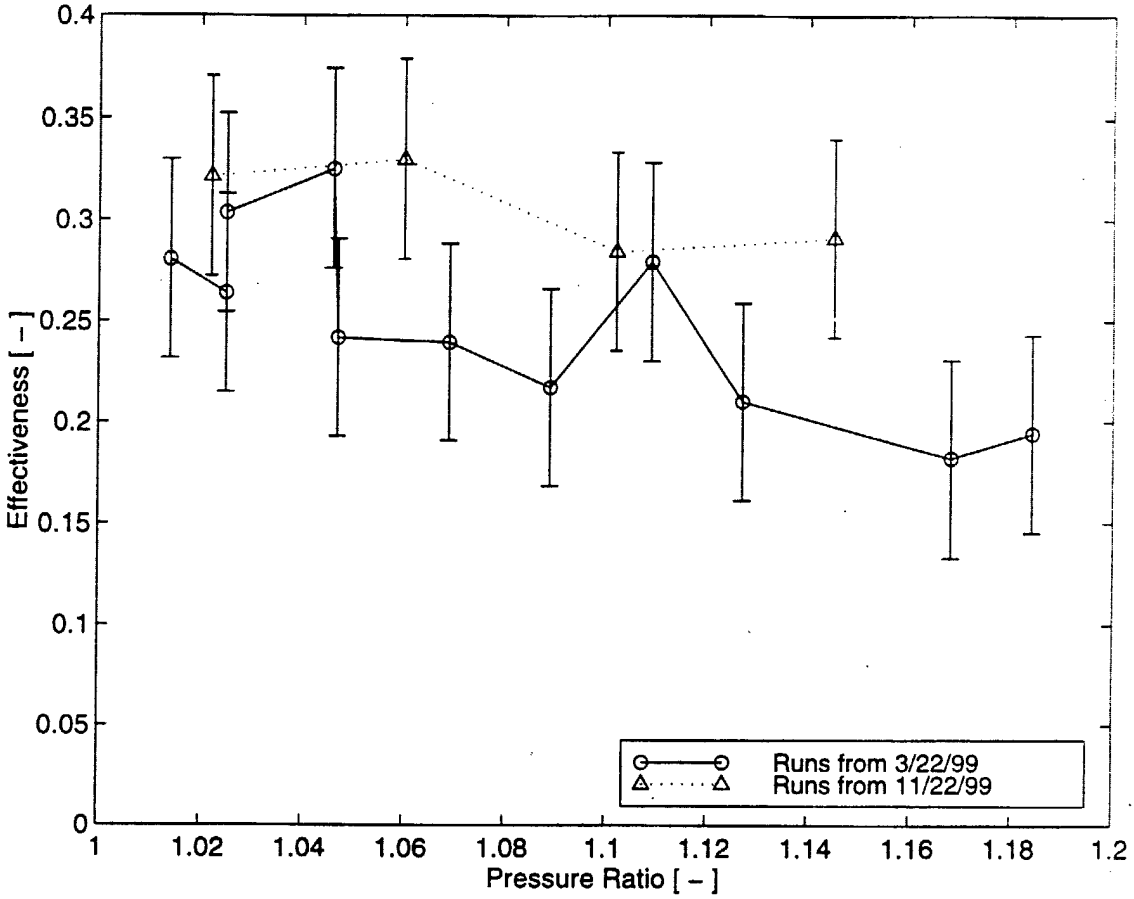

Figure 4.14: Variation of Film Cooling Effectiveness with Pressure Ratio for Gauge 1

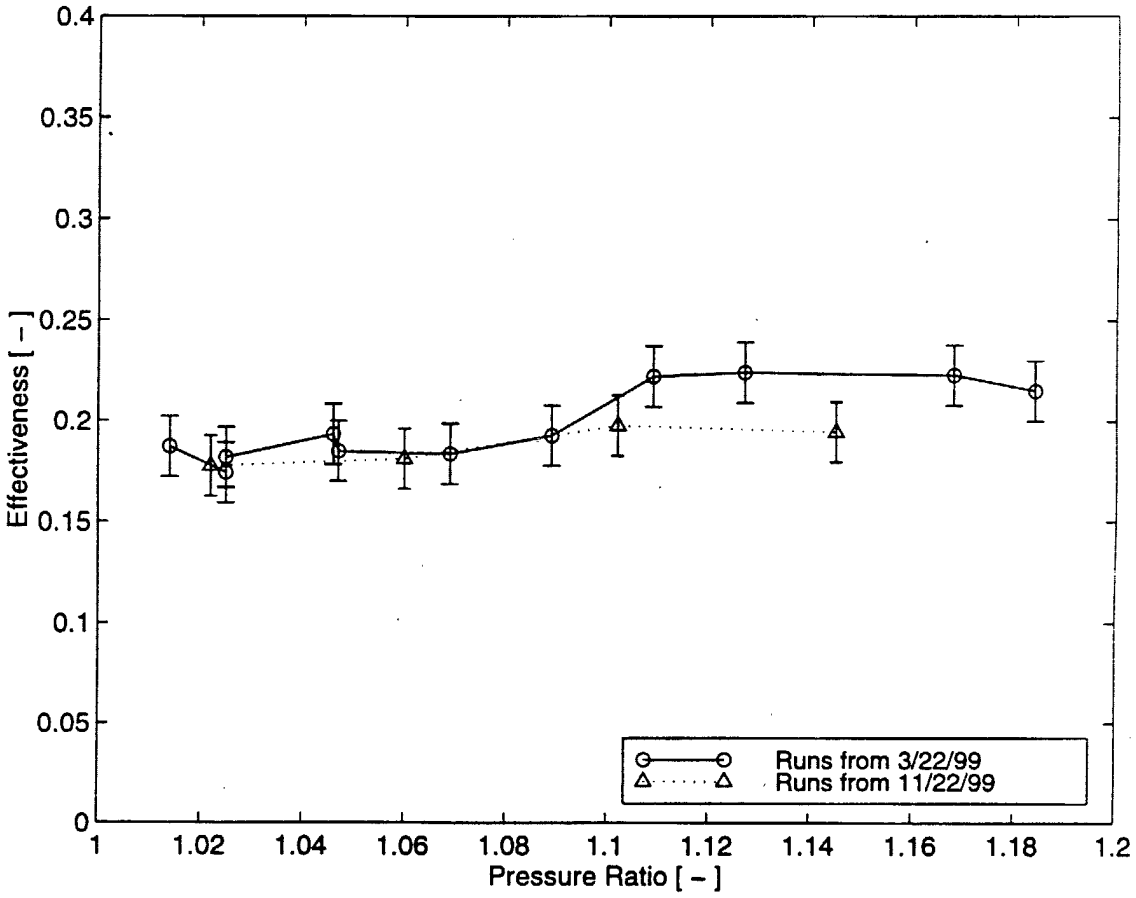

Figure 4.15: Variation of Film Cooling Effectiveness with Pressure Ratio for Gauge 2

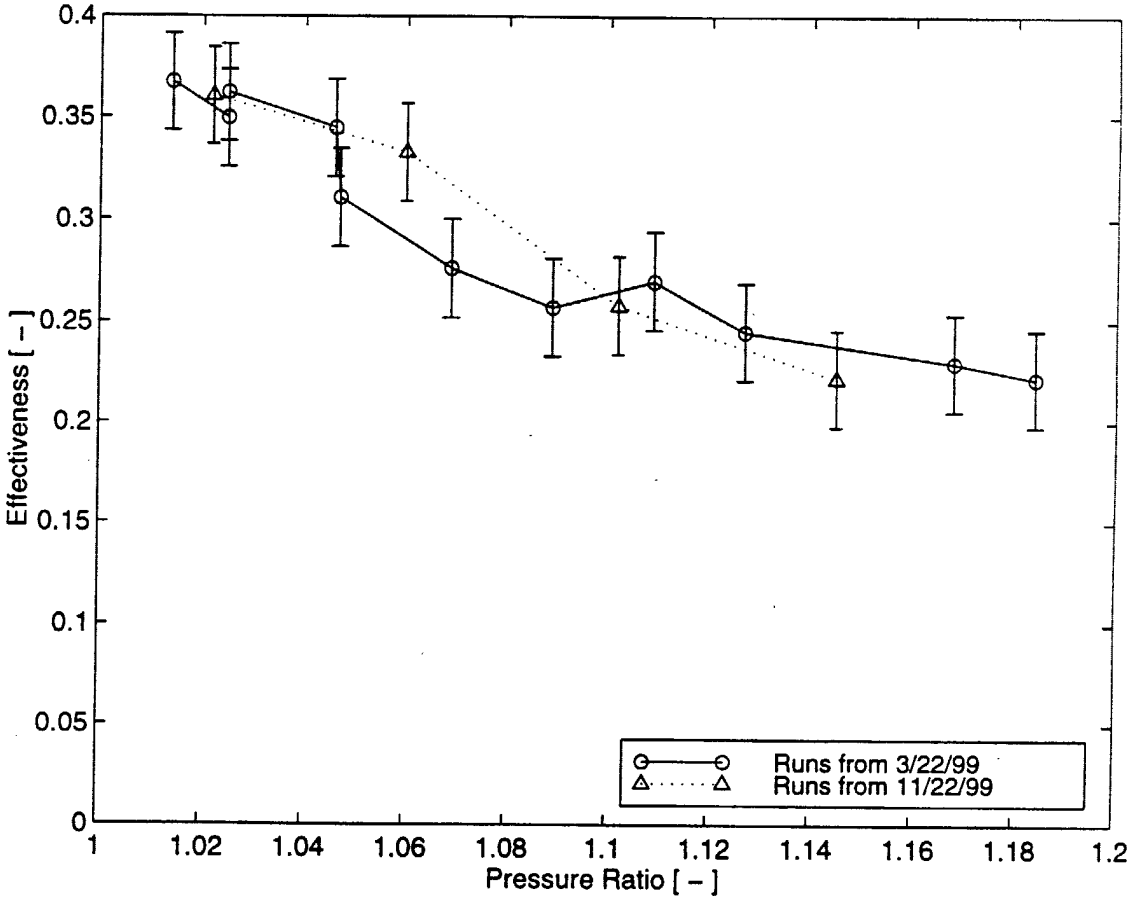

Figure 4.16: Variation of Film Cooling Effectiveness with Pressure Ratio for Gauge 3

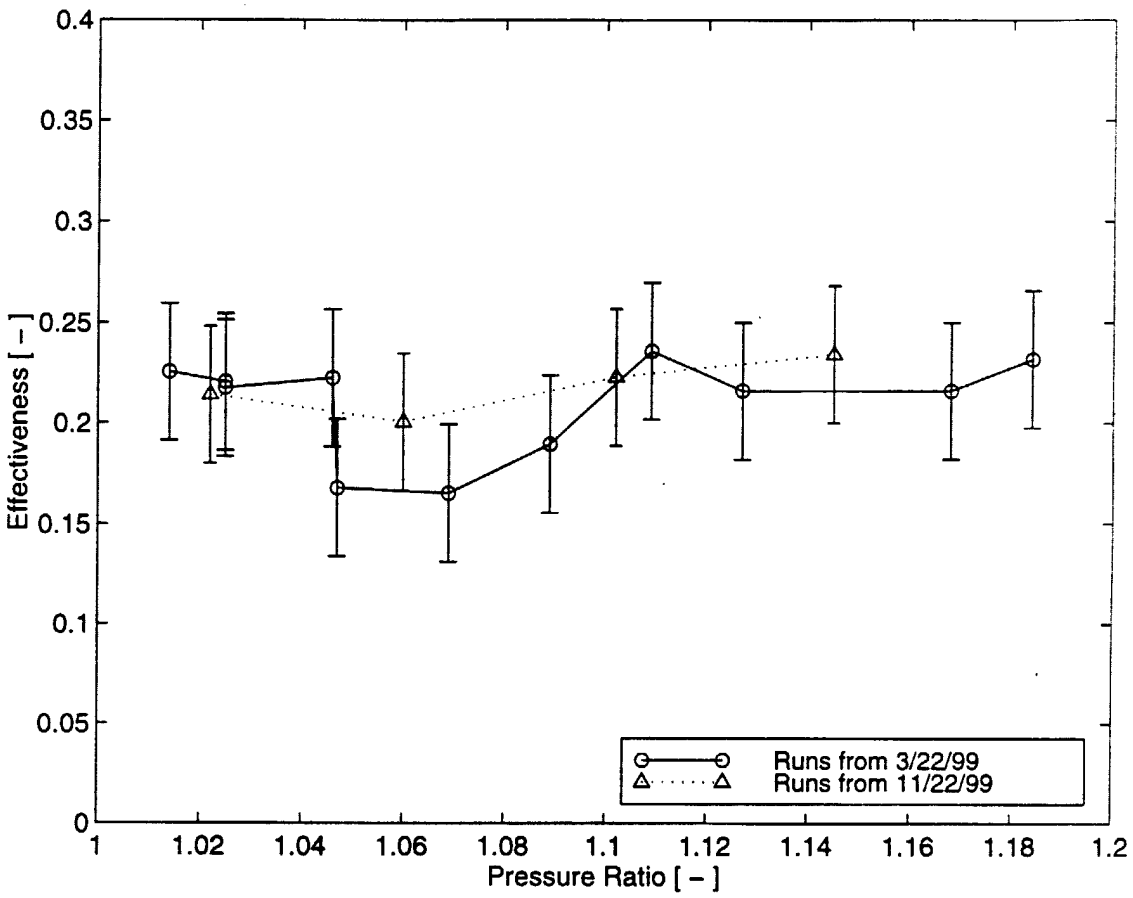

Figure 4.17: Variation of Film Cooling Effectiveness with Pressure Ratio for Gauge 4

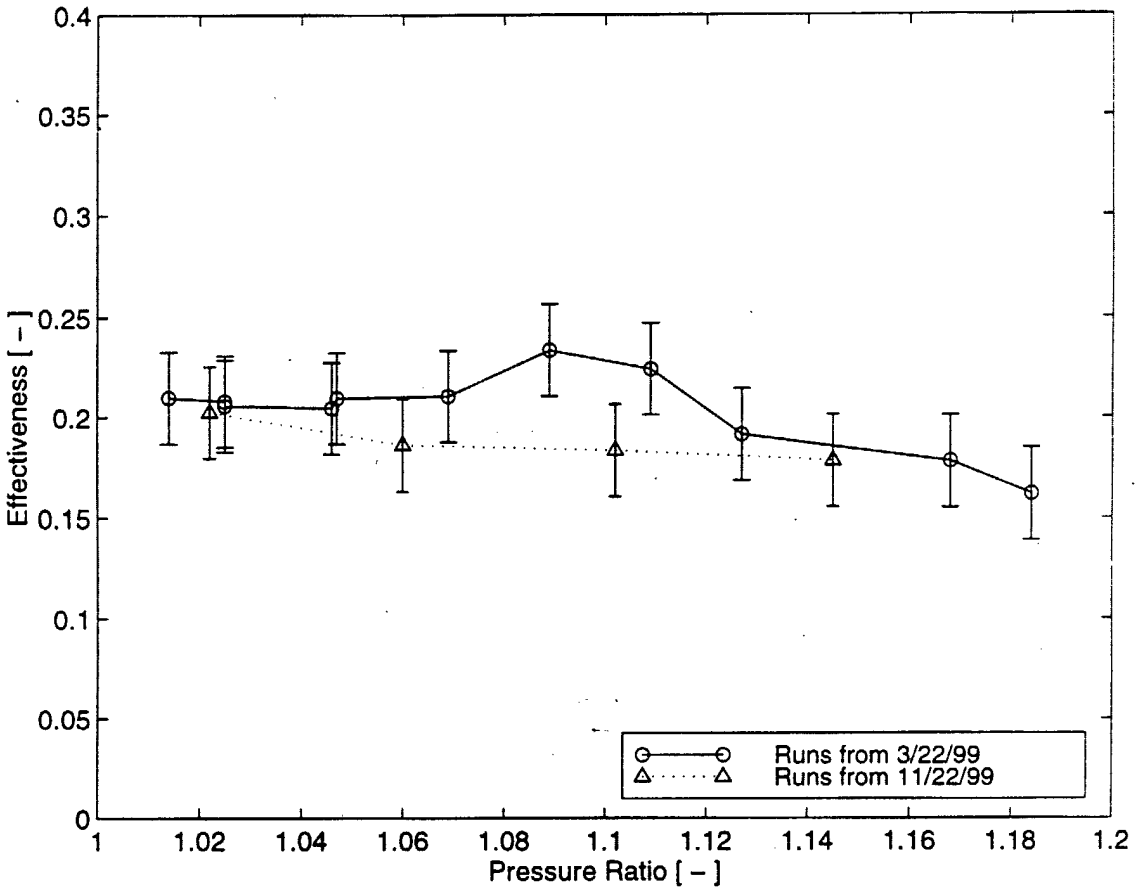

Figure 4.18: Variation of Film Cooling Effectiveness with Pressure Ratio for Gauge 5

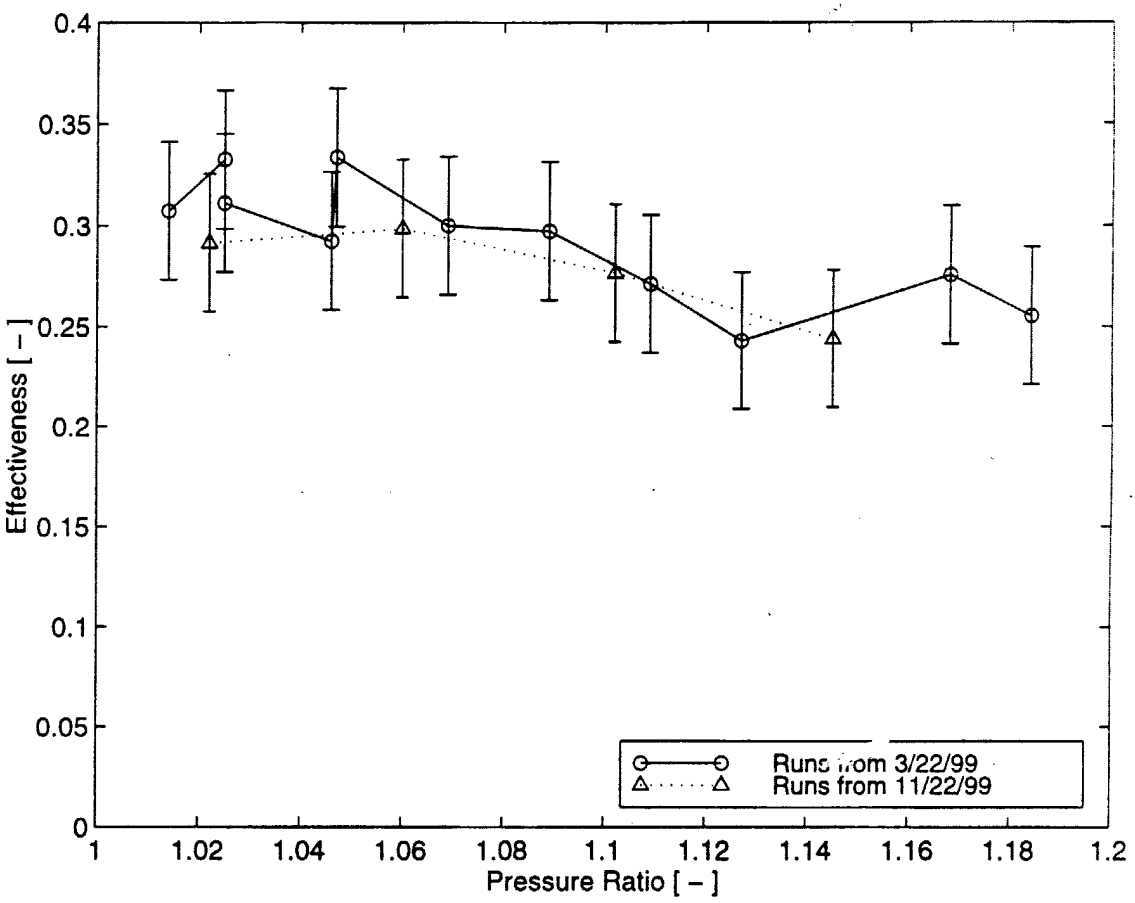

Figure 4.19: Variation of Film Cooling Effectiveness with Pressure Ratio for Gauge 6

4.4 Streamwise Variation of Heat Transfer Coefficient and Effectiveness

4.4.1 Experimental results

One of the objectives at the outset of this research was to measure and to explain the variation of heat transfer coefficient and film cooling effectiveness as a function of the streamwise distance from the coolant holes. These h and η profiles are shown in Fig. 4.20 and Fig. 4.21, respectively. These figures are taken from one representative run, and other runs show a similarly shaped profile.

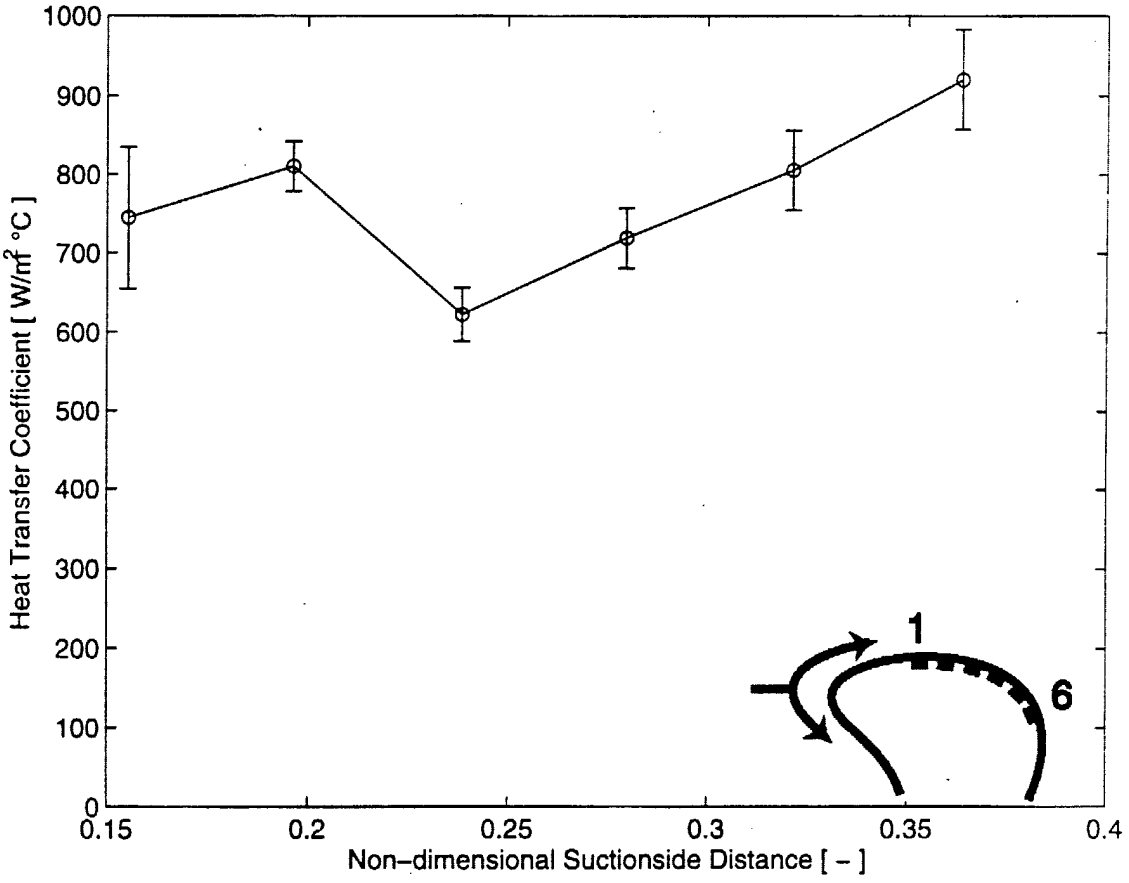

Figure 4.20: Heat Transfer Coefficient Profile at Pressure Ratio of 1.04

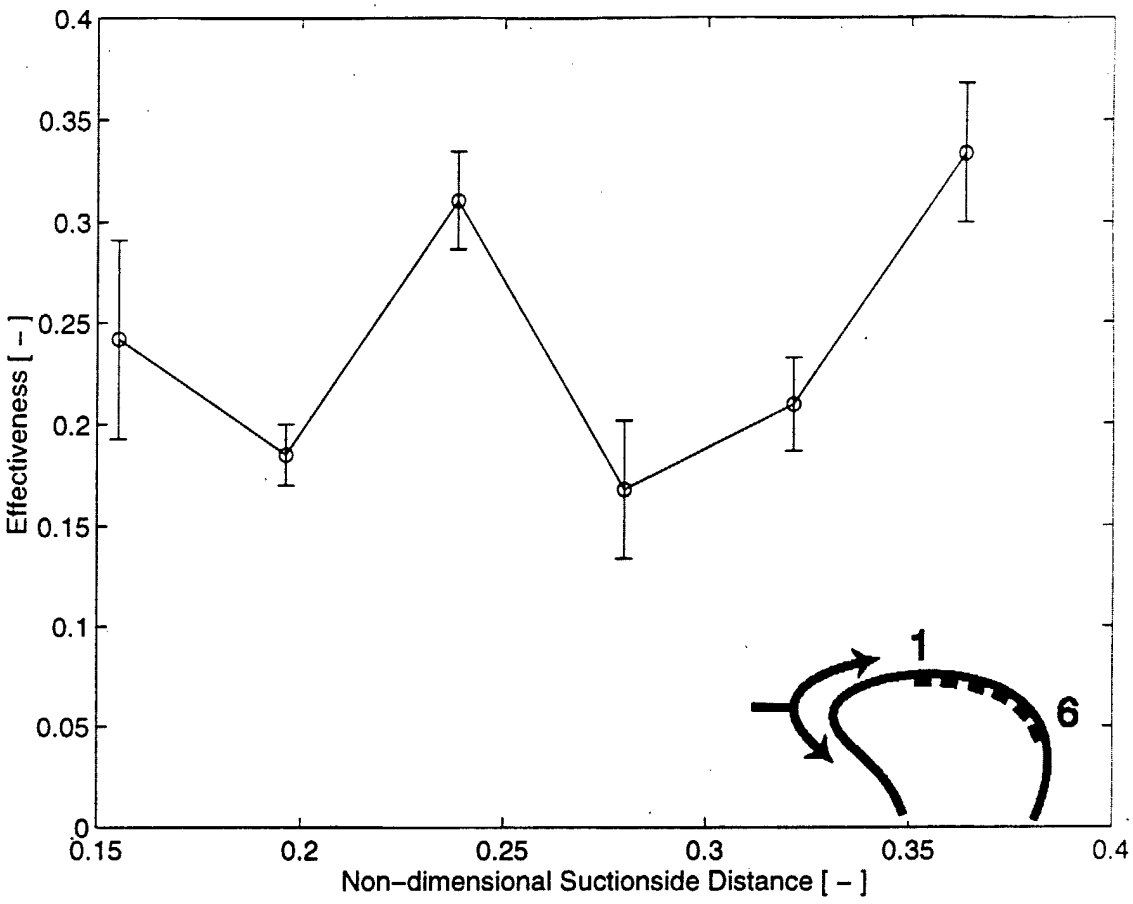

Figure 4.21: Film Cooling Effectiveness Profile at Pressure Ratio of 1.04

As can be seen, both the heat transfer coefficient and film cooling effectiveness vary significantly from location to location. The heat transfer coefficient starts high. decreases until Gauge 3, and then increases until Gauge 6. It is difficult to find a plausible explanation for this streamwise profile. There were several possible explanations proposed for the shape of these profiles, and a number of experiments were performed to investigate each of the possibilities. The next section describes and discusses different ideas that were proposed, the experiments performed to investigate the hypotheses, and the results of these experiments.

1. Transition

One thought was that the increase in heat transfer could be caused by transition of the boundary layer from a laminar to turbulent regime. It was somewhat doubtful that this would be the cause, however, since the same trend can be seen on both the non-film-cooled heat transfer data and film-cooled data. Shadowgraph pictures of a film-cooled blade also seemed to show a film layer that was turbulent from the very start. These pictures, however, provide only a spanwise averaged picture, and perhaps the boundary layer outside of the jet plumes (but along the surface of the blade) started laminar and transitioned to turbulent, giving the rise in heat transfer coefficient.

To investigate this possibility, a strip of sand was glued to the front of the blade to trip the boundary layer to turbulent. The sand strip was manufactured with 80 grit sand sealed with Polaroid sealant and the dimensions were in general as suggested by Chandraeskhara [3]. This setup should have insured that the boundary layer was turbulent for the entire length of the blade. A Schlieren picture of the tripped boundary layer without film-cooling is shown in Fig. 4.22. From Fig. 4.22 one can see that the boundary layer is turbulent when compared to that of the laminar un-tripped blade shown in Fig. 4.23. Also, from looking at the tripped picture it does appear that the boundary re-laminarizes far down the length of the blade. This occurs much farther down the blade surface then where the gauges are located. This boundary layer tripping strip did successfully provide a fully turbulent boundary over the region of scrutiny.

The experiment was run without film cooling to see if the heat transfer coefficient trends would become monotonic with surface distance as one might expect in a fully turbulent boundary. The results of this experiment, however, yielded heat transfer curves with the same shape but the heat transfer coefficient rose slightly (approximately 50 W/cm^2 °C) over the laminar case as one would expect.

At the end of this experiment, we felt fairly sure that the cause of the heat

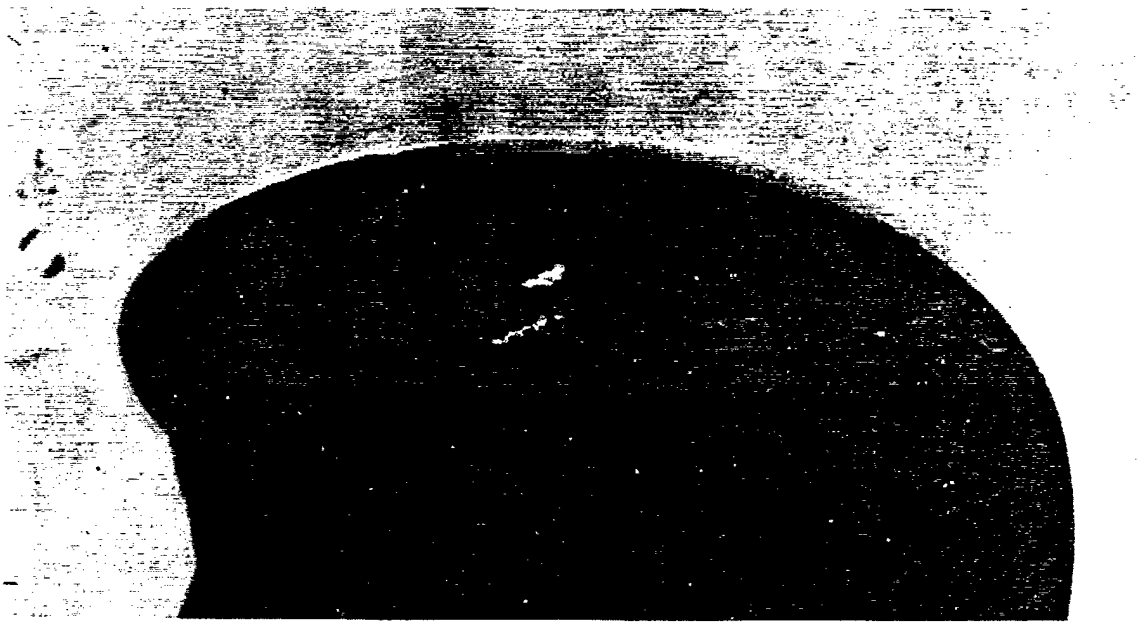

Figure 4.22: Schlieren of Blade with Tripped Boundary Layer (No Film Cooling)

transfer coefficient shape is not transition from laminar to turbulent.

2. **Calibration**

   Another possible cause for the both the peculiar heat transfer coefficient and film effectiveness profiles might be errors in the sensitivities of each HFM gauge. The sensitivities of the gauges have been investigated thoroughly in an attempt to eliminate this as a possible source of error. An in-situ calibration method for the HFM was developed and used as detailed by Smith et al. [23]. This in-situ calibration method provides a way for the gauges to be self calibrated every time the tunnel is run. The data was used from many of the runs and the gauges all have reasonable and repeatable sensitivities for each location. HFM calibration does not seem to be a likely explanation for the strange trends.

3. **Location of the Gauges with Respect to the Coolant Exits**

   As can be seen in Fig. 2.18 the gauges are not located consistently with respect to the coolant holes. Some gauges are located directly behind one

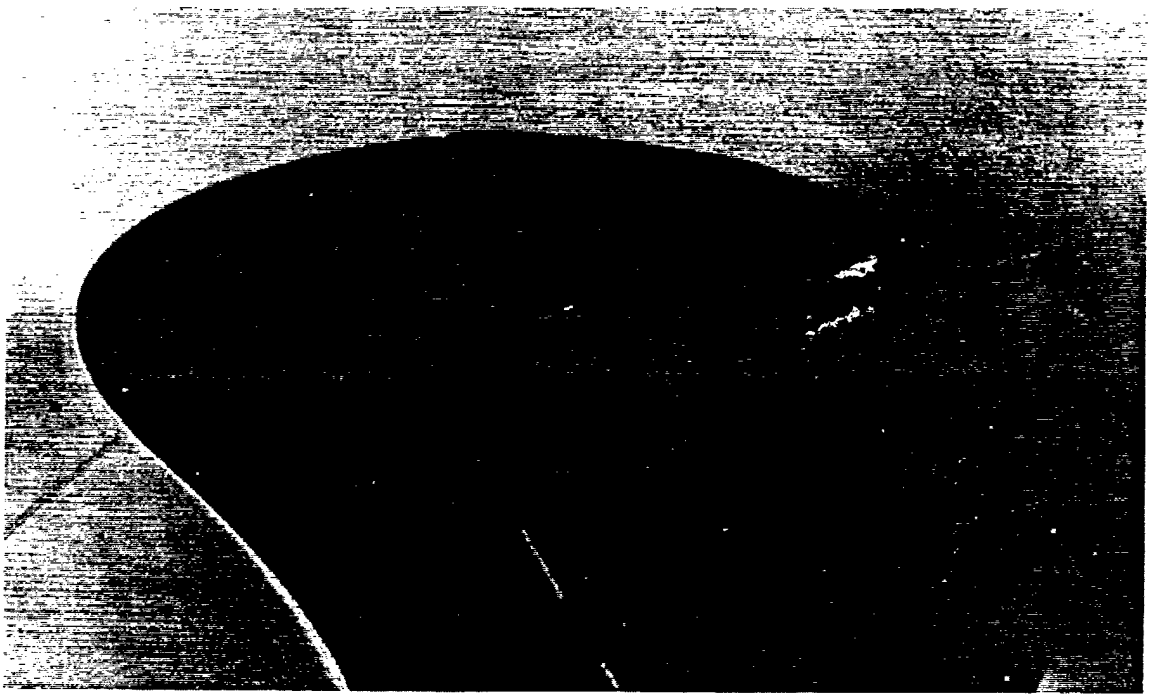

Figure 4.23: Schlieren of Blade with Un-Tripped Boundary Layer (No Film Cooling)

coolant exit, and some gauges have two coolant exits in front of them. The assumption in the experimental design was that the coolant would be sufficiently mixed spanwise by the time it reached the gauges. This might have been a bad assumption especially at Gauge 1 as it is so close to the last coolant exit.

If such were the case, it would explain the strange trends in cooling effectiveness. This hypothesis seems like the most plausible. Film cooling effectiveness can vary considerably if the film layer is not thoroughly mixed.

This hypothesis is a little more troubling to apply to the variations in heat transfer coefficient, however, since similar profiles persists in both the cooled and uncooled data. The only way this hypothesis might apply would be if the very presence of the film cooling holes even without the film coolant air running, was changing the flow field, therefore providing different heat transfer coefficients for different gauges. This is one scenario that may be occurring but it is suspected rather unlikely. The explanation for the h profiles is probably

somewhere else.

4. **Spanwise Variations of Heat Transfer Coefficient and Effectivness**

It is assumed in these experiments that the spanwise variations are secondary to the streamwise variations. Steps were taken to insure that the blade had as close to two dimensional flow as was possible and that the area of the measurements was sufficiently outside any secondary flow regimes. Because such steps had been taken, it was decided to stagger the gauges in the streamwise direction (as shown in Fig. 2.18) so that any effects from a gauge possibly not being flush to the surface (see item 5) would not effect the downstream gauges. Perhaps this assumption that the measurements are being made in a two dimensional portion of the blade is wrong. There might have been some significant spanwise variation that was measured.

In order to investigate this possibility, a simple oil dot surface flow visualization test was performed. This sort of test was inspired by a technical note written by Meyer [17] about oil dot visualization. Essentially, it was shown by Meyer that small oil drops placed on a surface would streak when placed in a wind tunnel. The length of the oil streak is proportional to skin friction, which is proportional to heat transfer. Therefore, the streak length is, at least qualitatively, proportional to the heat transfer on the blade at that location. Realizing this, a matrix of oil dots was placed on the blade before the tunnel was run. After the uncooled tunnel run, the lengths of these oil streaks were measured. Fig. 4.24 is a picture of the oil dots on the blade before the tunnel run, and Fig. 4.25 is a picture of the blade and oil streaks after the tunnel was run.

The results of these few experiments showed a repeatable variation of streak length in the streamwise direction and a rather uniform streak length in the spanwise direction. These results tend to confirm that there is uniform spanwise heat transfer. An attempt was made to correlate the streak length with the heat transfer coefficient in the streamwise direction. Unfortunately however, no

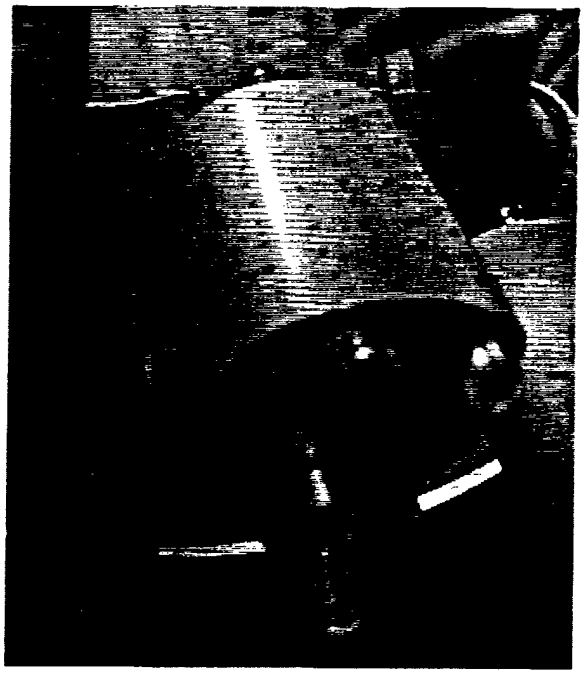

Figure 4.24: Setup of the Oil Streak Experiment

matching trends could be found from these tests.

These experiments added more confidence to ruling out spanwise variations as the cause of the peculiar heat transfer coefficient profiles.

5. **Gauge Offset**

One concern at the outset of this research program was that the flat surface heat flux gauges might not sit perfectly flush with the surface of the blade. Consequently, the lip where the gauge surface meets the blade surface would cause a disturbance in the boundary layer and effect the local heat transfer coefficient. This concern had been addressed earlier by Peabody [19]. He performed a number of tests to quantify the amount of error that both positive and negative gauge offsets introduce into the heat transfer measurements. His results showed that at a gauge offset of 0.010 inches there was a 40% difference in the heat transfer coefficient. Peabody's blades were one third the size of the blades used in this thesis and of the same profile. Since the blades used in this thesis

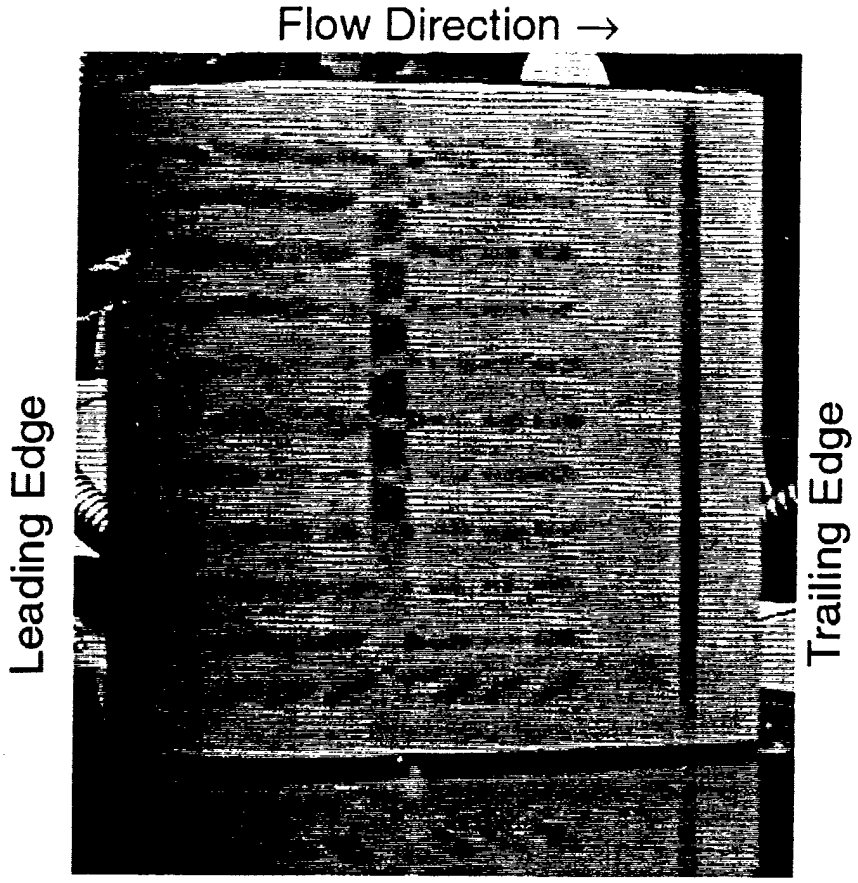

Figure 4.25: Oil Dot Streaks After Tunnel Run

are much larger, the local curvature and thus the offset is much smaller. An estimate of the worst offset of the gauges is about 0.001 inches. This offset may still be a source of error in the heat transfer coefficient measurements, but it is hard to believe it can account for the large changes in heat transfer coefficient.

4.4.2 Comparison to Published Results

An comparison of the Virginia Tech data to other published results is made in the following section . This comparison was made from General Electric data

from a similar conditions and is shown in Fig. 4.26 and Fig. 4.27. As shown,

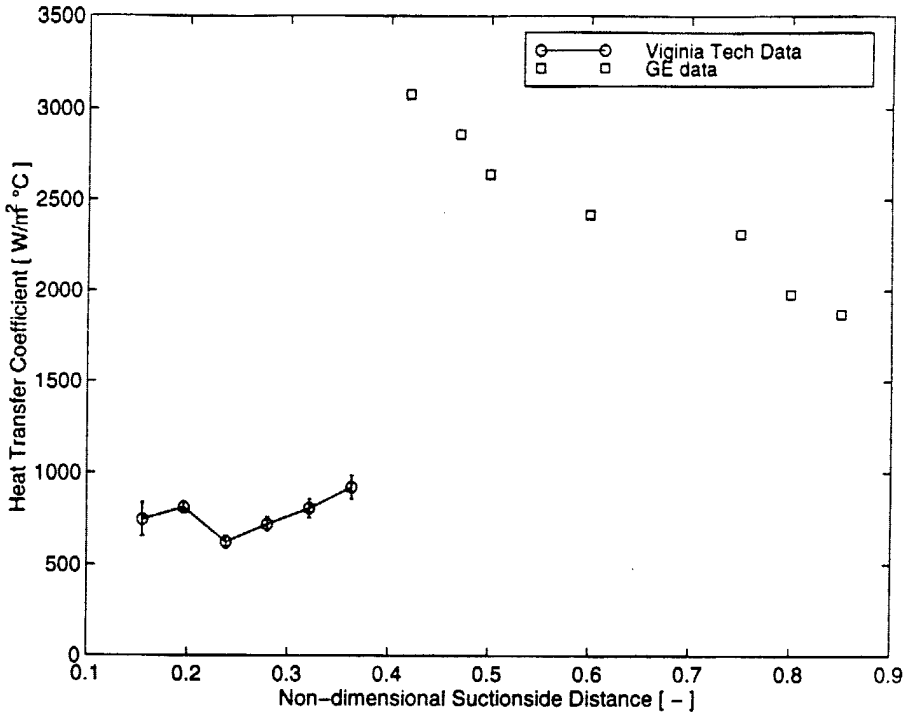

Figure 4.26: Comparison of Heat Transfer Coefficient

both the values of the heat transfer coefficient and the effectiveness are higher. This difference can be partially attributed to the fact the the General Electric blades had a film-cooling showerhead scheme with much more coolant exits. One can see the the General Electric film-cooling effectiveness drops off rapidly as downstream distance increases.

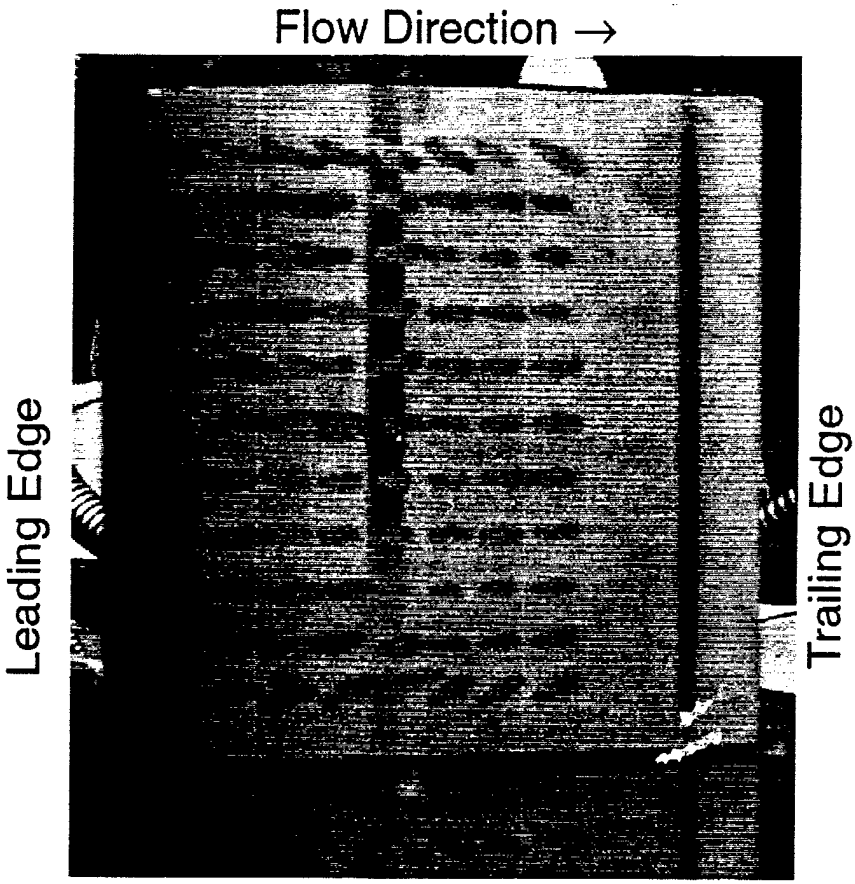

Figure 4.27: Comparison of Film-Cooling Effectiveness

Chapter 5

Conclusions

The primary goal at the outset of this research was to investigate the influence of pressure ratio on the heat transfer coefficient and film cooling effectiveness. The experimental results show that the heat transfer coefficient is nearly independent of the pressure ratio. Previous research at the same facility indicated that the presence of a coolant film increases the heat transfer coefficient when compared to an uncooled blade [22]. This research has extended that observation to state that the value of the increased heat transfer coefficient is independent of pressure ratio and coolant mass flow.

In addition, the film cooling effectiveness has been shown to be relatively independent of the pressure ratio. Film detachment is not seen over the tested range of pressure ratios. This conclusion is supported both by the film cooling effectiveness data and the shadowgraph pictures. Furthermore, this conclusion has been seen in research under similar conditions conducted by Epstein et al. [1].

It was also seen that the film cooling effectiveness has some slight trends at certain gauge locations. Gauges 1, 2, and 4 suggest an independence of pressure ratio

and effectiveness, and Gauge 3, 5, and 6 show a slight decrease in effectiveness with increasing pressure ratio.

In order to have a reasonable explanation for why the effectiveness has a decreasing trend, one must suppose a possible behavior of the three-dimensional flow field. Fig. 5.1 provide a few illustrations of what the flow field might possibly look like. In this figure, parts A and B show how an increase in momentum ratio might

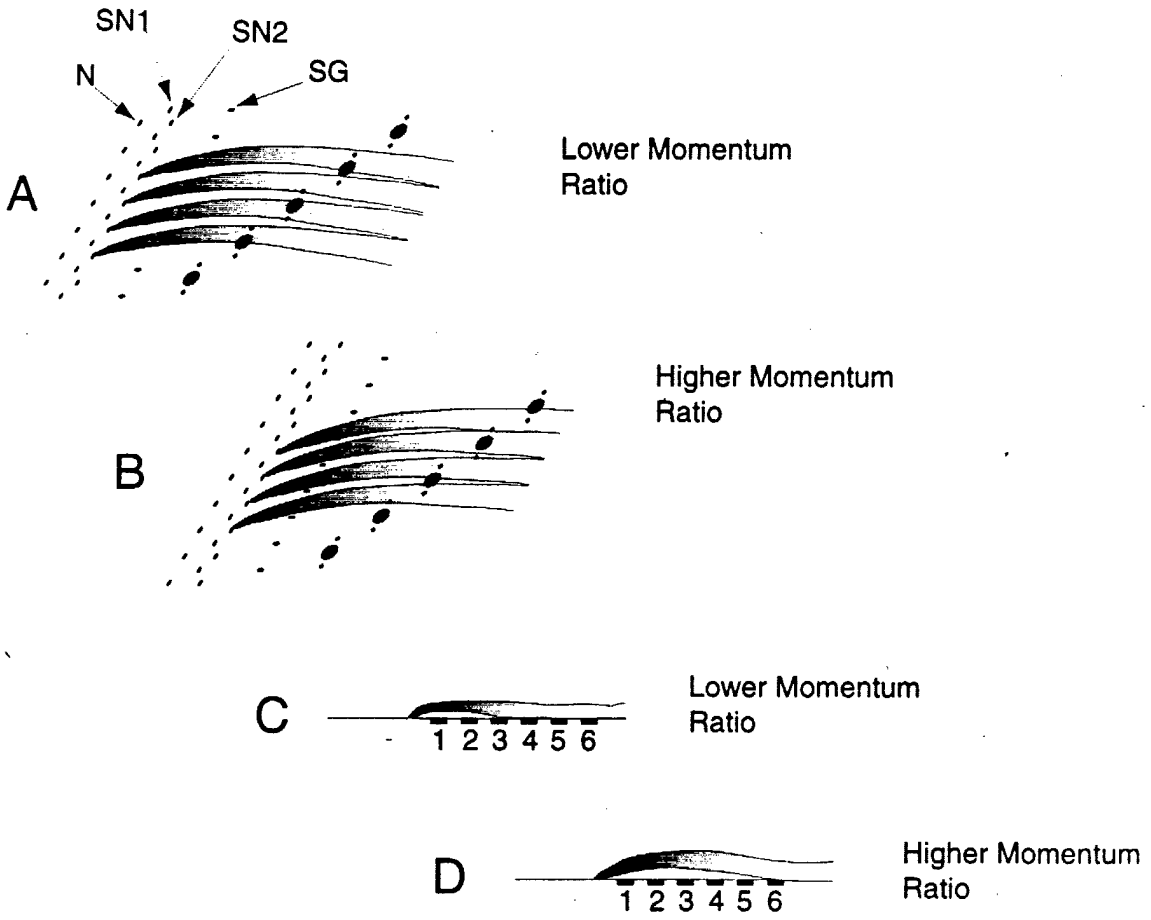

Figure 5.1: Possible Three-Dimensional Coolant Flow Fields

affect the angle SN2 or SN1 holes. In effect, the coolant film might move spanwise on the blade surface resulting in more or less film coverage depending on gauge location. Pictures C and D show a cross-section view of how the SG coolant might behave with

changes in momentum ratio. The increase in momentum ratio might lift the coolant film off the first gauge locations allowing the hot freestream gases to be exposed to the blade surface. The shadowgraph visualizations discussed in Sec. 4.1 tend to indicate that the dynamics in pictures C and D are not present. These Schlieren photographs, however, give only a streamwise averaged picture of the flow.

Perhaps more important than the supposition of reasonable flow dynamics, is the realization that the coolant flow is not one-dimensional or even two-dimensional. The flow in this area is very three-dimensional and very complicated. In order to really understand how it behaves, additional measurement techniques need to be used (liquid crystals, LDV's, a tighter spacing of gauges, etc.).

The sort of scenarios described above are possible if the coolant film is not well mixed over the gauge area. In continuing research it would be advisable to increase the number of coolant holes either by increasing the number of holes or decreasing the s/D spacing. This might provide a more evenly mixed film layer that would be better for study.

Another area of future study is an investigation of freestream turbulence. As suggested in Sec. 1.2.3, freestream turbulence has an effect of film cooling effectiveness and heat transfer coefficient. The turbulence levels for these tests are also much lower than is seen in a real engine environment. An expansion of this research to higher turbulence levels would certainly be an interesting endeavor.

A last area of recommended research would to be to investigate similar effects on the pressure side of the blade. Past research (Ito [13] for example) has shown the pressure side of turbine blades to be much more sensitive to film lift-off.

Bibliography

[1] R. S. Abhari and A. H. Epstein. An experimental study of film cooling in a rotating transonic turbine. *ASME Journal of Turbomachinery*, 116, 1994.

[2] N. Abuaf and R. Bunker. Heat tansfer and film cooling effectiveness in a linear airfoil cascade. *ASME Journal of Turbomachinery*, 119, 1997.

[3] M.S. Chandraeskhara, M.C. Wilder, and L.W. Carr. Boundary layer tripping studies of compressible dynamic stall flow. In *AIAA 25th Fluid Dynamics Conference*, number 94-2340, 1994.

[4] T. E. Diller. *Advances in Heat Flux Measurements*, volume 23. Academic Press, Inc, 1993.

[5] V. Ekkac, Srinath, Hui Du, and Je-Chin Han. Local heat transfer coefficent and film effecitveness distributions on a cylindrical leading edge model using a transient liquid crystal image method. Presented at the ASME International Mechanical Engineering Congress and Exposition, 1995.

[6] N. W. Foster and D. Lampard. Effects of density and velocity ratio on descrete hole film cooling. *AIAA Journal*, 13, 1975.

[7] R. J. Goldstein. Film cooling. In *Advances in Heat Transfer*. Academic Press, Inc, 1971.

[8] R. J. Goldstein, E. R. G. Eckert, V. L. Ericksen, and J. W. Ramsey. Film cooling following injection through inclined circular tubes. *Israel Journal of Technology*. 8, 1970.

[9] Hank Grabowski. An optical study of a film cooled turbine blade. Master's thesis, Virginia Polytechnic Institute and State University, 1999.

[10] S. M. Guo, T. V. Jones, and G. D. Lock. Gas turbine heat transfer measurements with engine simulated film cooling. In *2nd Annual European Conference on Turbomachinery Fluid Dynamics and ThermoDynamics*, 1996.

[11] David Holmberg. *Frequency Domain Analysis of Surface Heat Transfer/Free-Stream Turbulence Interations in a Transonic Turbine Cascade.* PhD thesis, Virginia Polytechnic Institute and State University, 1996.

[12] Forrest M. Mimms III. *Engineer's Mini-Notebook.* Siliconepts, second edition, 1994.

[13] S. Ito, R. J. Goldstein, and E. R. G. Eckert. Film cooling of a gas turbine blade. *The ASME Journal for Engineering Power*, 100, 1978.

[14] Venkit Iyer. Computer program bl2d for solving two-dimensional and axisymmetric boundary layers. Contractor Report CR-4668, National Aeronautics and Space Administration, 1995.

[15] Walter G. Jung. *IC Op-Amp Cookbook.* SAMS, third edition, 1986.

[16] P. M. Ligrani, S. Ciriello, and D. T. Bishop. Heat transfer, adiabatic effectiveness, and injectant ditributions downstream of a single row and two staggered rows of compound angle film-cooling holes. *ASME Journal of Turbomachinery*, 114, 1992.

[17] R. F. Meyer. A note on a technique of surface flow visualisation. Aeronautical Report LR-457, Canada National Research Council, 1966.

[18] R. J. Moffat. Describing uncertainties in experimental results. In *Experimental Thermal and Fluid Science.* Elsevier Science Publishing Co., Inc., 1988.

[19] Hume Peabody. Evaluation of a heat flux microsensor in a transonic turbine cascade. Master's thesis, Virginia Polytechnic Institute and State University, 1997.

[20] Oliver Popp. *Steady and Unsteady Heat Transfer in a Film Cooled Transonic Turbine Cascade.* PhD thesis, Virginia Polytechnic Institute and State University, 1999.

[21] S. G. Schwarz, R. J. Goldstein, and E. R. G. Eckert. The influence of curvature on film cooled performance. *The ASME Journal of Turbomachinery*, 113, 1990.

[22] Dwight Smith. Evaluation of heat transfer coefficient and film cooling effectiveness in a transonic turbine cascade. Master's thesis, Virginia Polytechnic Institute and State University, 1999.

[23] Dwight Smith et al. A comparison of radiation versus convection calibration of thin-film heat flux gauges. In *The ASME Ad-Hoc Committee on Heat Flux Measurement*, 1999.

[24] Angela Wesner. *An Interferometric Study of Unsteady Passing Shock Flow in a Turbine Cascade.* PhD thesis, Virginia Polytechnic Institute and State University, 1996.